Acoustic Softening and Acoustic Stiffening

Modifications of Thermal Conductivity from Altered Dispersion Relations in Si and ZnO Nanostructures

By

Matthew Dale Gerboth

Dissertation
Submitted to the Faculty of the
Graduate School of Vanderbilt University
in partial fulfillment of the requirements
for the degree of

DOCTOR OF PHILOSOPHY

in
Interdisciplinary Materials Science

October 31st, 2020

Nashville, Tennessee

Approved by:

Greg Walker

Deyu Li

Shihong Lin

Clare McCabe

Richard Mu

Dedication

To my wife, Lisa, for your patience, love, and support.

Acknowledgements

This work would not have been possible without the support of many people. I would like to thank my advisor Dr. D. Greg Walker for his support over these many years, my collaborator and committee member Dr. Deyu Li, and the rest of my committee, Drs. Clare McCabe, Shihong Lin, and Richard Mu.

I would further like to thank Dr. Lin Yang and Dr. Qian Zhang, former members of Deyu Li's group, whose experimental work inspired and motivated much of the exploration of softening effects in silicon here.

I would also like to thank my family and friends for their unceasing support across these many years.

Support for this work was provided by the National Science Foundation (CBET-1403456). This work was conducting in part using the resources of the Advanced Computing Center for Research and Education (ACCRE) at Vanderbilt University.

Portions of this work have been published as "Effects of acoustic softening on thermal conductivity beyond group velocity" in the Journal of Applied Physics[1]. All portions used are my work.

Table of Contents

List of Figures

List of Tables

Chapter 1

Introduction

For many engineering applications, controlling heat transfer is critical to ensuring high performance. This remains true both at the macroscale and the nanoscale. Key to understanding heat transfer at any scale is the thermal conductivity, or ease with which heat can flow through a material. At the macroscale high thermal conductivity allows for the rapid dispersal of heat, while low thermal conductivity materials can be used for thermal insulation. At the nanoscale, maintaining high electrical conductivity while reducing the thermal conductivity is critical to creating efficient thermometric materials. For microelectronics, as the size is reduced, cooling becomes an important limiting factor on performance.

Understanding thermal conductivity is critical for designing materials and devices that control or manipulate heat transfer. At the nanoscale, the influence of surfaces introduces several effects that can alter the thermal conductivity. The main influence of surfaces is seen through phonon scattering, however other effects have been reported. In particular, surface effects in many materials cause the elastic modulus to change locally. At the nanoscale where surfaces can dominate the physics, the effective properties of the system can assume values more like the surface than the bulk.

From a continuum understanding of waves in solids, the speed of phonons, the major carriers of thermal energy in non-metallic solids, can be expressed as $v_g = \sqrt{E/\rho}$ where E is the elastic modulus and ρ is the density. In silicon (Si), reductions in the elastic modulus have been implicated in measurements of very low thermal conductivity for nanostructures with dimensions of about 20 nm or smaller [2–4], where the effect has been termed acoustic softening.

In addition to Si, a number of other materials have effective elastic moduli that are size dependent—some are even known to stiffen with reduction in size. However, there is far less experimental evidence for either acoustic softening or acoustic stiffening in other nanomaterials [4]. This leads one to ask when do effects from changes in the elastic modulus become apparent at the nanoscale? And, more important to this research, how does the size dependence of the elastic modulus at the nanoscale manifest itself in thermal conductivity?

In this work I use both modeling and molecular dyanamics (MD) simulations to demonstrate that the size dependence of the elastic modulus at the nanoscale should impact not only the velocity of phonons, but also the phonon heat capacity and the phonon scattering rates—the three main factors that govern thermal conductivity. While a surface level consideration of acoustic softening or acoustic stiffening effects would indicate that the thermal conductivity decreased or increased proportional to the square root of the change in the elastic modulus, respectively, the consideration of effects beyond the group velocity, leads to competing impacts on thermal conductivity. It is the combination of these effects that is responsible for the total influence of acoustic softening or acoustic stiffening on thermal conductivity. Understanding how these effects combine offers opportunities to target materials with a high potential to display acoustic softening/acoustic stiffening effects for further study.

1.1 Nanoscale Elastic Modulus

Key to understanding acoustic softening and acoustic stiffening effects in nanostructures is the size dependence of the elastic modulus in nanowires. The elastic modulus, or Young's modulus, measures the resistance of a material to non-permanent deformation. In Si a number of experiments have investigated a decrease in the elastic modulus as a function of decreasing nanostructure size. When deformed elastically, structures store energy in both the bulk and the surface but at different rates. For structures with sufficiently large surface-area-to-volume ratios, surface elasticity contributes significantly to the effective elastic modulus. Early work by Miller and Shenoy [5] indicated that for Si, the increasing influence of the surface elasticity should cause a softening effect. In Si, studies of the elastic modulus of nanostructures employing molecular dynamics and ab initio methods have found size-dependent softening of this type [6–12], but numerical analyses tend to predict the onset of softening occurring at much smaller sizes, and to a lesser degree, than observed in experiments [7, 13–15]. To reconcile the discrepancies between theoretical calculations and experimental work, several explanations have been proposed, including native oxide layers [14, 16, 17] and manufacturing defects [13, 14].

Experimentally, size-dependent reductions in the effective elastic modulus have been reported for a number of Si nanostructures, including wires [15, 16, 18, 19], nanotubes [2], and cantilevers [13, 20]. In work by Yang et al. [3] both the effective elastic modulus and thermal conductivity were measured for FIB manufactured nanoribbons. In both the work on nanotubes from Wingert et al. and the work on nanoribbons by Yang et al. thermal conductivity and the elastic modulus decrease with decreasing nanostructure size, and the thermal conductivity decreases below what would be expected from boundary scattering alone implicating softening in the decreased thermal conductivity value.

Silicon is far from the only material that exhibits a size-dependent elastic modulus at the nanoscale. Recent reviews have identified significant experimental evidence for size-dependent elastic moduli at the nanoscale materials including Ag, Au, Cu, GaN, GaAs, and ZnO [21]. Nanoscaled ZnO has been explored for use in various applications, including sensing applications [22], solar cells [22, 23], and thermoelectric applications [24]. In contrast to Si, stiffening in ZnO nanowires has been reported with much more consistency [21]. Using a resonance method Chen et al. measured the elastic modulus of nanowires down to 50 nm in diameter and found an increase in the Young's modulus, especially for wires below 120 nm [25]. Further experimental investigations using resonance, nanoscale tensile, nanoindentation, and AFM manipulation methods have demonstrated the increase in the elastic modulus with reduced wire diameter [26–29]. Additionally, shear and buckling moduli have also been observed to increase with decreasing diameter [26, 28].

Results comparing the tensile and buckling modulus for nanowires have found a stronger diameter dependence for the buckling modulus than for the tensile modulus [28], indicating a surface driven effect. Treating the surface effects as a stiffened surface region, core-shell type models have proven capable of capturing a large portion of experimental results [25, 26, 29, 30]. For wires exposed to atmosphere, a 3-shell model provides an improved fit indicating that there is an oxygen-affected region at the surface that causes an increase in the stiffening effect [29].

To explain these effects, many researchers have turned to the change in coordination number at the surface of the ZnO nanowires [25–29, 31] which causes a relaxation of the surface. The change in the bond length at the surface due to the altered coordination number has been correlated with the increased surface elastic modulus [32]. Calculations of the change in the bond length at the surfaces from fitted elastic modulus data are in line with observations [25].

Molecular dynamics simulation of ZnO nanowires' elastic moduli have also shown that the elastic modulus is increased as the diameter is reduced [27, 33] in contrast to silicon nanowires. Combined experimental and computational investigation has shown good quantitative agreement between stiffening predicted by MD and that observed experimentally [27]. Analysis of the layer-by-layer elastic modulus confirms that the surface layers are strongly stiffened, while there is a small amount of softening in the center of the nanowire [27], indicating that the surface effects responsible for stiffening seen in experiment are captured by MD. The combination of strong experimental evidence for stiffening, and good agreement with computational methods makes ZnO nanowires a good system for exploring the effects of surface stiffening on thermal conductivity.

1.2 Nanoscale Thermal Conductivity

Thermal conductivity is one of the most important properties of underlying heat transfer. In the presence of a temperature gradient, heat flows from hot to cold, driven by the difference in temperature. This flow can be described by Fourier's law,

$$\boldsymbol{q} = -\kappa \nabla T, \tag{1.1}$$

where $\boldsymbol{q}$ is the heat flux density, in $\mathrm{W} \cdot \mathrm{m}^{-2}$, ∇T is the temperature gradient, and κ is the thermal conductivity, in $\mathrm{W} \cdot \mathrm{m}^{-1} \cdot \mathrm{K}^{-1}$. The thermal conductivity is a material property that represents the ease with which thermal energy can move through a material. For a given temperature gradient, the higher the thermal conductivity the more heat will flow across the gradient.

In materials without significant electrical conductivity heat is dominantly carried by vibrations of the crystal lattice, which when quantized are termed phonons[1]. From the point of view of phonons, thermal conductivity can be modeled as [34]

$$\kappa = \frac{1}{3} \sum_i \int C_v(\omega) v_g(\omega) l(\omega) d\omega, \tag{1.2}$$

where C_v is the phonon heat capacity, v_g is the group velocity, ω is the phonon frequency, and l is the phonon mean free path. The sum is taken over the branches of the phonon dispersion. This model, sometimes termed the kinetic model, demonstrates the main factors that influence the lattice thermal conductivity. The phonon heat capacity C_v indicates how much energy each phonon mode can carry; the group velocity, the speed at which the phonon can move; and the mean free path the distance the phonon can travel before a scattering event. The integral is taken over the phonon frequencies ω as the specific heat, group velocity

---

[1] In materials with significant electrical conductivity, electrons can carry significant thermal energy. In this work we focus on semiconductors and lattice (phonon) thermal conductivity and so ignore any electrical contribution to thermal conductivity.

and mean-free path are spectral quantities.

The phonon frequency is calculated using the dispersion relation. The dispersion relation relates the phonon wave vector q to the phonon frequency and describes the allowable phonon frequencies[2]. In general the dispersion relation is examined over the first Brillouin zone (FBZ), as wave vectors outside of the FBZ convey the same information as wave vectors inside it. From the dispersion relation many parameters may be deduced including the phonon group and phase velocities which are key to this work. The group velocity can be found as $v_g(\omega) = d\omega/dq$ and at the center of the FBZ is equivalent to the speed of sound in the material.

In nanostructures, the thermal conductivity is mainly limited by the mean free path of phonos that scatter off the surfaces. Scattering events restrict heat flow, reducing the thermal conductivity, and surfaces create site where scattering can occur. Scattering can also occur due to impurities (such as interstitial atoms, or isotropic differences), dislocations, and grain boundaries. Phonon-phonon scattering, or scattering processes that involve multiple phonons restrict thermal conductivity as well and are responsible for much of the high temperature behavior of thermal conductivity. In general, the scattering rates can be expressed as power functions of the phonon frequency.

Considering experimental investigations of nanoscale thermal conductivity in Si, initial measurements of single nanowires by Li et al. demonstrated that the thermal conductivity was significantly reduced from the bulk value [36]. For wires with diameters greater than 22 nm, the reduced thermal conductivity could be explained through classical surface scattering effects. However, for 22 nm wires, classical explanations did not suffice and deviations from a T^3 low temperature dependence were found. Further work by Chen et al. measured the thermal conductance of similarly thin chemical vapor deposition (CVD) grown silicon nanowires with diameters ranging from 15 nm to 50 nm [37]. The measurements confirmed the deviation from a T^3 low temperature dependence, which Chen et al. attributed

---

[2] For more information on calculating a dispersion relation and the FBZ see a condensed mater textbook such as Ashcroft & Mermin [34], or a work on lattice dynamics such as [35]

to frequency-dependent boundary scattering; however, their model consistently predicted higher thermal conductivity near room temperature than observed. Work by Wingert et al. using Ge and Ge-Si core-shell nanowires with diameters of 20 nm additionally observed highly reduced thermal conductivity and modifications to the temperature dependence of thermal conductivity [38]. They found an enhancement to thermal conductivity at low temperature, and a reduction at room temperatures for the Ge-Si core-shell nanowires.

Subsequent work by Wingert et al. examining crystalline Si nanotubes found thermal conductivities below the limit for boundary scattering and below measured values for amorphous silicon [2]. To explain these highly reduced thermal conductivities, Winger et al. proposed acoustic softening. Building on theoretical and experimental evidence of the size dependence of the elastic modulus in nanostructures, Wingert et al. hypothesized that the phonon group velocity, which is proportional to the elastic modulus, may be reduced for small wires, significantly contributing to reduced thermal conductivity. They also measured significantly reduced elastic moduli for their Si nanotubes using nanoscale tensile tests, lending credence to the acoustic softening hypothesis.

Thermal conductivity can be approximated as $\kappa = \frac{1}{3} C_v v l$, where v is the phonon group velocity and l is the MFP. This expression is similar to equation 1.2 but does not contain the spectral dependence. Although this equation is not used for calculations, it is nevertheless a useful instructional tool. In nanostructures, reduced thermal conductivity is usually attributed to a reduced MFP arising from surface scattering; in contrast, acoustic softening causes additional reductions in the thermal conductivity of nanostructures that arise from a reduction in v. In the continuum limit, the speed of sound (and thus the long wavelength phonon group velocity) is proportional to $\sqrt{E}$ where E is the Young's modulus, implying that a softening of the material should induce a reduction in the phonon group velocity.

Much as for nanoscaled silicon, in nanoscaled ZnO measurements of thermal conductivity have shown the thermal conductivity of nanowires to be reduced by more than an order of magnitude from bulk [39, 40]. In ZnO nanowires, the peak thermal conductivity has been observed to be shifted to higher temperatures than in bulk[39]. Bui et al. found that the thermal conductivity of ZnO nanowires reduced faster with diameter than would be predicted by Casimir limit based scattering models, while the addition of amorphous-carbon shells to the nanowires was not seen to alter significantly the thermal conductivity [39]. Experiments have shown that thermal conductivity of ZnO nanowires can be significantly reduced by ion implantation [40].

Molecular Dynamics investigations of ZnO nanobelts have also indicated a significant reduction in the thermal conductivity with decreased diameter [41–45]. The simulations can be fit with the equation for phonon radiative transport using boundary, three-phonon, and four-phonon processes [42]. In these nanobelts, thermal conductivity and the phonon group velocity share similar trends with temperature. Jiang, Park and Rabczuk performed MD simulations of thermal conductivity for ZnO nanowires and nanobelts, with various reconstructions to the polar surfaces. They found that the thermal conductivity of [1 1 0 0] oriented nanowires with polar surfaces stabilized by charge reduction, and the conductivity of the hexagonal nanowires were both significantly less than for [1 1 0 0] oriented ZnO nanowires with polar surfaces that were allowed to under go surface reconstruction, as the surface reconstruction reduced scattering of the bending modes by limiting the twisting of the wires [41].

By studying the thermal conductivity effects of stiffening in ZnO nanowires, we are able to elucidate competing effects on thermal conductivity of various factors influenced by stiffening and to note under which circumstances and at which size scales thermal conductivity will be most strongly affected. This competition in part and the small size scale needed to produce large thermal conductivity effects may explain the noted [4] lack of experimental evidence for stiffening in thermal conductivity measurements of ZnO.

Using dispersion relations that incorporate acoustic softening or acoustic stiffening, I was able to explore the influence of the size dependence of the elastic modulus at the nanoscale on the factors of thermal conductivity. For the first time I considered the influence of factors other than group velocity, namely heat capacity and scattering and explored the relative magnitude of effects on these factors in multiple materials. My efforts will help to advance a better understanding of the full scope of softening and stiffening phenomenon affecting nanoscale thermal transport. More importantly, this understanding can help identify materials that should demonstrate acoustic softening/acoustic stiffening effects for further study.

Chapter 2

Modeling Softening

Key to this work is the ability to include the effects of acoustic softening and acoustic stiffening in models of thermal conductivity. We can start to model thermal conductivity in Si and ZnO nanostructures by considering the frequency-dependent Landauer-like equations proffered by Callaway and Holland [46, 47],

$$\kappa = \frac{1}{3} \int C_v(\omega) v_g(\omega) F_g(\omega) l(\omega) d\omega, \tag{2.1}$$

where $C_v(\omega)$ is the spectral phonon heat capacity, $v_g(\omega)$ the phonon group velocity, and $l(\omega)$ the mean free path, all functions of ω, the phonon frequency. $F_g(\omega)$ is the geometric reduction function used for nanoribbons and is added to the formulation to capture the influence of high aspect ratios on boundary scattering. As an implementation detail, the integral in equation 2.1 is taken with respect to the wave vector (q) over the FBZ. The phonon frequency and wave vector are related to each-other through the dispersion relation $\omega(q)$.

The effects of acoustic softening/acoustic stiffing act primarily through the dispersion relation. From continuum elastic theory, the speed of sound in a solid can be related to the elastic modulus E as $v_s = \sqrt{E/\rho}$, where ρ is the density of the material. From the perspective of the dispersion relation, v_s represents the slope of the dispersion relation close to the center of the FBZ, so changes to the elastic modulus should result in changes to the dispersion relation. Since all the terms in Eq. 2.1 are dependent on phonon frequency $\omega(q)$, the addition of softening to the dispersion relation, should result in effects arising in all of the frequency-dependent terms.

2.1 Born von Karmen Slack Model

To employ this model for thermal conductivity, we need a phonon dispersion for the material in question. For both softened and stiffened nanostructures we use a modified quarter-sine wave dispersion, which has been called the Born von Karman Slack (BvKS) model. This model has been found to accurately reproduce the thermal conductivity and accumulation functions in Si and Si/Ge nanowires [48, 49].

When stiffening or softening is added to the BvKS, the phonon dispersion function becomes

$$\omega = 2\pi F_s v_b q_0 \sin\left(\frac{\pi q}{2q_0}\right), \tag{2.2}$$

where the dispersion function is modeled as a quarter sine wave and fitted to the average bulk speed of sound [48]

$$\frac{1}{v_b^2} = \frac{1}{3}\left(\frac{1}{v_L^2} + \frac{2}{v_T^2}\right), \tag{2.3}$$

where v_L is the longitudinal speed of sound, and v_T the transverse speed of sound. q_0, the Debye cutoff wave vector, is determined from the atomic density. F_s is the stiffening/softening factor and is the ratio of the modified speed of sound to the bulk speed of sound v_b. Using a continuum analysis, this ratio can be expressed in terms of the elastic modulus as

$$F_s = \sqrt{\frac{E_{\text{nano}}}{E_{\text{bulk}}}}. \tag{2.4}$$

An example of the BvKS dispersion with and without acoustic softening is shown in Figure 2.1 for Si.

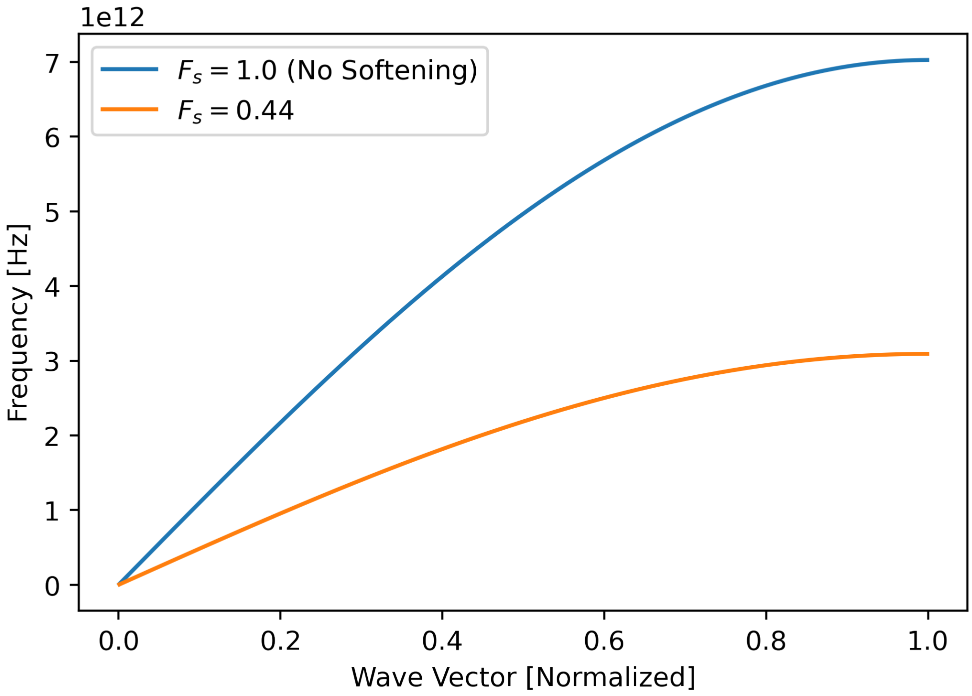

Figure 2.1: An example of the BvKS dispersion with and without acoustic softeningfor silicon.

2.2 Stiffening/Softening Model

In the case of the modified BvKS model, the effect of a size dependent elastic modulus is included through F_s. In the case of acoustic softening in Si, as the size of the wires decreases, F_s should decrease from approximately 1.0 at 50 nm to around 0.5 for 20 nm wires. For a stiffened wire, such as a ZnO nanowire, F_s will be greater than 1 and increase as the size of the wires decreases.

In ZnO, core-shell models for the nanoscale elastic modulus have found widespread adoption. For ZnO nanowires, the change in the elastic modulus with reduced size arises from the change in the coordination number of the surface atoms. This change reduces the bond order, reducing the bond length, and increasing the bond strength[32]. The end result is an increase in the overall elastic modulus. As the change in the elastic modulus is limited to the surface region, the effective elastic modulus of the nanowire as a whole can be treated using a composite model, consisting of a bulk-like core region and a stiffened shell region.

For nanowires in tension, this results in an effective elastic modulus of

$$E_{\text{nano}} = \frac{A_{\text{core}}E_{\text{core}} + A_{\text{shell}}E_{\text{shell}}}{A_{\text{core}} + A_{\text{shell}}}, \tag{2.5}$$

Where A_{core} and A_{shell} are the cross-sectional areas of the core and shell respectively, and E_{core} and E_{shell} are the core and shell elastic moduli. For a hexagonal nanowire, the cross sectional areas can be calculated as

$$A_{\text{core}} = 2\sqrt{3}\left(\frac{\sqrt{3}}{4}D - t\right)^2 \text{ and} \tag{2.6}$$

$$A_{\text{shell}} = \frac{3\sqrt{3}}{8}D^2 - A_{\text{core}}, \tag{2.7}$$

where D is the nanowire diameter, and t is the thickness of the shell. This results in 3 fitting parameters for the core-shell model, E_{core}, E_{shell} and t.

For the ZnO nanowires, we fit elastic modulus data from Agrawal et al. [27] to the model. This results in a shell thickness of 2.36 nm, a shell elastic modulus of 193.1 GPa, and a core modulus of 136.4 GPa. These parameters are within the ranges reported for other experimental studies of nanowires [25, 28, 29]. The core modulus is in line with the values of the elastic modulus for bulk ZnO. One issue arises for the MD wires that we must consider; at diameters around 5 nm the shell region fully overlaps the core region, and the model begins to underpredict thermal conductivity. To address this, we performed fits to the core-shell model including elastic moduli data from MD performed in this work (Chapter 3) and this fit is discussed further in Chapter 4. From these parameters, the stiffening factor F_s is then calculated from equation 2.4.

Unlike ZnO, core-shell models have difficult fitting the experimental observations of the elastic modulus for Si nanowires, particularly the data from Yang et al. [3]. Some fitting of experimental data using core-shell models are presented in Chapter 4. However, a recent review of size-dependent mechanical properties indicates that there is a high degree of scatter in the size-dependent Young's moduli reported from experiment [21] and that theoretical work predicted that softening should not be significant until smaller sizes than seen in experiment [13, 14].

Taking the above into account, for much of this work, we determine F_s for Si nanostructures by fitting the data from Yang et al.[3] for Young's modulus vs hydraulic diameter. Yang et al. have reported both Young's modulus and thermal conductivity for sets of Silicon nanoribbons. We fit the Young's modulus with the function

$$E = \frac{E_{\text{bulk}}}{1 + \exp\left[-k(d_h - d_0)\right]}, \tag{2.8}$$

where k and d_0 are fitting parameters related to the slope of Young's modulus and the diameter, respectively, where $E/E_{\text{bulk}} = 0.5$. E_{bulk} is the bulk Young's modulus. The fit (Figure 2.2) results in $k = 0.240\,\text{nm}^{-1}$ and $d_0 = 25.9\,\text{nm}$. E_{bulk} for the fit is 176.8 GPa, which is in line with experimental and theoretical values for silicon [17, 50, 51]. The sound speed reduction factor is then defined as

$$F_s = \sqrt{\frac{E_{\text{nano}}}{E_{\text{bulk}}}} = \sqrt{\frac{1}{1 + \exp\left[-k(d_h - d_0)\right]}}. \tag{2.9}$$

We note that in this definition the fitted bulk modulus cancels out. From this we find that $F_s = 0.55$ corresponds to a hydraulic diameter of approximately 22 nm.

2.3 Group Velocity

A change in group velocity is the most obvious factor that occurs with acoustic softening or acoustic stiffening. From a continuum point of view, the presence of a dominating surface alters the elastic modulus resulting in an effective modulus (E_{nano}) for the nanostructure. The speed of sound in the nanostructure is then related to the effective modulus as $v_s = \sqrt{\frac{E_{\text{nano}}}{\rho}}$. Therefore, if the effective modulus is reduced in a nanostructure because of the surface softening, so too should the group velocity. However, this reduction implies that there

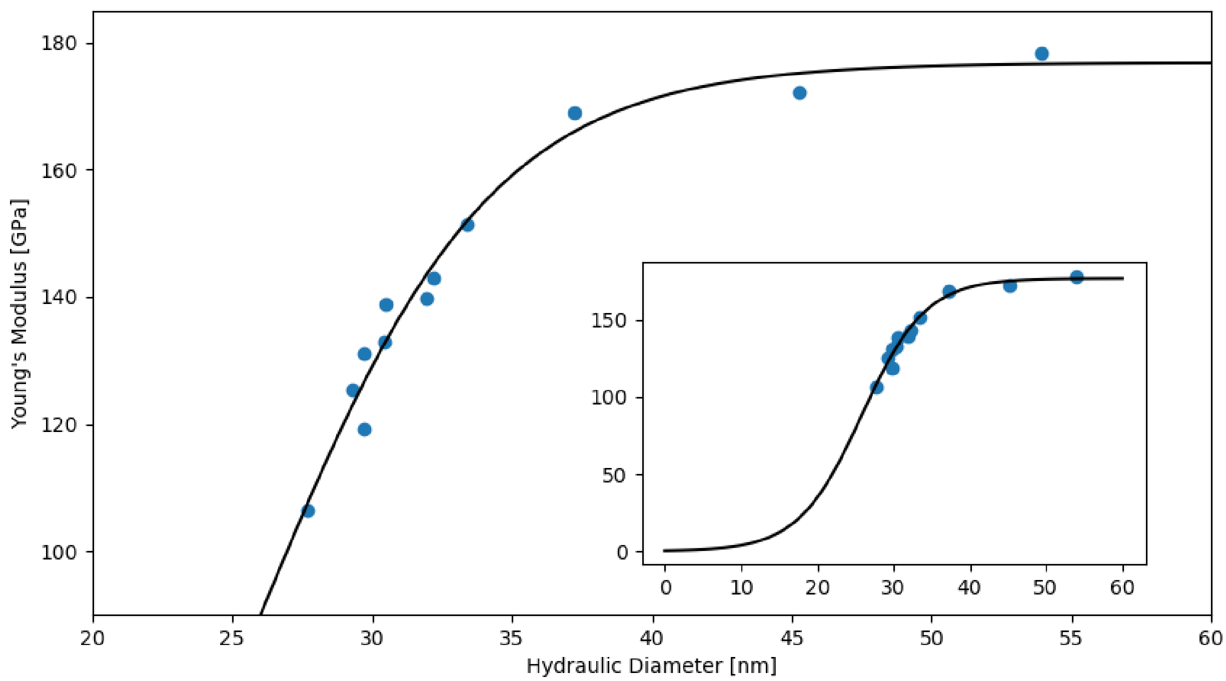

Figure 2.2: Fit of Young's modulus vs hydraulic diameter for nanoribbons from Yang et al. [3]. Inset: fit extended to 0 nm hydraulic diameter.

should be a reduction in the group velocity not only at the gamma point but also across the entire FBZ. More explicitly, a reduction in the elastic modulus reduces both the slope of the dispersion (group velocity) at the center of the FBZ, but also the phonon frequencies at the edge of the FBZ, which are also proportional to $\sqrt{E_{\text{nano}}}$.

Proceeding from the dispersion relation, the group velocity is given as $v_g = d\omega(q)/dq$. Considering the BvKS dispersion relation with a softening/stiffening factor F_s, the group velocity then becomes $v_{g,\text{nano}}(q,d) = F_s(d)v_{g,\text{bulk}}(q)$. This indicates that the effect on group velocity should be the same across the entire FBZ. That is, for a 15% softening factor, the group velocity is reduced by 15% for all wave vectors. This is demonstrated in Figure 2.3 where the group velocities for Si and ZnO with and without softening/stiffening are plotted.

2.4 Mean Free Path

Less obviously than group velocity, acoustic softening and acoustic stiffening can affect the mean free path (MFP). In nano-structured devices the MFP is controlled by multiple mecha-

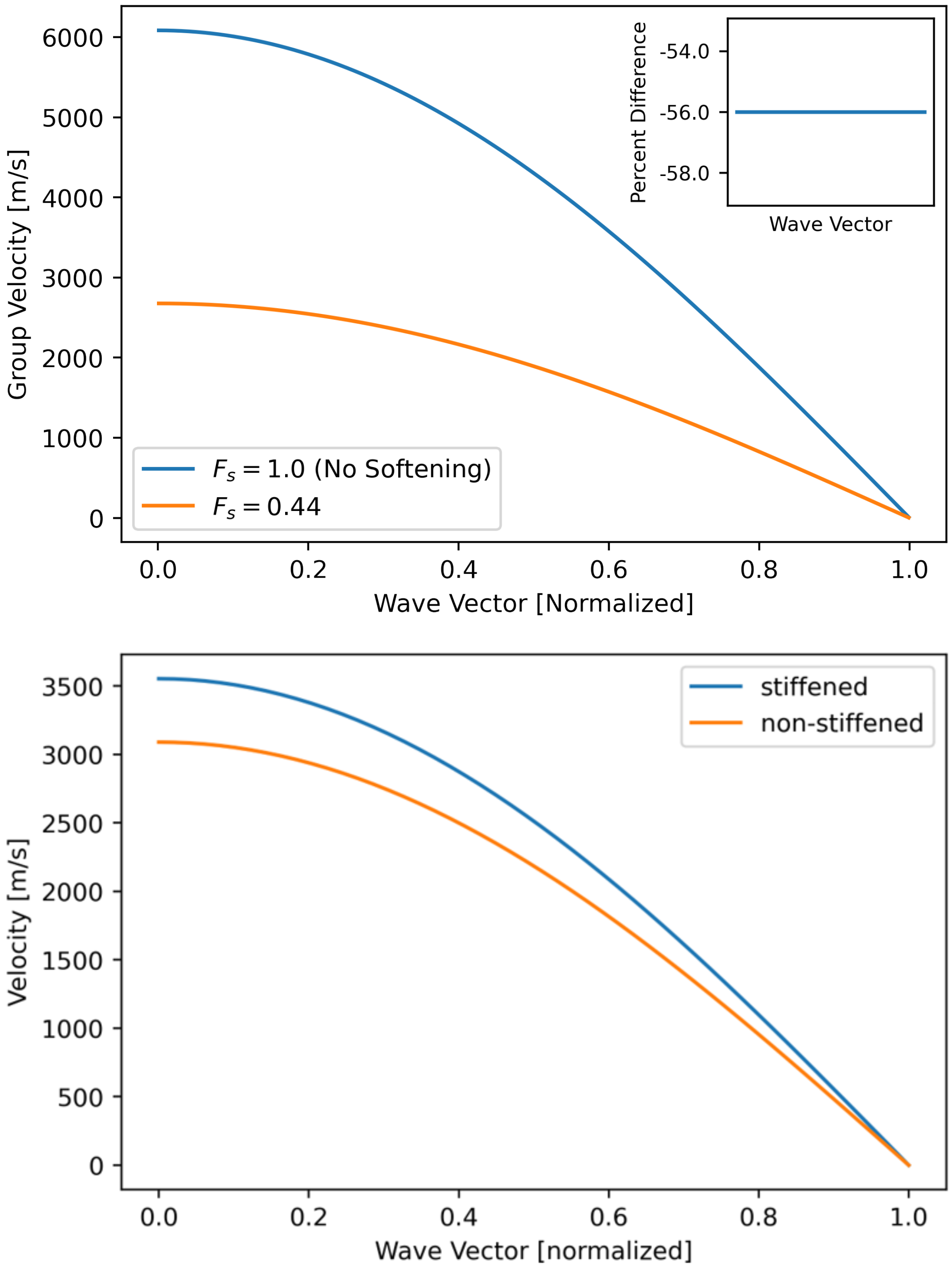

Figure 2.3: Group velocity for softened/stiffened nanowires calculated from the BvKS dispersion. Top: Silicon, inset: percent difference between softened and unsoftened group velocities demonstrating constant reduction. Bottom: ZnO with $F_s = 1.15$.

nisms: surface scattering, scattering at internal boundaries (e.g. grain boundaries), impurity scattering, phonon-phonon scattering, and dislocation scattering. The total MFP can then be calculated using Matthiessen's rule:

$$\lambda = v_g \left(\sum \tau_i^{-1} \right)^{-1} \tag{2.10}$$

where the τ_i^{-1} factors are the scattering rates from the various mechanisms.

While for bulk Si and ZnO scattering mechanisms such as grain boundary scattering and dislocation scattering are important for a good fit, they serve little purpose for our investigations. The Si nanoribbons that we are interested in are formed via epitaxy, so grain boundary scattering should result in a relatively small influence on the overall MFP. In our MD of ZnO, we do not model dislocations. Due to these factors we do not include either grain boundary or dislocation scattering in our nanoscale models.

Note that the MFP and the scattering rate are related through the group velocity $l = v_g \tau$. For boundary scattering in a nanowire, we can express the scattering rate as $\tau_{\text{boundary}} = D/v_g$. Thus, the mean free path resulting from the surface can be written as $l_{\text{boundary}} = D$ and is not affected by changes in the velocity from the stiffened dispersion relation.

2.4.1 Monte Carlo Ray Tracing

For structures with a single dominant dimension, e.g. films and wires, the characteristic length is used directly to estimate the boundary scattering; in structures that have more than one governing dimension, we have several options. Firstly, we can use an effective size, such as a Casimir length ($\sqrt{ab}$, where a and b are two different characteristic lengths of the system). Secondly, all device dimensions can be included through Matthiessen's rule ($1/l = 1/a + 1/b + \cdots$). And finally, we can use a more detailed model of the scattering, such as Monte Carlo ray tracing (MCRT), that rigorously accounts for several effects, such as corners and specularity. To compare results from our softened thermal conductivity model with nanoribbons, such as those produced by Yang et al., we use Monte Carlo ray tracing as the presence of two dominant dimensions (width and height) reduce the accuracy of the first two options. Parametric sweeps of thick ribbons with aspect ratios from 1 to 15 (similar to the aspect ratios seen in [3]) have been reported by Park et al. [52] and indicate that for structures between these ratios, the aspect ratio must be included in modeling the geometric reduction of thermal conductivity. In this regime, both cross sectional dimensions strongly influence the resulting MFP, and considerations such as corner effects become important, so the use of MCRT to model boundary scattering is warranted. While this method provides accurate boundary scattering, MCRT can be computationally intensive, so to isolate the effects of modifying the dispersion relation on thermal conductivity, we also present systems that include a single characteristic dimension.

In the MCRT approach, a calculated geometric factor $F_g(q, w, h) = \Lambda_n(q)/\Lambda_b(q)$ is the ratio of the actual nanostructure mean free path dictated by the boundaries scaled by the mean free path in a bulk material. The MCRT procedure takes its inspiration from the well-known Fuchs-Sondheimer (FS) formalism [53, 54] first used to describe electrical conductivity in thin films and later widely used to treat phonons [3, 52, 55]. Under the Fuchs-Sondheimer (FS) formalism, the geometric reduction arises from the influence of a (partially) diffuse surface on the MFP of a carrier (e.g. an electron). At any point in the structure, the influence of a surface at some distance from that point will cause a reduction in the mean free path due to the change in particle momentum when scattered off the surface. By integrating over all interior points and all directions to the surface, the reduction in the mean free path can be computed.

In our case, we have replaced the integration in the FS model with a MCRT procedure following McGaughey [56]. This replacement allows us to incorporate specularity and other geometric features into our model not directly available in the FS model. The procedure, outlined in Figure 2.4, is as follows. First, a d_{free} is pseudo-randomly selected from an exponential distribution with a mean of l_{bulk} and an initial direction is pseudo-randomly selected. In the second step, ray tracing is employed to determine the distance (l) from the initial point to the surface along the selected direction. If $d_{\text{free}} < l$ then the free path for that trial is d_{free}. If $d_{\text{free}} > l$ then we treat the interaction with the surface as either diffuse or specular. The selection is made pseudo-randomly based on the specularity parameter p: the fraction of specular events. The parameter p ranges from 0 (entirely diffuse) to 1 (completely specular) and is treated as a free parameter in the simulation. In the diffuse case, the free path for the trial is l. For specular events, a new direction is chosen by inverting the directional component normal to the surface, and ray tracing is continued with $d_{\text{free}} = d_{\text{free}} - l$ until either a diffuse event or d_{free} is reduced to below zero. In the case of ray tracing with specular reflections, the free path for the trial is the sum of all the ray lengths $l = l_1 + l_2 + \cdots + l_n$. Additional trials are calculated using the final position of the previous trial as the starting position for the new trial, and the reduced MFP is calculated as the average of the free paths of all the trials. For a specularity of 1 (i.e. no surface scattering) the MCRT calculations recover an $F_g = 1$, verifying the model. For the calculations in this report we consider the limiting case of a fully diffuse boundary ($p = 0$).

2.4.2 Impurity and Phonon-Phonon Scattering Rates

While grain boundary and geometric surface scattering are not affected by acoustic softening, impurity and phonon-phonon scattering can be. As both of these scattering rates have a non-linear dependence on the frequency (usually modeled as a power law), the effects on the scattering rate of a modification to the dispersion relation persist in the contribution to the MFP term resulting from both of these phenomena.

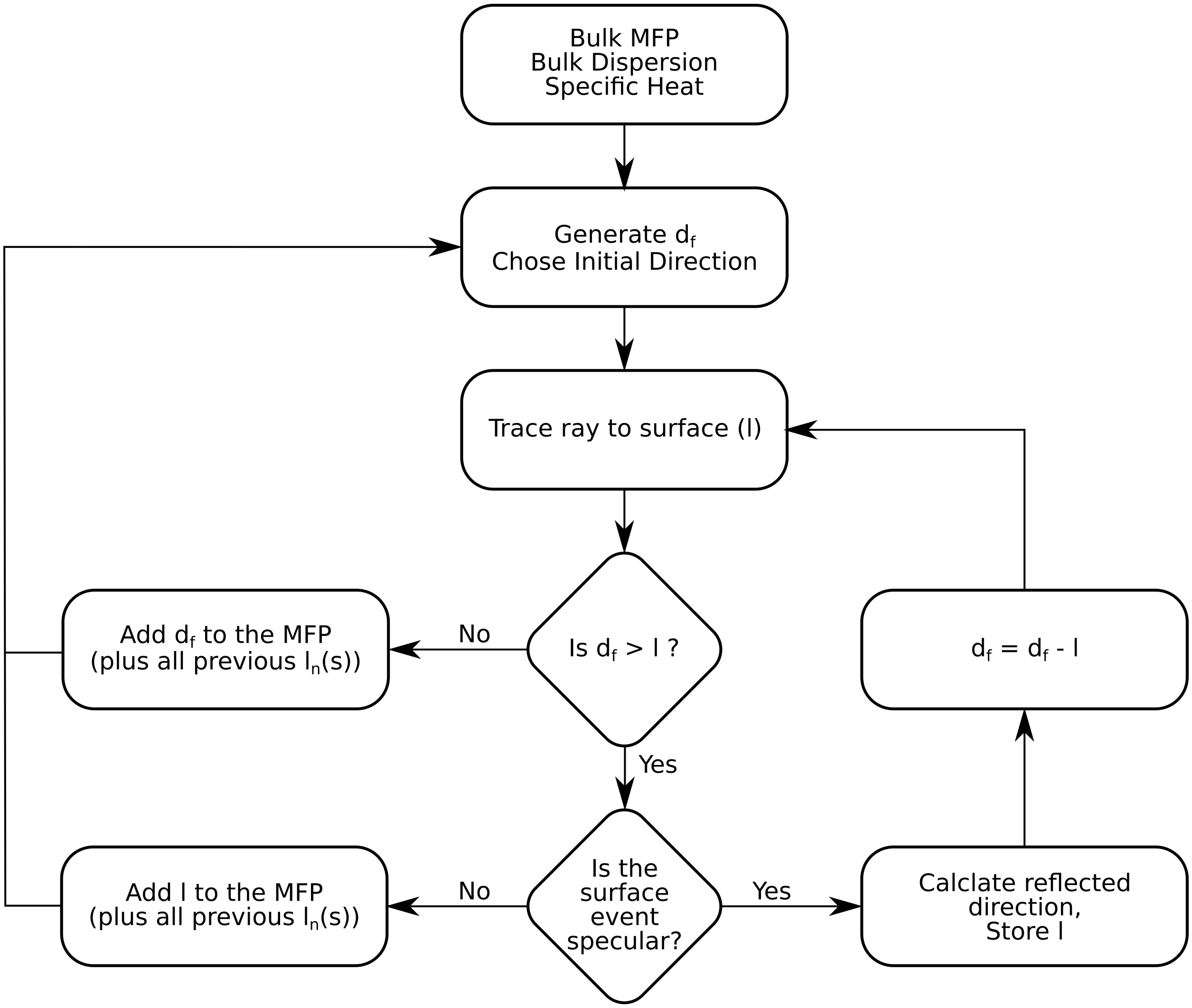

Figure 2.4: MCRT procedure

Silicon

To demonstrate this more clearly, we consider the Callaway models for scattering. These power law formulas, which we use for scattering in Si are [46, 48, 49]:

$$\tau_I^{-1}(\omega) = A\omega^4, \tag{2.11}$$

$$\tau_{pp}^{-1}(\omega) = P\omega^2 T \exp\left(\frac{-C_u}{T}\right), \tag{2.12}$$

where A, P, and C_u are fitting parameters that depend on the material and the phonon branch, and are taken from the literature [48, 49] where they are found to reproduce bulk Si thermal conductivity well. At the nanoscale, the choice of parameters should not have a large effect on our results as surface scattering will dominate. We do not include terms for normal scattering, and thus results for scattering at low temperatures should be viewed with caution. However, at low temperatures, the thermal conductivity is dominated by the heat capacity. Formulating these relations as MFPs then introduces the dispersion relation through the group velocity:

$$l_{\text{impurity}}(\omega) = \frac{v_g(\omega)}{A\omega^4}, \tag{2.13}$$

$$l_{\text{phonon-phonon}}(\omega) = \frac{v_g(\omega)}{P\omega^2 T \exp\left(\frac{-C_u}{T}\right)}. \tag{2.14}$$

Therefore, a modified dispersion due to acoustic softening will alter the MFP. This effect is captured in the MCRT.

For phonon-phonon softening, in addition to the group velocity ($v_g(\omega)$) and the frequency (ω), the fitting parameters are also modified by softening. The factor P can be expressed as $P = \frac{\hbar\gamma^2}{Mv^2\Theta_D}$ [57]. The Debye temperature, Θ_D, and the Grüneisen parameter, γ, are both proportional to the softening fraction F_s. This leads to a dependence on the softening factor of $1/F_s$ for P. Additionally, $C_u \propto \Theta_D$. Thus, for the phonon-phonon scattering, the softened phonon-phonon scattering is

$$\tau^{-1}_{\text{phonon-phonon}}(\omega) = F_s P \omega_b^2 T \exp\left(\frac{-F_s C_u}{T}\right), \tag{2.15}$$

where ω_b is the unsoftened phonon frequency.

For impurity scattering, a softened dispersion results in an increase in the MFP across the FBZ. This is in contrast to phonon-phonon scattering. In this case, the P parameter, the frequency, and the group velocity softening dependencies cancel out, leaving only the effect of softening on C_u. This results in a small decrease in the MFP from softening. For the $\tau \propto \frac{1}{\omega^4}$ behavior calculated by Ward and Broido[58], the frequency dependence on softening would in contrast cause an increase in the MFP. As discussed below and seen in Figure 2.6 the difference between the two models, when incorporating surface scattering, should be small.

To examine the combined effects of impurity and phonon-phonon scattering in Si we use a system without surface scattering (where the only geometric scattering included is a grain-boundary scattering term) and incorporate uniform softening (Figure 2.5). In this system the effects of phonon-phonon scattering dominate, and the MFP is reduced, by up to 20%. However, for the major portion of the FBZ, it is clear that the combined MFPs are much longer than the characteristic size of the nanostructures that we are interested in. For structures where we would see softening of this degree, we expect that surface scattering will occur on a size scale of around 10^{-8} m (10 nm), where the MFPs from the combined phonon-phonon and impurity scattering are on the order of approximately 10^{-8} m to 10^{-5} m.

To demonstrate the characteristics of softening effects in Si on MFP as a function of wave vector in a structure with a sufficiently small characteristic size, we add boundary scattering to the MFP via Matthiessen's rule. This is akin to a round wire with a diameter equal to the characteristic size. For the structures that show softening experimentally, and which we wish to investigate, the characteristic size is between 20 nm and 40 nm. The effective MFP

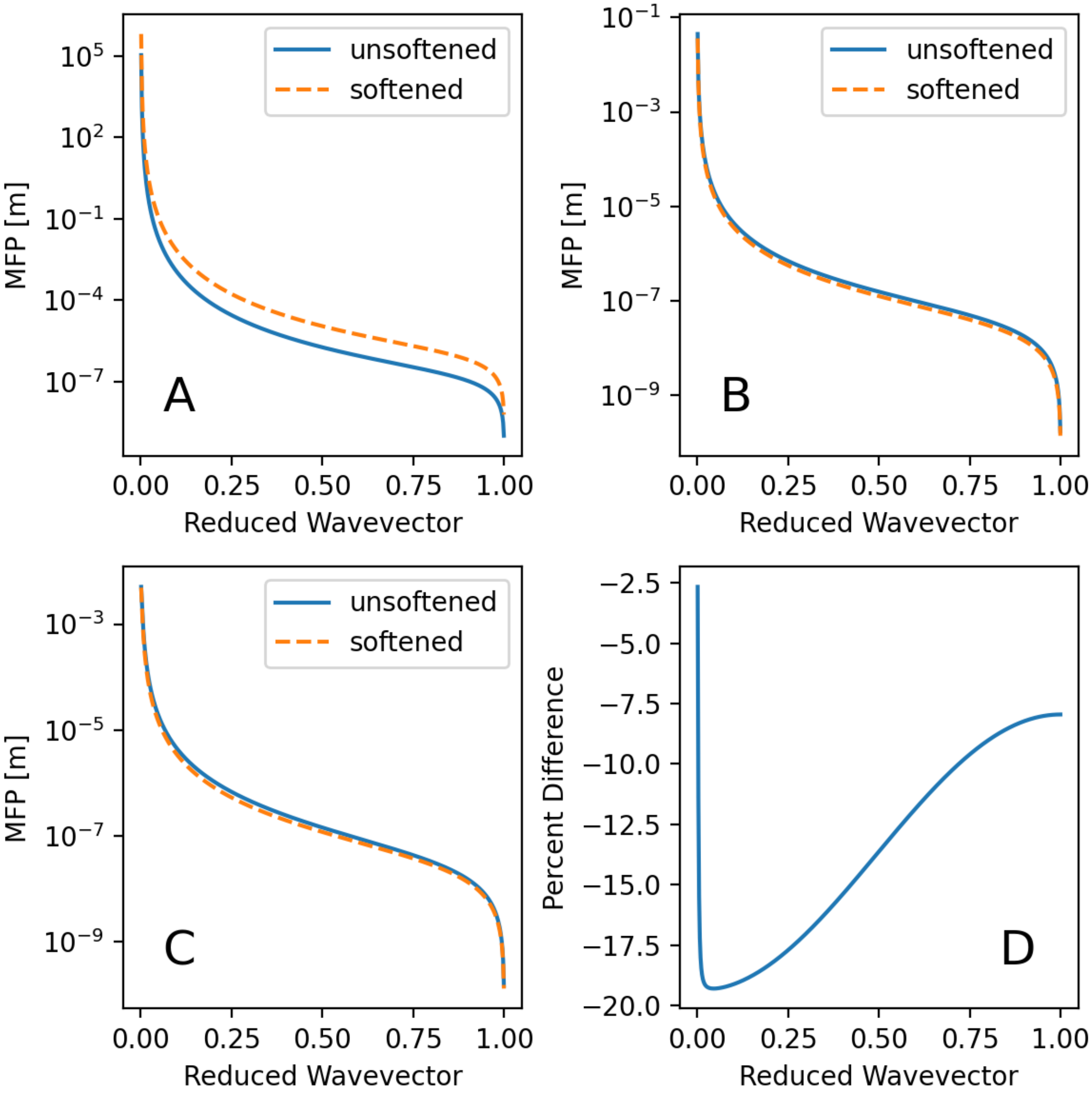

Figure 2.5: MFP as a function of reduced wave vector for softened and un-softened silicon, $F_s = 0.44$ at 300K, this softening corresponds to a wire with a diameter of 20 nm. A: impurity scattering MFP term, B: phonon-phonon scattering MFP term, C: MFP from combined impurity and phonon-phonon scattering, D: difference between softened and un-softened case in subfigure C

as a function of the reduced wave vector is plotted in Figure 2.6. Since the shortest MFP component will dominate the total MFP, the inclusion of a nanoscaled surface scattering term results in that term dominating the MFP. Consequently, the influence of softening on the MFP is diminished. For a 28 nm characteristic size, the reduction in the MFP is less than 2% for all wave vectors. For a characteristic size of 20 nm, the reduction in the MFP never exceeds 12% for any wave vector.

ZnO

In ZnO, for the MFP we adopt the formulations used by Wolf and Martin for fitting low-temperature bulk ZnO thermal conductivity and for modeling the thermal conductivity ZnO films respectively[59, 60]. Here scattering is composed of several terms including surface scattering, phonon-phonon scattering, impurity scattering, and dislocation scattering. As we are interested in nanowires, where there should be few dislocations, we ignore the dislocation scattering rate. The pertinent scattering rates then become

$$\tau^{-1} = \tau^{-1}_{\text{boundary}} + \tau^{-1}_{\text{phonon-phonon}} + \tau^{-1}_{\text{impurity}}, \tag{2.16}$$

$$\tau^{-1}_{\text{boundary}} = \frac{v_g}{D}, \tag{2.17}$$

$$\tau^{-1}_{\text{phonon-phonon}} = \left(\frac{P}{F_s} \exp\left(\frac{-F_s \Theta_D}{4T} \right) + C \right) \omega^2 T, \text{and} \tag{2.18}$$

$$\tau^{-1}_{\text{impurity}} = A\omega^4. \tag{2.19}$$

We note that while the surface scattering rate is dependent on the softened phonon group velocity, the MFP from boundary scattering remains independent of the group velocity (as discussed above).

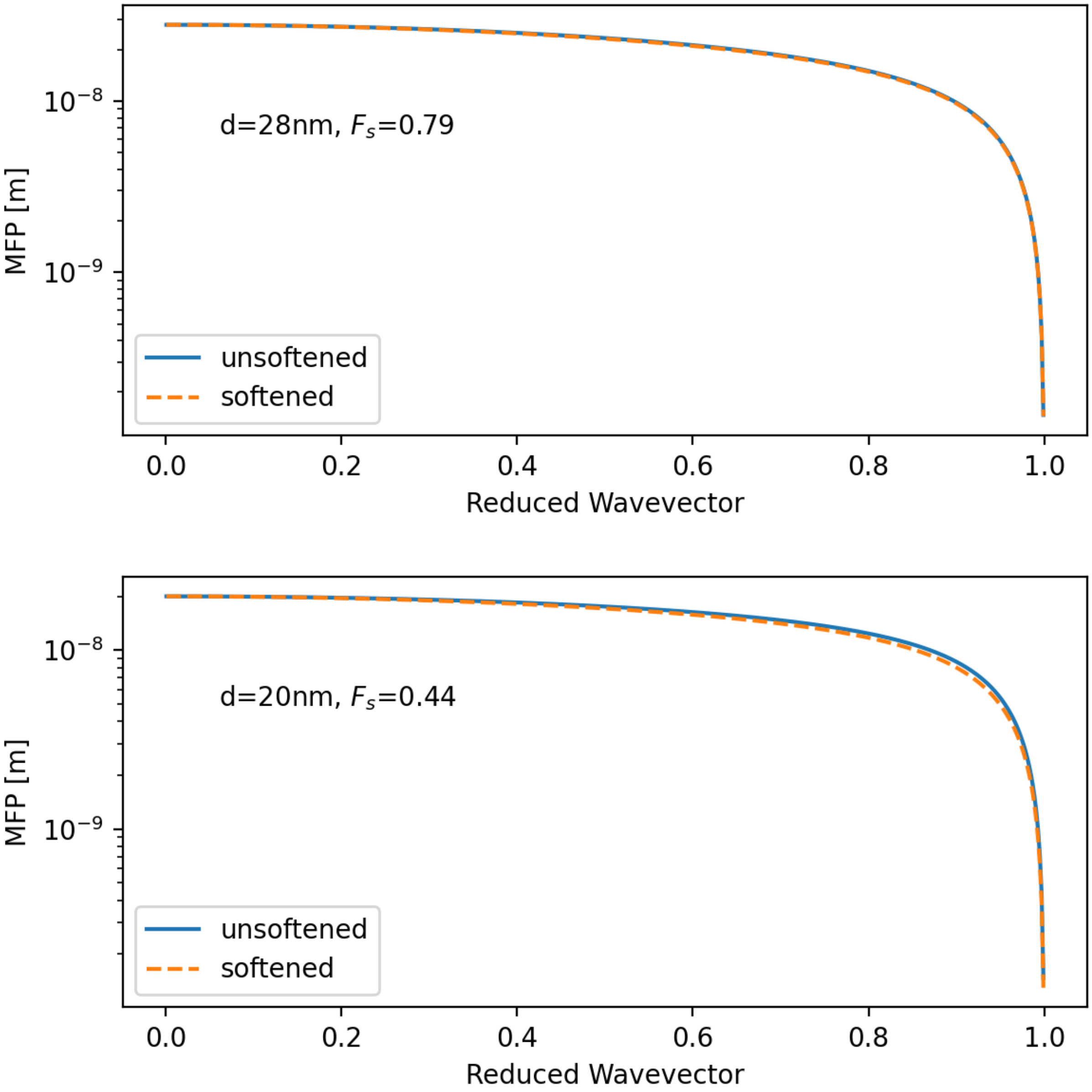

Figure 2.6: Spectral MFP with and without softening **(top)** for a structure with a characteristic size of 28 nm and $F_s = 0.79$, and **(bottom)** for a structure with a characteristic size of 20 nm and $F_s = 0.44$

2.4.3 Scattering Rate Parameters

With the above formulations for the scattering rate, we can parameterize the models for various materials to reproduce bulk thermal conductivity. These parameters for scattering are then used as the base for modeling the thermal conductivity of nanostructures. As discussed above, the fitting parameters for Si are taken from the literature [48, 49].

In ZnO, the BvKS model has not been parameterized, and there are limited sets of tabulated, temperature-dependent thermal conductivity. Most measurements of bulk thermal conductivity have been performed on sintered specimens, where porosity affects the measured results. Thus, to parameterize the BvKS model we fit it against parameterized models presented in the literature. Specifically, we fit our model against the Debye-Callaway model for bulk ZnO thermal conductivity as parameterized by Wolf and Martin[59] to fit thermal conductivity data between 1.1 K and 300 K:

$$\kappa = \frac{k_B}{2\pi^2 v}\left(\frac{k_B T}{\hbar}\right)^3 \int_0^{\theta_D/T} \tau \frac{x^4 \mathrm{e}^x}{(e^x - 1)^2} dx, \tag{2.20}$$

where θ_D is the Debye temperature, k_B is Boltzmann's constant, v the speed of sound, and $x = \hbar\omega/k_B T$. In order to fit bulk data, Wolf and Martin used the scattering rates, τ, in equation 2.16 as well as a dislocation scattering term: $\tau^{-1}_{\text{dislocation}} = Y\omega$ where Y is a fitting parameter related to the dislocation density.

Using the parameterization of the Debye-Callway model from Wolf and Martin, we fit the BvKS model against the predicted thermal conductivities in a temperature range from 1 K to 400 K. The resulting scattering parameters are presented in Table 2.1. As seen in Figure 2.7 the resulting parameters reproduce the bulk thermal conductivity well across the temperature range. However, the parameters for the BvKS model underpredict thermal conductivity at 300 K by approximately 15% when compared to the Debye-Callaway model. The consequences of this when comparing the BvKS model with MD data are discussed in Chapter 4.

	B [s/ K]	C [s/ K]	I [s^3]	Y
Wolf and Martin[59]	4.7×10^{-19}	2.8×10^{-20}	1.7×10^{-44}	1.5×10^{-6}
BvKS All Temperature	3.28×10^{-19}	1.73×10^{-20}	2.83×10^{-44}	
BvKS High Temperature	1.71×10^{-19}	1.02×10^{-19}	1.20×10^{-44}	

Table 2.1: Parameter values resulting from fit of thermal conductivity to bulk ZnO. The "All Temperature" fit is to thermal conductivities between 1 K and 400 K while the "High Temperature" fit is to thermal conductivities between 200 K and 400 K.

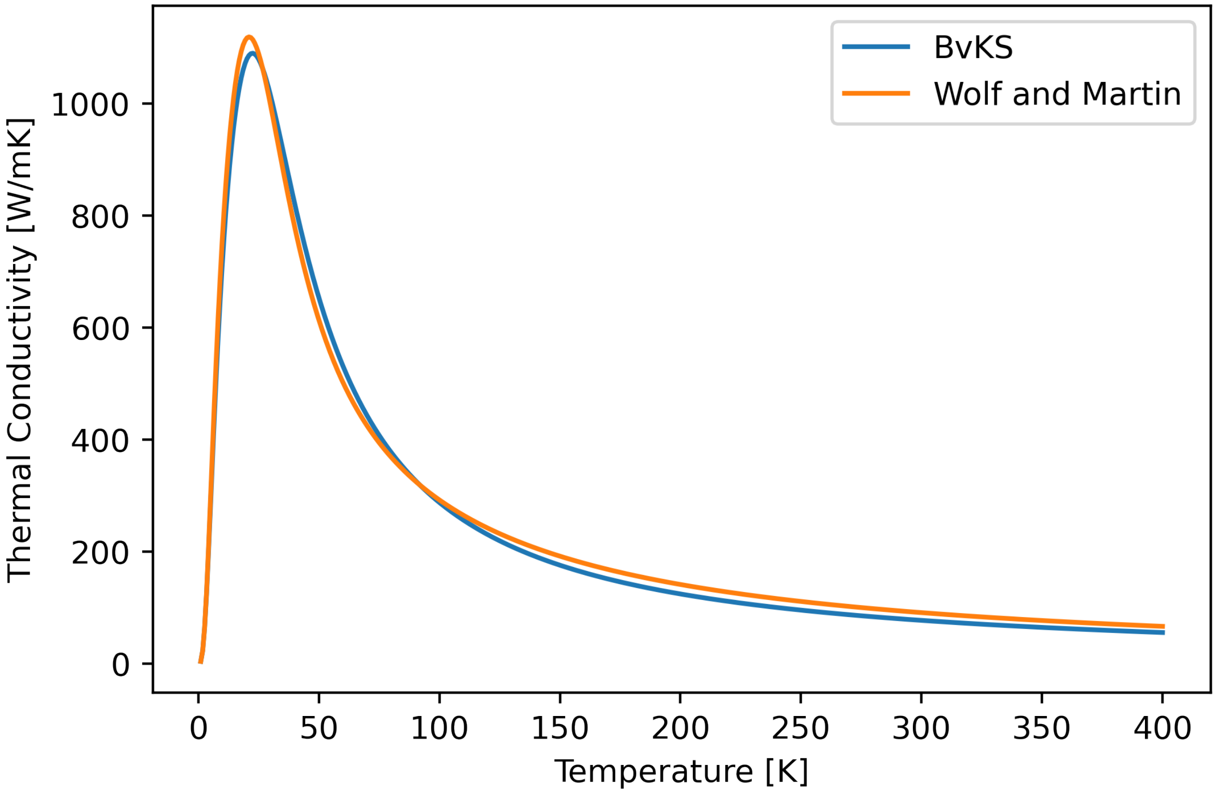

Figure 2.7: Bulk thermal conductivity calculated with the Debye-Callaway model parameterized by Wolf and Martin[59], and with the BvKS model using the "All Temperature" parameters (Table 2.1).

2.5 Heat Capacity

In addition to the scattering rate, a change in phonon frequency and thus in phonon energies, also affects the heat capacity. In general, the reduction in the frequencies of phonons will result in a reduction in the energy of phonons with high wavevectors, and thus an increase in the occupation of those states at a given temperature. Deriving a model for heat capacity using a spherical integration up to the cutoff wavevector, we have for each wavevector q [61]:

$$C_v(q) = \frac{3\hbar^2}{2k_B\pi^2}\frac{1}{T^2}\frac{q^2\omega^2(q)e^{\hbar\omega(q)/k_BT}}{(e^{\hbar\omega(q)/k_BT}-1)^2}. \tag{2.21}$$

Examining the spectral heat capacity across the FBZ, we see that softening should result in a slight increase in the spectral heat capacity, especially for longer wavevectors (Figure 2.8), and a slight decrease for stiffening (Figure 2.9). These effects are more intense at lower temperatures. Comparing the magnitude of the effect of acoustic softening/acoustic stiffening on the heat capacity with the magnitude of effect on the MFP at room temperature, the effect on the heat capacity is much smaller.

As the heat capacity is responsible for a large portion of the temperature dependence of thermal conductivity, examining the temperature dependence of the heat capacity and the effect of softening on it become interesting. In Figure 2.10 we plot the heat capacity as a function of temperature for a softened Si nanowire and note that there are significant changes in the heat capacity with softening. At low to intermediate temperatures, the heat capacity is significantly increased by the softening. This increase is mostly due to increased occupation numbers at low temperatures for the softened case, offsetting the decreased phonon energy. At higher temperatures, as expected, both heat capacities converge; at room temperature, the heat capacity is increased by 7% over the unsoftened case for $F_s = 0.44$.

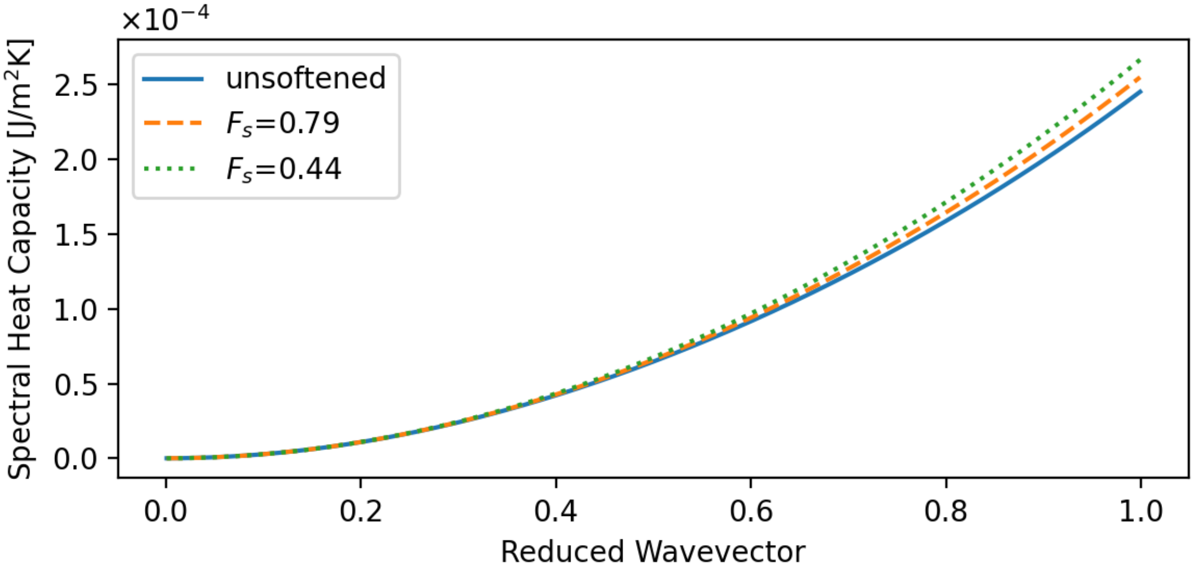

Figure 2.8: Heat capacity as a function of reduced wavevector with and without softening in a Si nanowire at 300 K

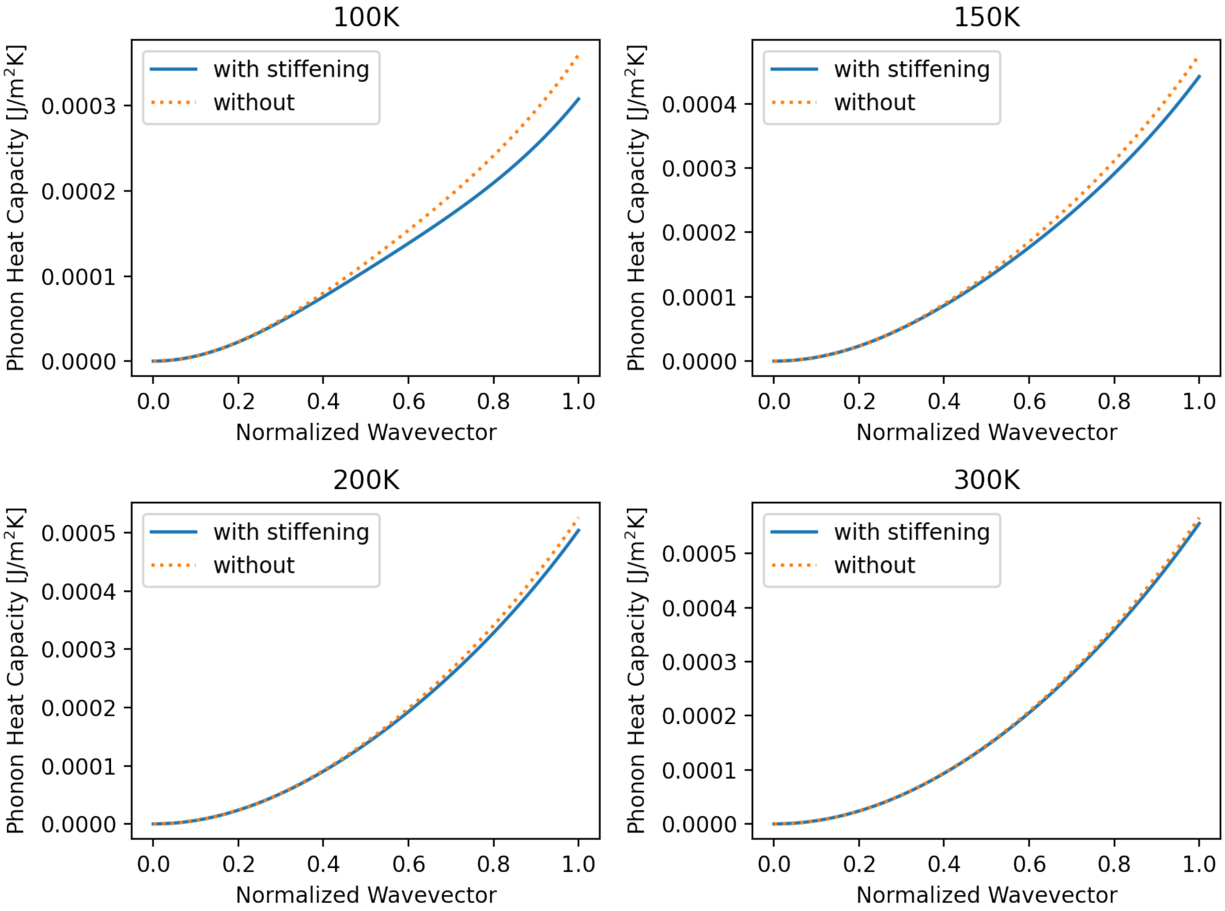

Figure 2.9: Heat capacity as a function of reduced wavevector with and without stiffening at multiple temperatures in a ZnO nanowire

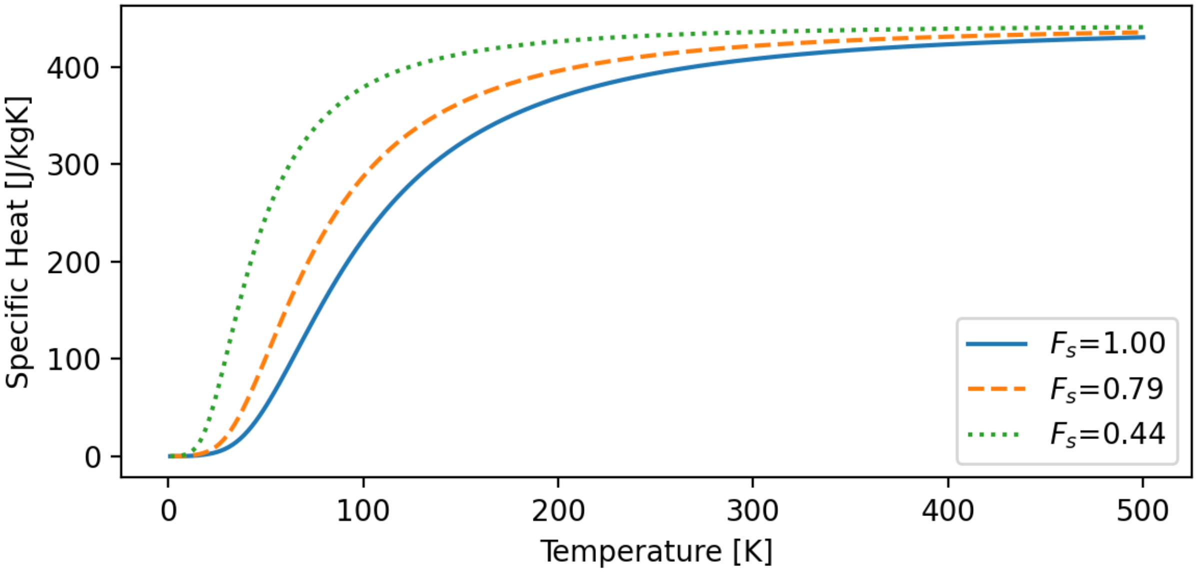

Figure 2.10: Heat capacity as a function of temperature with equivalent to 28 nm and 20 nm diameter wires ($F_s = 0.79$ and $F_s = 0.44$) and without softening

Chapter 3

Molecular Dynamics

While modeling can provide a number of insights into the effects of acoustic stiffening and acoustic softening on the thermal conductivity of nanowires, the models are still limited by their empirical nature. As will be discussed in Chapter 4, the scattering rates can play an important role in the competition between different stiffening modes. Unlike these models, in molecular dynamics, scattering arises as an intrinsic result of the simulation method. Additionally, the acoustic softening and acoustic stiffening in MD are less subject to experimental uncertainties, such as slippage at the ends of nanowires, or twisting of the sample.

Molecular dynamics simulations are a classical simulation of materials. In these simulations, atoms are treated as particles that exert a position dependent force on each other. By integrating Newtons laws of motion, the trajectory of the atoms as a function of time can me simulated. From these trajectories, statistical methods can be used to extract a number of properties such as stress, temperature.

For this work, I have used the LAMMPS software package for MD simulation [62]. This software is provided by Sandia National Laboratory and has seen active development since the 1990's.

3.1 Interatomic Potentials

To model a material in MD we first require an interatomic potential that describes the forces exerted by atoms on each other. In silicon, one well known potential is the Tersoff potential [63–65]. Although other interatomic potentials are available for Si, such as Stillenger-Webber

(SW) potentials, a comparison between Tersoff and SW potentials has show that the Tersoff potential more accurately predicts thermal conductivity [66]. The Tersoff potential describes energy between a pair of atoms as the sum of attractive and repulsive terms,

$$E_{ij} = f_C(r_{ij})[f_R(r_{ij} + b_{ij} f_A(r_{ij})], \tag{3.1}$$

where r_{ij} is the distance between the pair of atoms i and j and f_R and f_A are the repulsive and attractive terms which decay exponentially with distance. f_C is a smooth cutoff function that limits the distance of interactions. This limit to the interaction distance is important to allow MD simulations to remain computationally tractable. The factor b_{ij} is the bond-order term. This term encodes the changes to the attractive force experienced by an atom in different environments (with different coordination numbers). The parameters used for Si come from Munetoh et al. [67] and have been used in a number of studies of thermal conductivity in Si nanostructures [68–70].

For ZnO a Buckingham-style potential,

$$E_{ij} = A \exp \frac{-r_{ij}}{\rho} - \frac{C}{r_{ij}^6} + E_{long}(r_{ij}), \tag{3.2}$$

where the long range Coulombic interactions, $E_{long}(r_{ij})$, are computed using the Wolf summation as modified by Fennell and Gezelter [71]. Unlike the short-range terms, representing covalent bonding, Coulombic interactions do not decay fast enough to employ cutoff terms, necessitating the use of such a summation. Parameters for the Buckingham potential are taken from the work of Binks [72]. These parameters have been used in a number of ZnO studies and have found good agreement between experimental and computational values for the size dependence of the elastic modulus and other mechanical properties [27, 73], and have been used in studies of thermal conductivity in a number of ZnO nanowire systems [42, 44, 45]. At the surfaces, the reduced coordination number, specifically the absence of atoms on one side, results in a change in the equilibrium distance between atoms. As the equilibrium distance decreases, a different portion of the interatomic potential is sampled by the atom's motions, increasing the stiffness of the potential. Unlike the Tersoff potential, the Buckingham-style potential used for ZnO here has no explicit dependence on coordination number or bond order. However, using this potential, the expected decrease in the bond length from a decrease in coordination number has been observed in MD simulations [27].

3.2 Building Nanostructures

3.2.1 Silicon Nanoribbons

For thermal conductivity calculations in silicon, individual nanoribbons were modeled as slabs of Si atoms in a perfectly crystalline lattice. Slabs were prepared with cross sectional dimensions of 4×4, 4×8, and 4×16 unit cells. Slabs were prepared with three conduction region lengths for each cross section (Figure 3.1) to implement the scaling methodology described below (Section 3.3). The lattice was equilibrated for 3×10^5 timesteps in the NVT ensemble to prepare the system for adding heat. Shrink-wrapped boundaries were applied in the directions normal to the wire's surfaces (i.e. parallel to the direction of transport). The wire was then quenched to the simulation temperature (between 200 K and 400 K, depending on the particular simulation) over 2×10^5 timesteps, and then equilibrated at the simulation temperature for a further 2×10^5 timesteps. For these simulations a timestep of 0.7 fs was used.

To investigate the role of surface specularity, we have also built ribbons with increased surface roughness by melting and quenching the outer layers of the ribbons. This approach has been taken by a number of groups investigating amorphous silicon and core-shell nanowires with molecular dynamics [74–77]. The roughening is accomplished by heating the outermost unit cells of a crystalline nanoribbon to 2500 K for 3×10^5 timesteps using a Nose-Hoover thermostat—-melting the outer surface. The system is then quenched to 1200 K and the whole system is run for another 3×10^5 timesteps. At this point, a few of the atoms on the surface of the ribbon may have evaporated from the wire and drifted beyond the

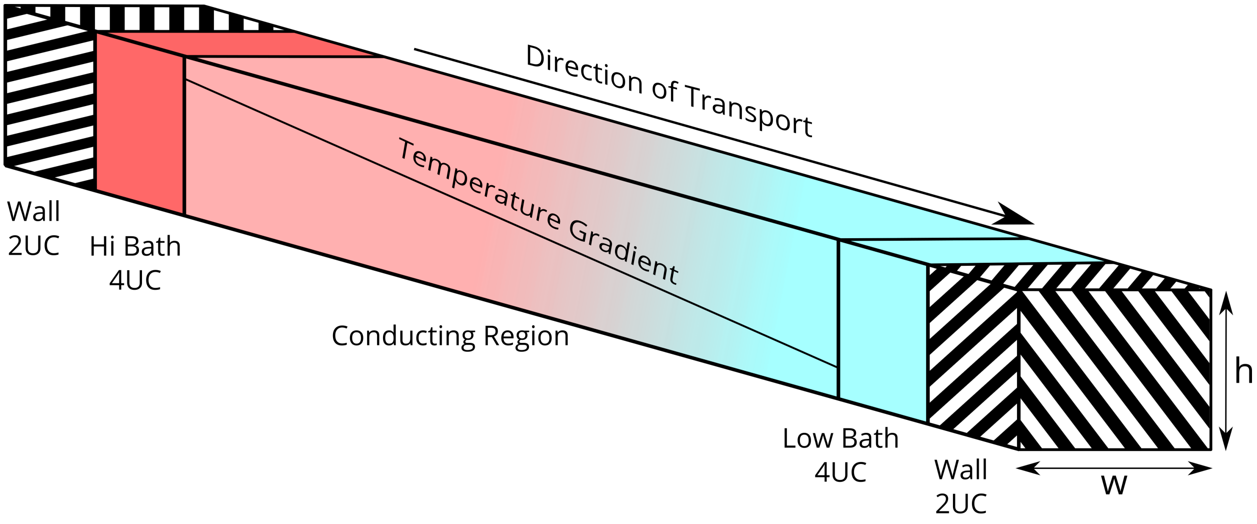

Figure 3.1: Schematic of NEMD thermal conductivity simulations

force cutoff; these atoms are removed from the simulation for computational efficiency as they do not contribute to the thermal conductivity of the nanoribbon. The system is then equilibrated for another 3×10^5 timesteps at the simulation temperature (between 200 K and 400 K). Equilibrated wires with smooth and roughened surfaces can be seen in Figure 3.2.

3.2.2 ZnO nanowires

For the ZnO simulations, nanowires are prepared using a heat-and-quench procedure from the idealized structure to allow the surfaces to relax. Nanowires of appropriate dimensions are first constructed and then heated to 1200 K over 30 ps. The wires are held at this temperature for 30 ps and allowed to cool to the test temperature over 30 ps and held at the final temperature for 100 ps before data for thermal conductivity is collected. During this equilibration procedure, the wires are allowed to relax along the wire length.

3.3 Non-Equilibrium Thermal Conductivity Calculations

For thermal conductivity simulations, we employ a non-equilibrium molecular dynamics (NEMD) technique. This approach calculates thermal conductivity by imposing a temperature gradient across the system and monitoring the heat flow required to maintain the

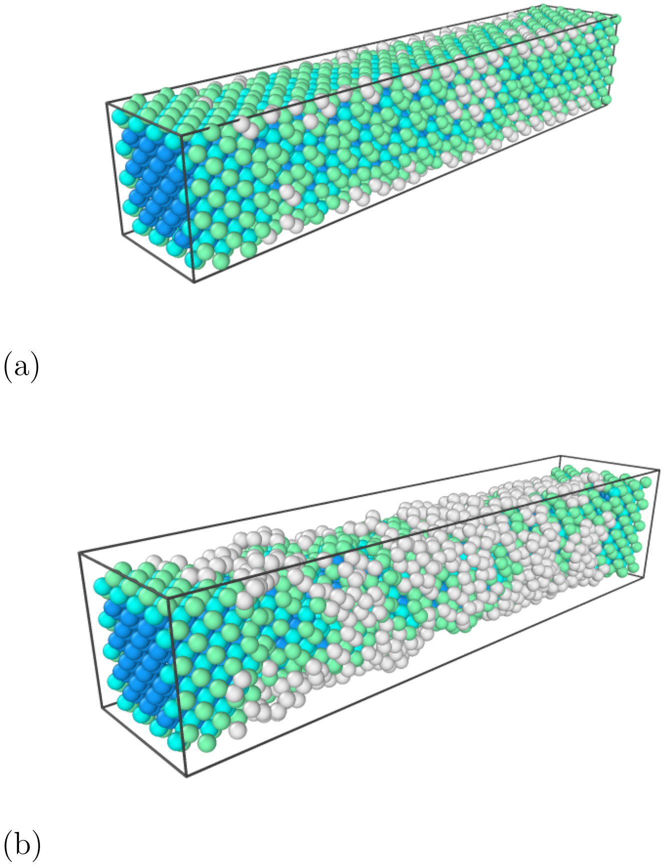

(a)

(b)

Figure 3.2: Smooth (a) and roughened (b) nanoribbons where the color indicates atomic structure: Dark blue indicates atoms in a diamond cubic structure, while teal colors indicate that the atom has diamond cubic neighbors. White atoms are not in a diamond cubic structure [78, 79].

gradient. Thermal conductivity is then computed using Fourier's law,

$$\mathbf{q} = -\kappa \frac{dT}{dx}, \tag{3.3}$$

where $\frac{dT}{dx}$ is the temperature gradient, and $\mathbf{q}$ the heat flux.

For silicon nanostructures, once the wires were prepared, the thermal conductivity was calculated as follows. At each end of the wires a 2 unit-cell thick wall of stationary atoms is created by freezing the atoms, and, directly inside of each wall, a 4 unit-cell thick heat bath is defined (Figure 3.1). To calculate thermal conductivity with NEMD, a temperature gradient is imposed along the nanoribbon by holding the heat baths at the simulation temperature $\pm 10\,\mathrm{K}$. This creates a temperature difference of $20\,\mathrm{K}$ across the wire. The simulation was then advanced for 5×10^6 timesteps to allow the system to reach steady state.

Once the system reaches steady state, temperatures along the length of the ribbon, as well as the energy required to maintain the heat bath temperatures are collected for another 5×10^6 timesteps. During the NEMD calculations, the heat baths are integrated using the Nose-Hoover thermostat, and the conducting region is integrated without the thermostat. The heat flux is then computed from the cross-sectional area and the energy added/subtracted from the heat baths. The effective thermal conductivity can be computed via Fourier's law. For this study thermal conductivity was computed as the average of the thermal conductivity from four separately initialized wires using the data from the last 4.85×10^6 timesteps.

Because we want to investigate the effects arising from phonon scattering at the nanoribbon surface and compare this to experiment, we want to remove reductions in thermal conductivity caused by scattering at the heat baths. Therefore, we employ a well-established scaling method [80, 81] to extract the thermal conductivity of an infinitely long nanoribbon from a set of different finite-length MD calculations. To accomplish this, we fit a line to the $1/\kappa$ vs. $1/L$ data. The intercept of $1/\kappa$ when $1/L$ is zero gives us the thermal conductivity for an infinitely long wire; examples of this process are shown in Figure 3.3. Unless other-

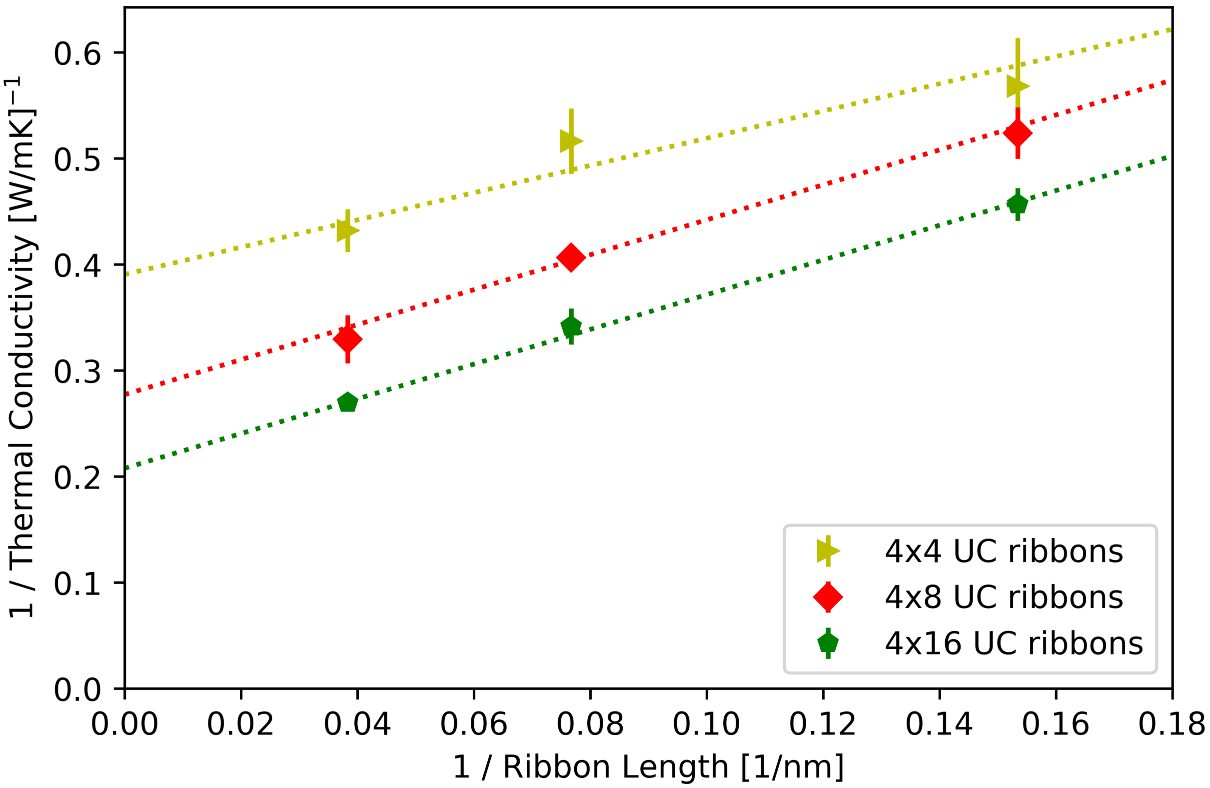

Figure 3.3: Example of scaling thermal conductivity to infinite lengths. Data shown here is for smooth surfaced ribbons at 400 K. The infinite length thermal conductivity is extracted from the y-intercept using a linear fit to the thermal conductivity from MD.

wise noted, all thermal conductivities from MD reported in this report are scaled to infinite nanoribbon lengths.

Similarly, to the Si nanoribbons, after ZnO nanowires have been constructed, the end regions of the wires are frozen, and high and low temperature heat baths are defined at the ends of the wire immediately adjacent to the frozen sections. These baths are held at ±10 K of the average temperature, and the system is allowed to come to a steady state over 0.1 ns. The temperature difference (ΔT) and energy required to maintain the bath temperatures (q) were then averaged over a period of 1 ns. Thermal conductivity was then calculated using Fourier's law. ($k = qL/A\Delta T$, where L is the length of the wire, and A is the cross-sectional area.)

For each diameter of the ZnO nanowires, the thermal conductivity of an infinitely long

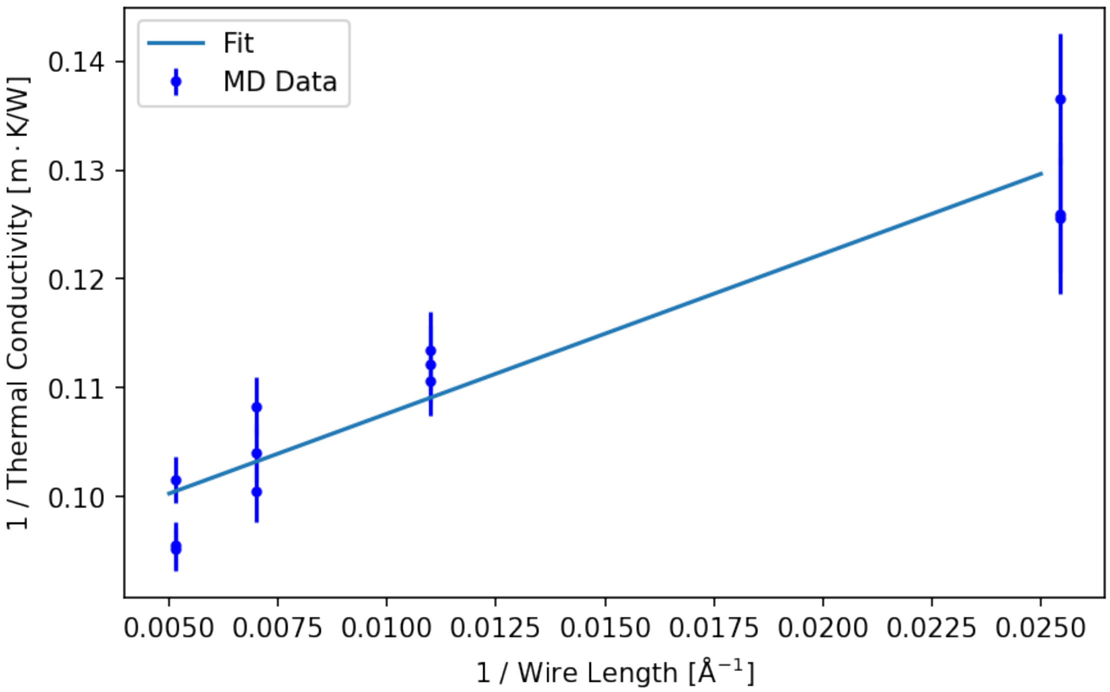

Figure 3.4: Example of length scaling of thermal conductivity for NEMD method for a 6.9 AA diameter ZnO nanowire at 300 K.

wire is approximated by simulating the thermal conductivity of wires of multiple lengths. Thermal conductivity as a function of wire length is then fit with $1/k = m/l + b$, where $1/b$ is the thermal conductivity of an infinitely wire[80, 81] as for Si. An example of this scaling for ZnO nanowires is seen in Figure 3.4.

3.4 Wave packet simulations

To directly observe the effects of surfaces on the phonon velocity in Si nanostructures, we turn to wave packet simulations. In wave packet simulations, a localized phonon wave packet is constructed from one of the branches of the phonon dispersion by controlling the displacement of atoms at one end of the simulation domain. As the wave packet propagates through the simulation domain a number of transport characteristics may be calculated. In particular, wave packets have been widely used to analyze phonon transmission and reflection at interfaces [70, 82–86], boundary scattering [87], and thermal rectification [88].

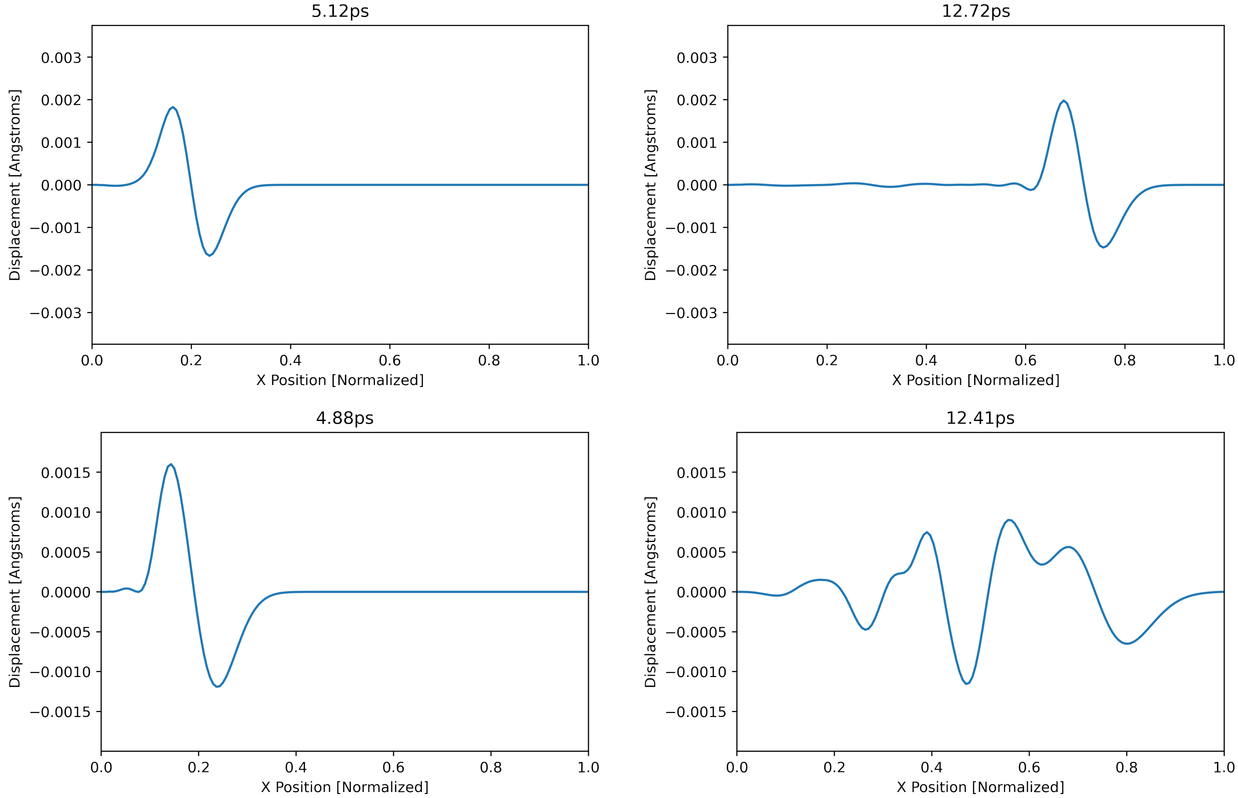

Figure 3.5: Displacement as a function of position along a wire as a function of the distance along the nanostructure. Top two images are for a 4×4 UC square wire, bottom two images are for a 8×16 UC nanoribbon

In these simulations, a wave packet is introduced into various sized wires (ranging from 2×2 UC wires to 32×32 UC wires), and the displacement of atoms is monitored as the wave packet propagates through the system. From these displacements, peaks are identified, and the position of the peak is determined as a function of time. With that, the velocity is calculated. Examples of displacements can be seen in figure 3.5. Looking at low frequency wave packets, we expect phase and group velocity to be approximately equal, and thus this reduction in phase velocity be similar to a reduction in the group velocity and its effects on the thermal conductivity.

These structures are prepared by creating a block of silicon with the desired cross section, with periodic boundaries in the z direction, and shrink wrapped boundaries in the other directions. For films, shrink-wrapped boundaries are only applied in the x direction, with periodic boundaries in the other two directions. The energy of the wire is minimized, and the box is allowed to relax in the z direction to maintain zero pressure in that direction. We then simulated annealing the wires by heating them to 500 K and then cooling them over a number of steps to 0.001 K. This is accomplished over five stages of 1×10^5 timesteps timesteps (with a timestep of 0.2 fs): holding at 500 K, cooling from 500 K to 1.0 K, holding at 1.0 K, cooling from 1.0 K to 0.001 K, and holding at 0.001 K. The system is then minimized again, allowing the box to relax in the z direction. The periodic boundary in the z direction is then changed to a shrink-wrapped boundary and walls are created by freezing a region 2-unit cells thick at either end of the wire. The system is then run at 0.001 K for a final 1×10^5 timesteps timesteps, the velocities zeroed, and the system minimized.

Once minimized wires are built, wave packets are introduced and allowed to propagate down the wire. The packets are created by moving the lower z wall following the equation:

$$z = z_0 A \sin(\omega(t - t_0)) exp(-(t - t_o)\eta^2), \tag{3.4}$$

where ω is the central frequency, A the amplitude, t_0 the center, and η the width of the wave packet. We then follow the wave packet by calculating the average displacement of slices of atoms in the z-direction over 25 timestep periods, allowing the system to evolve until the wave packet has reach far end of the wire, around 7.5×10^4 timesteps.

3.5 Elastic Modulus Calculations

To calculate the elastic modulus in the ZnO nanowires molecular dynamics can be employed in a method that is similar to macroscale tensile testing. To do this the wires are strained quasi-statically along the c-axis to a total of 0.005 mm/ mm over 1 ps. This is done by deforming the simulation box and re-scaling the atom positions. The wires are then allowed to relax for 30 ps and the virial stress is monitored. This process is repeated up to a total strain of 0.05 mm/ mm and the elastic modulus is extracted from the stress-strain curve constructed from all the simulation steps.

Chapter 4

Results

Now that we have laid the groundwork for examining acoustic softening and acoustic stiffening in nanowires, we can begin to explore how these effects manifest in the thermal conductivity of both Si and ZnO nanostructures.

4.1 Si Nanoribbons

We were motivated to examine the role of acoustic softening in Si nanoribbons by experimental results that measured both the thermal conductivity and the elastic modulus for several sizes of nanoribbons. Yang et al. [3] have examined two sets of nanoribbons with different thicknesses: a thick set with widths from 29 nm–211 nm and thicknesses of approximately 30 nm, and a thin set with widths from 46 nm–134 nm and thicknesses of approximately 20 nm. For the thick nanoribbons, the thermal conductivity was well modeled by geometric considerations that incorporate surface scattering in rectangular cross sections. This result follows similar trends from literature studies on films and wires in the 50 nm–200 nm size range. To do this in Si, we have employed both molecular dynamics and modeling to capture the effects on the thermal conductivity.

4.1.1 Molecular Dynamics

We initially investigated the thermal conductivity of silicon nanoribbons by employing a fully diffuse BvKS model without softening using MCRT to correct for the high aspect ratios, and compared the thermal conductivity obtained via MD at 300 K with the thermal conductivities reported for nanoribbons from Yang et al. [3] and from Park et al. [52], and for various other nanowire, thin film, and nanotube geometries [2, 36, 89] (Figure 4.1). We have plotted these as a function of S/V (surface area to volume) so both square or round wires and ribbons with high aspect ratios ($AR = w/h$) can be included on a single graph.

Directly comparing the effects seen in MD with the experimental results is suspect due to the difference in sizes between the two. We bridge these two regimes by including the results of several MCRT calculations with fully diffuse boundary conditions. With these boundary conditions MCRT captures the maximum possible reduction in thermal conductivity arising solely from surface scattering, placing a lower bound on the thermal conductivity due to geometric effects alone.

For all sets of data, the same trends are apparent: as S/V increases (i.e. the size decreases), the thermal conductivity is reduced as expected. The fully diffuse MCRT captures a large portion of these experimental results, with the values for Yang's thick nanoribbons[1], for the MD with roughened surfaces conducted here, and for a number of other films, wires, and ribbons lying between or just slightly above the values for diffuse MCRT with apsect ratios (AR) varying from 1 to 15. For the data sets that have thermal conductivity higher than that predicted by fully diffuse MCRT, we expect that the surface specularity is higher than for other data sets.

The other clear deviation of the experimental results from the fully diffuse MCRT occurs for structures above a S/V of approximately $0.1\,\mathrm{nm}^{-1}$. For these structures, the measured thermal conductivity is lower than that calculated with MCRT. While thermal conductivities that are higher than the diffuse MCRT are easy to incorporate into a geometric model with specularity, the suppression of the thermal conductivity below that given by a fully diffuse model indicates that other effects are at play. To that end we turn to acoustic softening.

---

[1] Aproximately 30 nm thick

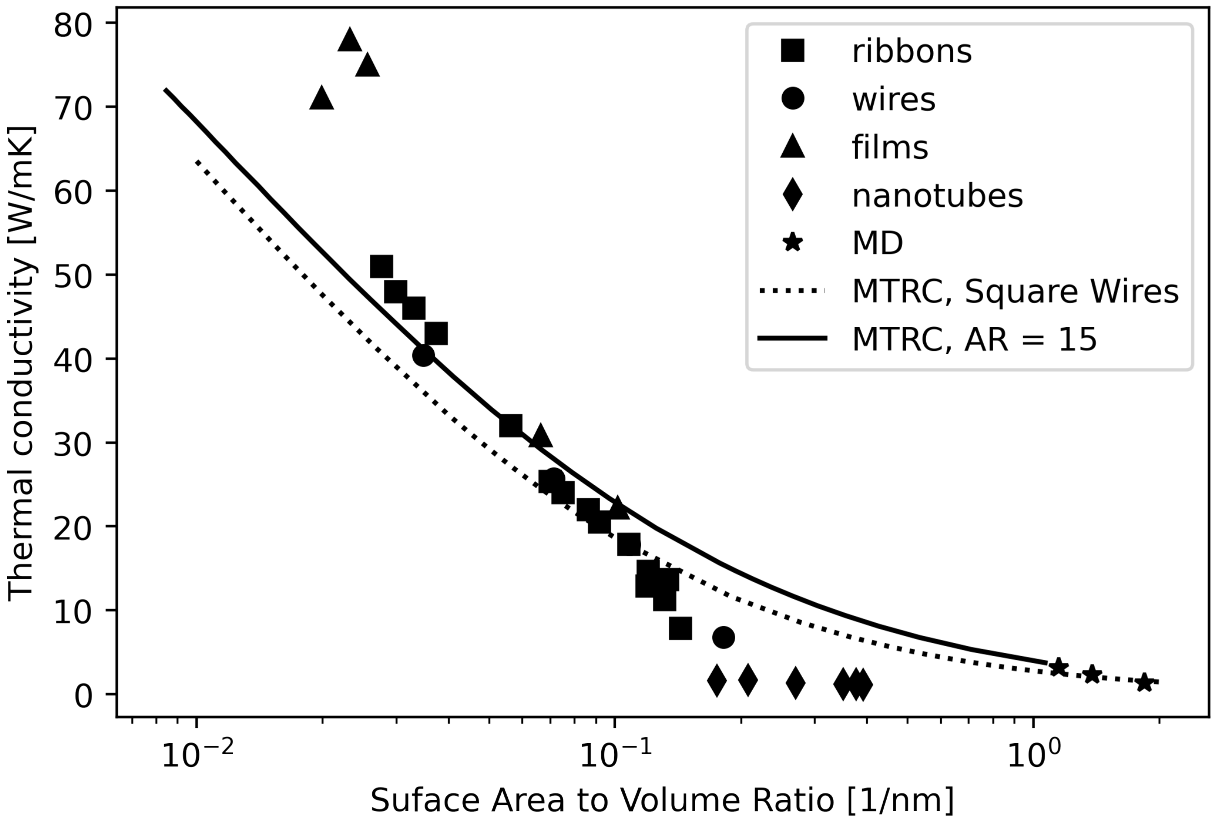

Figure 4.1: Thermal conductivity as a function of S/V form experiments and MD. Results from the literature are shown for ribbons [3, 52] (squares), wires [36] (circles), films [89] (triangles), nanotubes [2] (diamonds) and MD with roughened surfaces (current work, stars). MCRT calculations with ARs of 1 (dotted line) and 15 (solid line) are also show.

4.1.2 Wave Packet Simulations

Acoustic softening is a reduction in the acoustic phonon velocity arising from surface effects that reduce the effective Young's modulus of a nanowire. Numerous studies have worked to quantify and describe this reduction, however for thermal conductivity the change in the elastic modulus is an indirect proxy for phonon velocity. By utilizing MD wave packet simulations, we attempt to directly interrogate the phonon velocity in structures that may be subject to softening. Looking at square wires, ribbons, and films, we compute the phase velocity of low frequency ($\omega = 1$ THz) phonons. At low frequencies, we take the phase and group velocity to be approximately equal. We observe that the phase velocity of a longitudinal wave packet decreases from the bulk value ($7821 \pm 32\,\mathrm{m/s}$) to around $5000\,\mathrm{m/s}$ for a $2 \times 2\,\mathrm{UC}$ wire. The dependency is demonstrated in figure 4.2.

For wires with a square cross section, as the surface area to volume ratio increases (i.e. the wires decrease in size) the decrease in velocity occurs rapidly at first, and then levels off somewhere between a $8 \times 8\,\mathrm{UC}$ and $6 \times 6\,\mathrm{UC}$ wire. For smaller square wires, especially for the $2 \times 2\,\mathrm{UC}$ wire, the velocity again decreases, although at these sizes other effects may be contributing to the decrease in velocity. For films a similar pattern holds, with the velocity decreasing linearly with surface area to volume ratio until a wire size of about $8 \times 8\,\mathrm{UC}$ in size. After this point, the velocity levels off.

From these results we develop a simple model after the manner of core-shell models that splits the cross section of each wire into two parts, a surface region of a constant thickness and a core region. The velocity in the surface region is taken to be different than the bulk velocity, and the total velocity computed as the average of the core and surface velocities weighed by the area fraction of the core (X_C) and surface (X_S) regions respectively:

$$v_{\text{eff}} = v_C X_C + v_S X_S. \tag{4.1}$$

This model captures the plateauing at large surface area to volume ratios, as when a

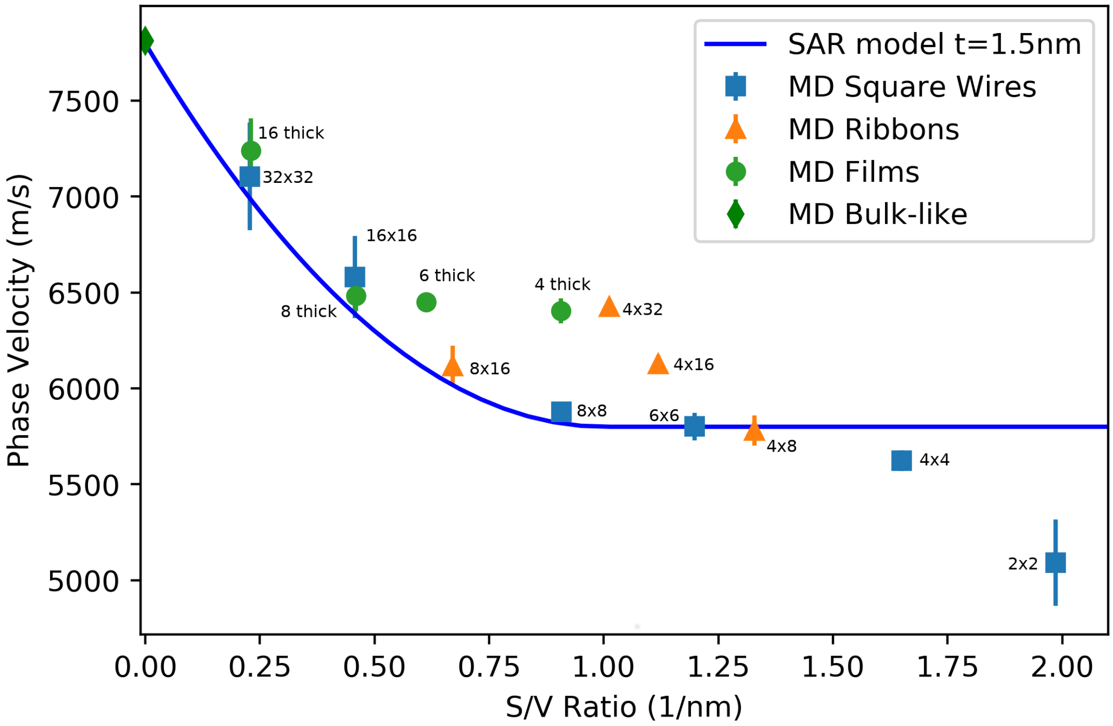

Figure 4.2: Phase velocity from various sized nanowires, ribbons and films from wave-packet simulations. Labels indicate the size of the nanostructures in unit cells.

dimension of the nanostructure reaches the thickness of the surface region $X_S = 1$ and $X_C = 0$. Additionally, the majority of the change in the surface region fraction occurs over about a decade of surface to volume ratio as can be seen in figure 4.3.

While a model with just core and surface components can capture the films and square wires pretty well, it cannot do so with the same parameters. Additionally, for ribbons, the MD data is between films and square wires, and is not captured. Since there appears to be two plateaus, one for films and one for square wires, we are motivated to introduce a third region to the model: corners. Thus, we compute the phonon velocity as,

$$v_{\text{eff}} = v_R X_R + v_C X_C + v_S X_S, \tag{4.2}$$

where v_{R} and X_R were the speed and area fraction of the corners.

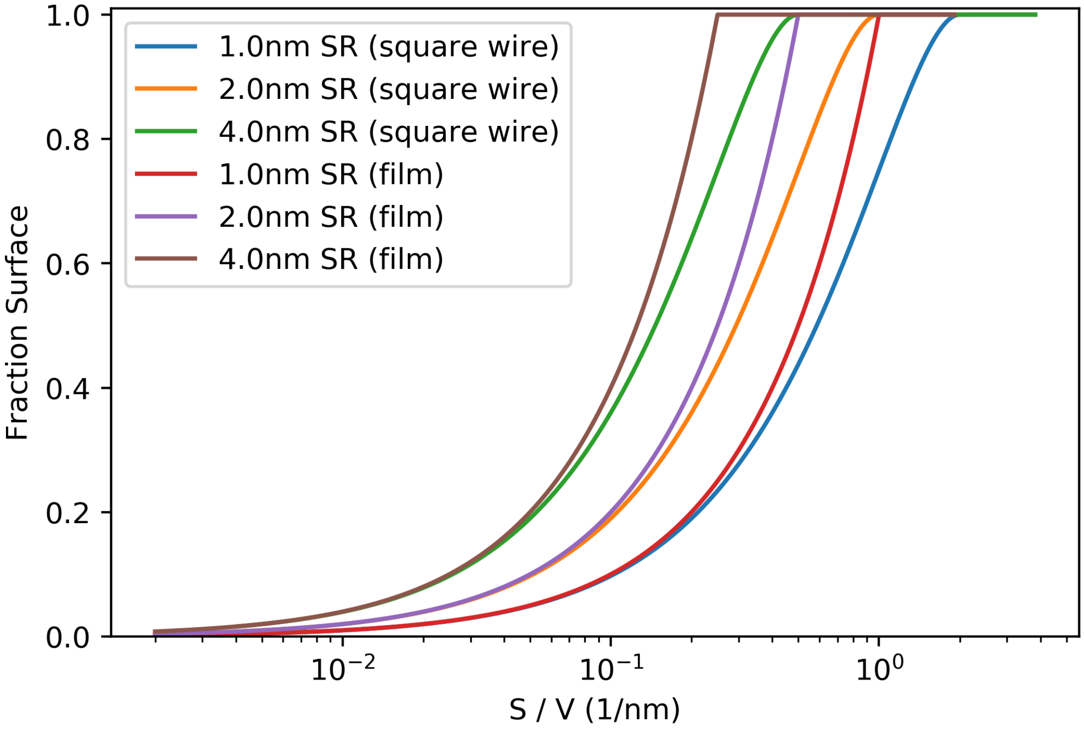

Figure 4.3: Fraction of nanostructure cross section in the surface region as a function of the surface to volume ratio.

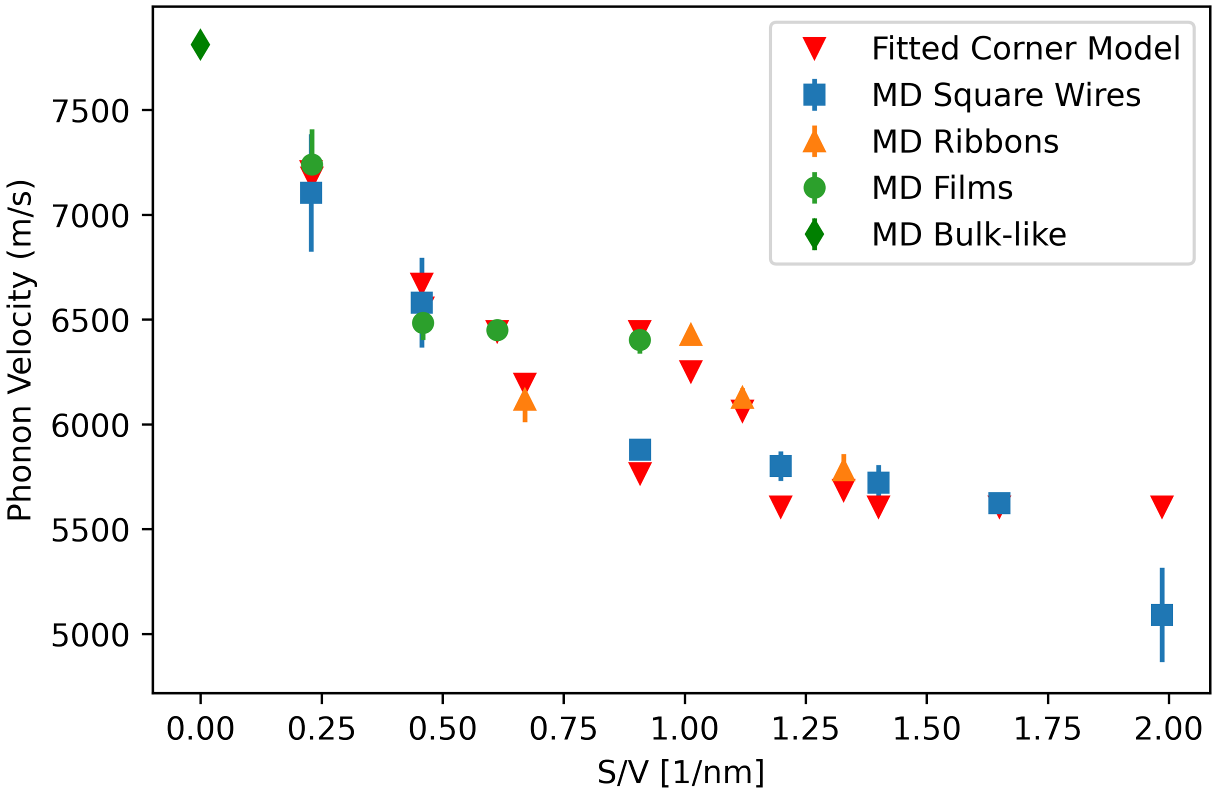

Figure 4.4: Phase velocity from MD fit with equation 4.2. Values from fit: $v_R = 5607 \pm 83\,\mathrm{m/s}$, $v_S = 6445 \pm 104\,\mathrm{m/s}$, and $t = 1.998 \pm 0.166\,\mathrm{nm}$

Fitting this model with the data from the MD wave packet simulations for films, square wires results in good agreement for almost all sizes (Figure 4.4). From the fitting parameters, it appears that in the corner region, the velocity is reduced by around 28% and in the surface region the velocity is reduced by around 17%.

Turning to the results from experiments, the ratio of the nanoscale phonon velocity to the bulk phonon velocity can be approximated from the measured nanoscale Young's modulus as

$$\frac{v_{\text{nano}}}{v_{\text{bulk}}} = \sqrt{\frac{E_{\text{nano}}}{E_{\text{bulk}}}}. \tag{4.3}$$

Comparing the velocities obtained by this method from Yang et al.'s data[3] with the MD results indicates that the experimental results expect softening to occur much more quickly with S/V than is seen in MD (figure 4.5). Unlike the MD results, the corner model doesn't

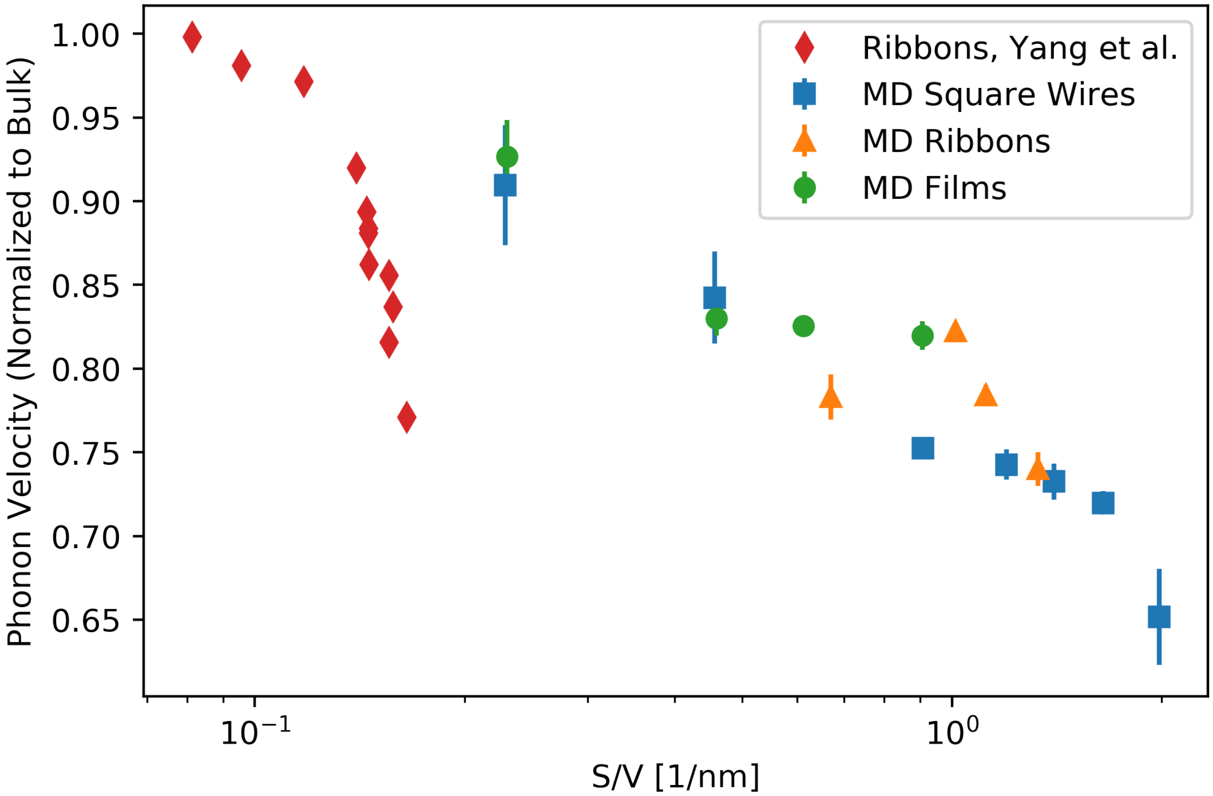

Figure 4.5: Comparison between speed of sound calculated using experimental measurements of the elastic modulus[3] and the phase velocity calculated from MD using wave packets.

fit the data from Yang et al. well.

4.1.3 Simple Acoustic Softening

The addition of specularity allows MCRT and other geometric models to predict the thermal conductivity in larger nanoribbons and nanowires; however, the addition of specularity cannot account for thermal conductivities seen in the smallest nanoribbons. A strong candidate for additional physics causing the reduced thermal conductivity is the acoustic softening effect. As has been widely reported, the elastic modulus for silicon nanostructures is observed to decrease with decreasing device size. From continuum theory the speed of sound can be computed as $v = \sqrt{\frac{E}{\rho}}$, where E is the Young's modulus and ρ is the density. Thus, if the Young's modulus is reduced, so too then is the speed of sound. The reduction in the group velocity due to a reduction in the Young's modulus can be computed as $F_s = \sqrt{\frac{E_{nano}}{E_{bulk}}}$. As this reduction in ratio is independent of the phonon wave vector for the approximation of the dispersion we use (the BvKS dispersion), when considering only the effect on the velocity it can be incorporated into the MCRT method simply as $\kappa_s = F_s \kappa_{MCRT}$, where the s subscript refers to softening.

In general, experimental measurements of Young's modulus indicate that softening effects become important when the dimensions of the systems are reduced below approximately 100 nm–150 nm (for example [13]). In Figure 4.6 we summarize the results of several investigations into this softening by plotting $E_{\text{nano}}/E_{\text{bulk}}$ as a function of S/V. In this graph we take $E_{\text{bulk}} = 180\,\text{GPa}$. We see that the softening observed across experiments seems to fall into two categories: (1) cluster of results with a $1/x$ type of trend, and (2) Young's moduli that are linear in S/V. In general these results indicate that for nanoribbons in the size range of Yang's thin ribbons, $E_{\text{nano}}/E_{\text{bulk}}$ should be between approximately 0.3 and 0.8. This translates to between a 10% to 45% reduction in thermal conductivity.

To incorporate softening effects into our MCRT we need to choose a model for softening that is a function of the size of our wires and ribbons. As an initial fit to experimental data, much of which comes from bending experiments, we use the core-shell model from Sadeghian for a film in bending [8]:

$$\frac{E_{\text{ribbon}}}{E_{\text{core}}} = \left(1 + 6\frac{h_0}{h}\right)\left\{\frac{h^3 + \frac{E_{\text{shell}}}{E_{\text{core}}}[8t^3 + 6h^2t + 12ht^2]}{(h+2t)^3}\right\}, \tag{4.4}$$

where h_0 is a characteristic length set by the ratio between the Young's modulus and the surface elasticity, h is the thickness of the film, and t is the thickness of the oxide at the surface of the film. In this core-shell model softening arises from two effects (1) from the difference in the Young's modulus of the oxide shell, and (2) from surface elasticity. While this model does not include a finite width (i.e. the forgoing model is strictly valid for films only), we use the model as a first approximation of the softening in the nanoribbons. As

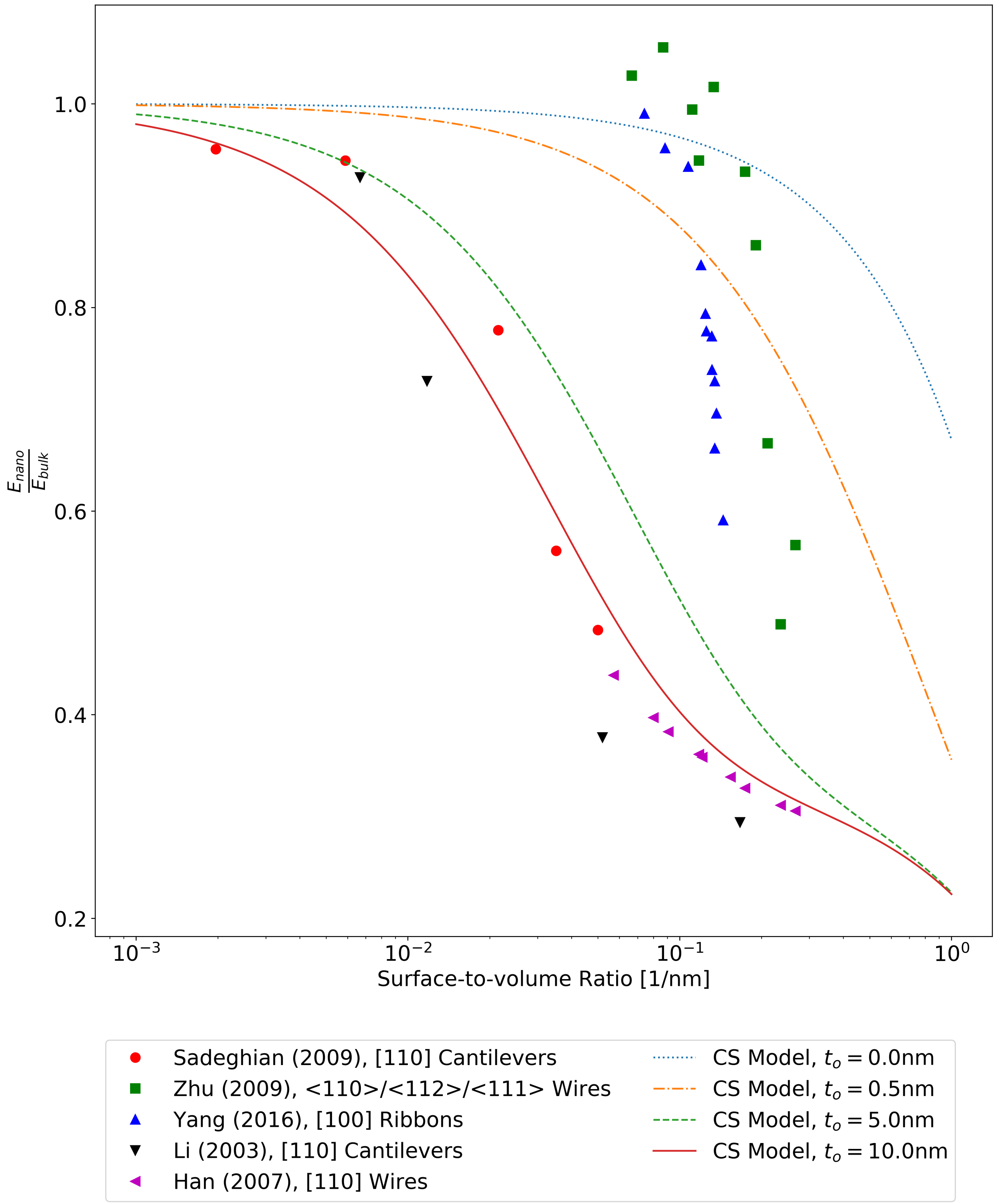

Figure 4.6: Reduction in Young's modulus from bulk from measured wires [3, 8, 15, 19, 20], and from the core-shell model (equation 4.4) with various oxide thicknesses, t_0

seen in Figure 4.6, this model provides a good fit for data from a number of experiments [8, 19, 20]. Depending on the parameters used—the Young's moduli of the shell (E_{shell}) and the core (E_{core}), shell thickness, and characteristic length h_0—this model is able to capture the onset size of softening for both clusters of data, though it only fits the first cluster well.

Additionally, this model is explicitly formulated for a film in bending, and was fitted to data measured for cantilevers, however the effect of the surface oxide on the tensile modulus can be different from that of the bending modulus. To look at the change in the speed of sound, the tensile modulus seems to be more appropriate. Following the approach by Sadeghian [8, 13] we derive an expression for ribbons in tension. The approach accounts for the effect of the native oxide on the effective elastic modulus with a composite model, so in tension

$$E_{\text{eff}} = E_{\text{shell}} \frac{A_c}{A_t} + E_{shell} \frac{A_t - A_c}{A_t}, \tag{4.5}$$

where A_c and A_t are the cross sectional areas of the core and the total ribbon respectively. The surface elasticity is then modeled by extending the expressions from Miller and Shenoy [5] to handle ribbons of non-square aspect ratio as

$$\frac{E - E_{\text{bulk}}}{E_{\text{bulk}}} = \alpha \frac{S}{E_{\text{bulk}}} \frac{1}{h} = \frac{2(w+h)}{w} \frac{h_0}{h}, \tag{4.6}$$

where w and h are the width and the height of the ribbon. Combining Equations 4.5 and 4.6 results in

$$\frac{E_{\text{ribbon}}}{E_{\text{core}}} = \left[1 + \frac{2(w+h)}{w} \frac{h_0}{h}\right] \left(\frac{A_c}{A_t} + \frac{E_{\text{shell}}}{E_{\text{core}}} \frac{A_t - A_c}{A_t} \right). \tag{4.7}$$

As the parameters $t_{ox} = 5\,\text{nm}$, $h_0 = -0.1099\,\text{nm}$, $E_{\text{shell}} = 60\,\text{GPa}$, and $E_{\text{core}} = 180\,\text{GPa}$ provide a reasonable fit to the experimental data using equation 4.4, especially the data from references [8, 19, 20], we will use these parameters with the model for tensile softening to approximate the acoustic softening effect.

Adding softening to the MCRT calculations reduces the thermal conductivity. Figure 4.7 shows this reduction along with the results from experiment and from MD. For the MCRT the softening is approximated using equation 4.4 for a film with the S/V ratio as the nanoribbon whose thermal conductivity we wish to predict with MCRT. Plotting the percent difference between the MCRT and measured thermal conductivity (Figure 4.7B) we see that this softening reduces the over-prediction of the MCRT, compared to the fully diffuse case. There is still some over-prediction when compared with the very smallest nanoribbons reported by Yang, although, as seen in Figure 4.7A, the absolute difference in thermal conductivity is small. Without the addition of any specularity, the MCRT model with softening now underpredicts the thermal conductivity for Yang's thick ribbons, as well as the large structures prepared by Park. In the size range of our MD simulations, the MCRT with softening seems to strongly underpredict the thermal conductivity seen in MD at 300 K with both smooth and roughened surfaces. This is likely because (a) our MD models do not have a surface oxide (which for the MCRT is set at 5 nm), and (b) the studies of softening in MD consistently show less reduction in the Young's modulus than that observed experimentally as the MD models lack many features that contribute to acoustic softening, such as surface oxides and pin-hole defects (see for example [13]).

4.1.4 Combined Effects

As the addition of neither acoustic softening nor specularity alone allows the MCRT to match the thermal conductivity across the whole range of experimental data, with both diffuse and specular MCRT overpredicting thermal conductivity in small structures, and with diffuse MCRT with softening underpredicting thermal conductivity in large structures, we seek to combine the two effects. This combination of effects can be understood as the application of multiple reduction ratios, here F_{soft} (the reduction from softening) and $\tilde{F}_{\text{surf}}$ (the reduction from surface scattering). Using these reduction ratios, we can now write the total reduction in the thermal conductivity as $\kappa_{reduced} = F_{\text{soft}}\tilde{F}_{\text{surf}}\kappa_{\text{bulk}}$. Note that $\tilde{F}_{\text{surf}}$ is calculated in this analysis as $\kappa_{\text{MCRT}}/\kappa_{\text{bulk}}$ for an unsoftened system rather than directly from the MCRT simulations.

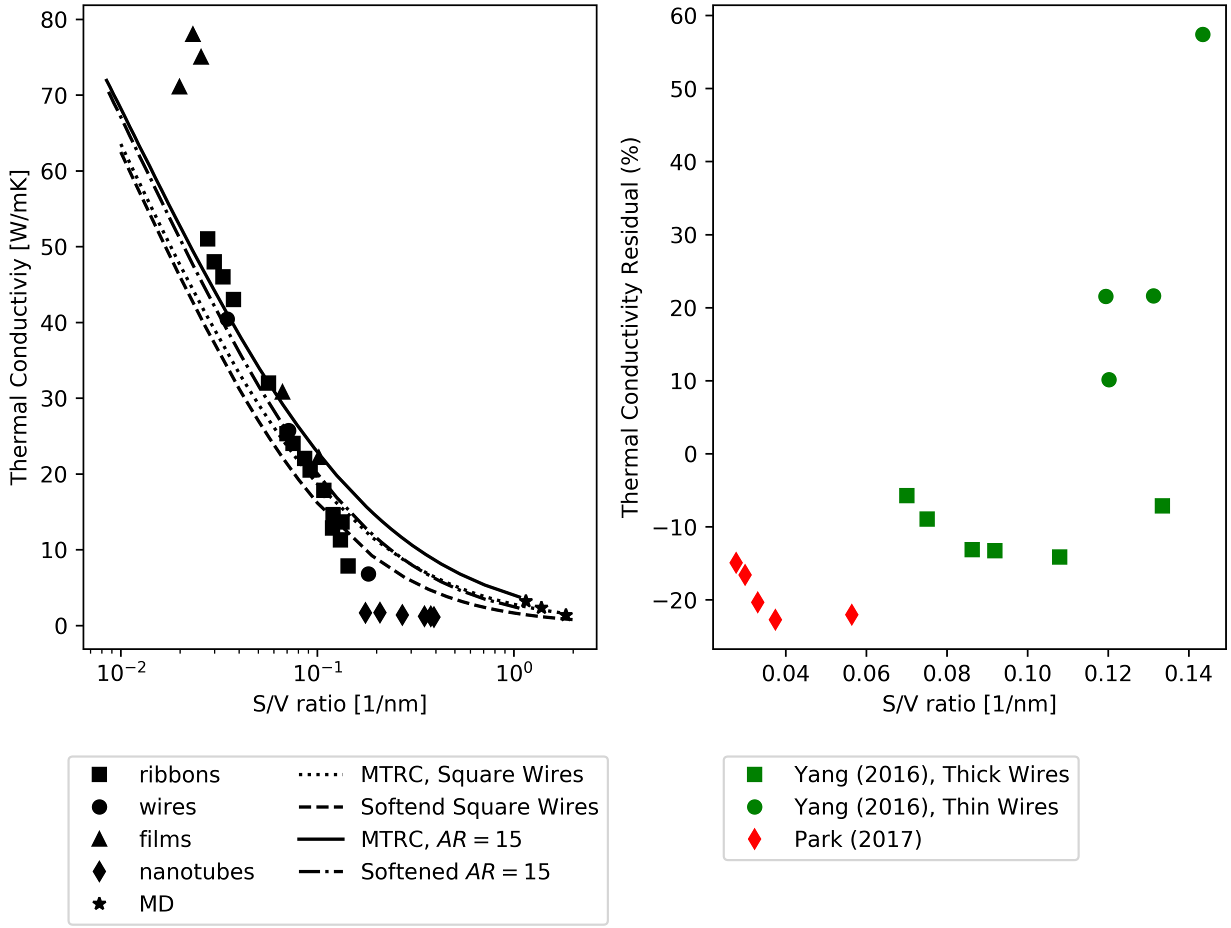

Figure 4.7: (A) Experimental conductivities from Figure 4.1 and diffuse MCRT with and without softening from eq. 4.7. (B) The percent increase in the thermal conductivity from MCRT with softening over the measured measured value for the nanoribbons.

Plotting the reduction ratios in Figure 4.8 gives a good indication of the relative strength of surface scattering effects and acoustic softening at various S/V ratios. Across all sizes, F_{soft} is much larger than $\tilde{F}_{\text{surf}}$ for either specular or diffuse surfaces, and thus softening is responsible for much less of the total reduction in thermal conductivity. F_{soft} ranges from approximately 0.5 (a 50% reduction) for the smallest systems (large S/V ratios) to nearly 1 (no reduction) for systems on the order of 100 nm. While, $\tilde{F}_{\text{surf}}$ ranges from just above zero (a very strong reduction) to approximately 0.4 (a 60% reduction). The combination of both surface scattering and acoustic softening is also plotted in Figure 4.8 as $F_{\text{total}} = F_{\text{soft}}\tilde{F}_{\text{surf}}$ for both diffuse and specular surfaces. In both cases, the total reduction is now lower across all the S/V ratios than just with the MCRT. Additionally, comparing the reduction ratio with both specularity and softening to just the reduction ratio from diffuse surface scattering, at small S/V ratios (large structures), the reduction ratio is higher than $\tilde{F}_{\text{surf}}$ for the diffuse case, while for large S/V ratios, the reduction ratio is smaller than $\tilde{F}_{\text{surf}}$ for the diffuse case. This can be seen more clearly in Figure 4.9, where the reduction ratios are plotted on a log axis.

The cumulative effect of both surface scattering with $p = 0.05$ and acoustic softening on thermal conductivity is shown in Figure 4.10. We see that for the thick wires from Yang [3], the addition of specularity and of acoustic softening to the MCRT model roughly balance each other out. For the thin ribbons the thermal conductivity is more closely matched with acoustic softening than without, however with a 5% specularity ($p = 0.05$) the MCRT still overpredicts the thermal conductivity. As with larger ribbons, the amount of specularity is a property of the surface of the structures, and thus may differ between devices, and may explain some of the overprediction in the MCRT with both specularity and acoustic softening (i.e. the thin wires might have a more diffuse surfaces).

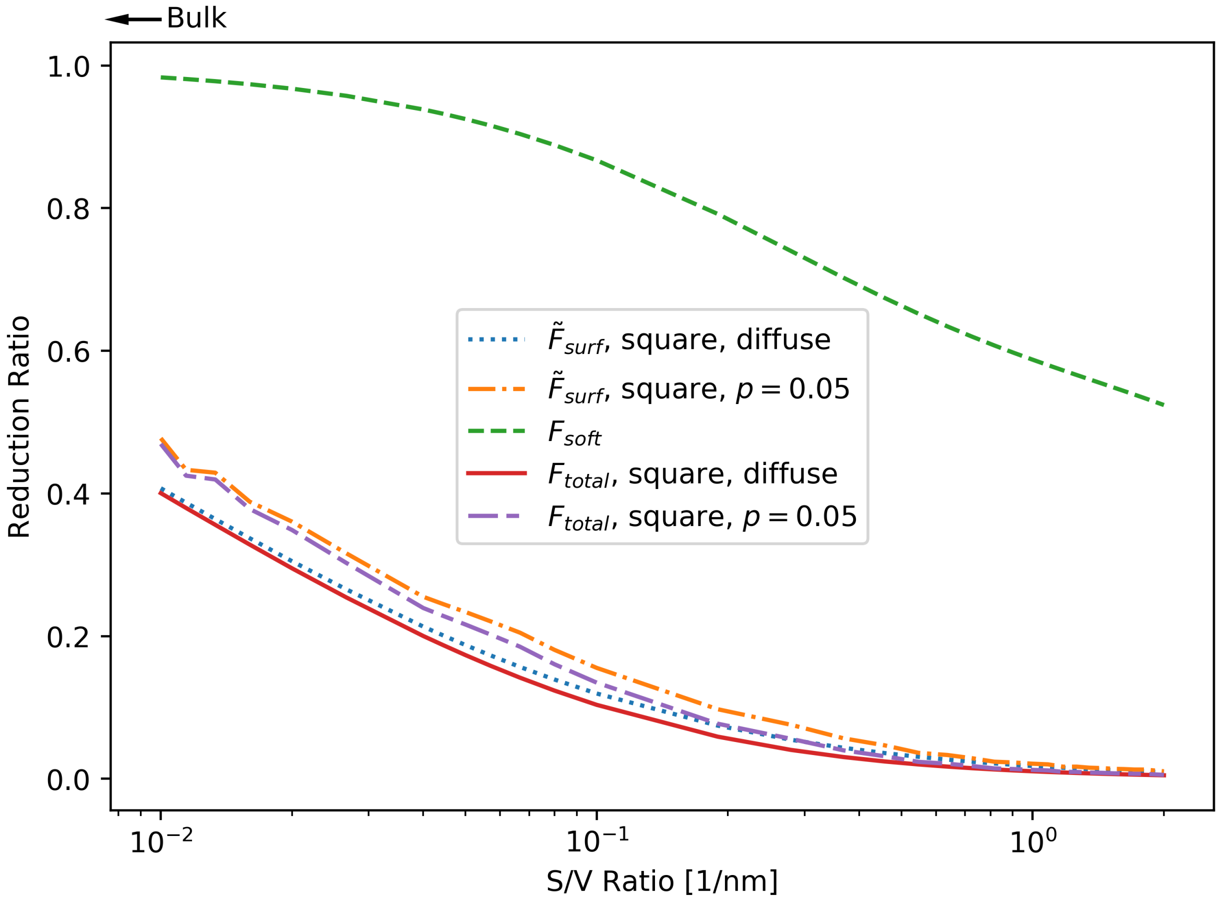

Figure 4.8: Reduction ratios for both acoustic softening and surface scattering.

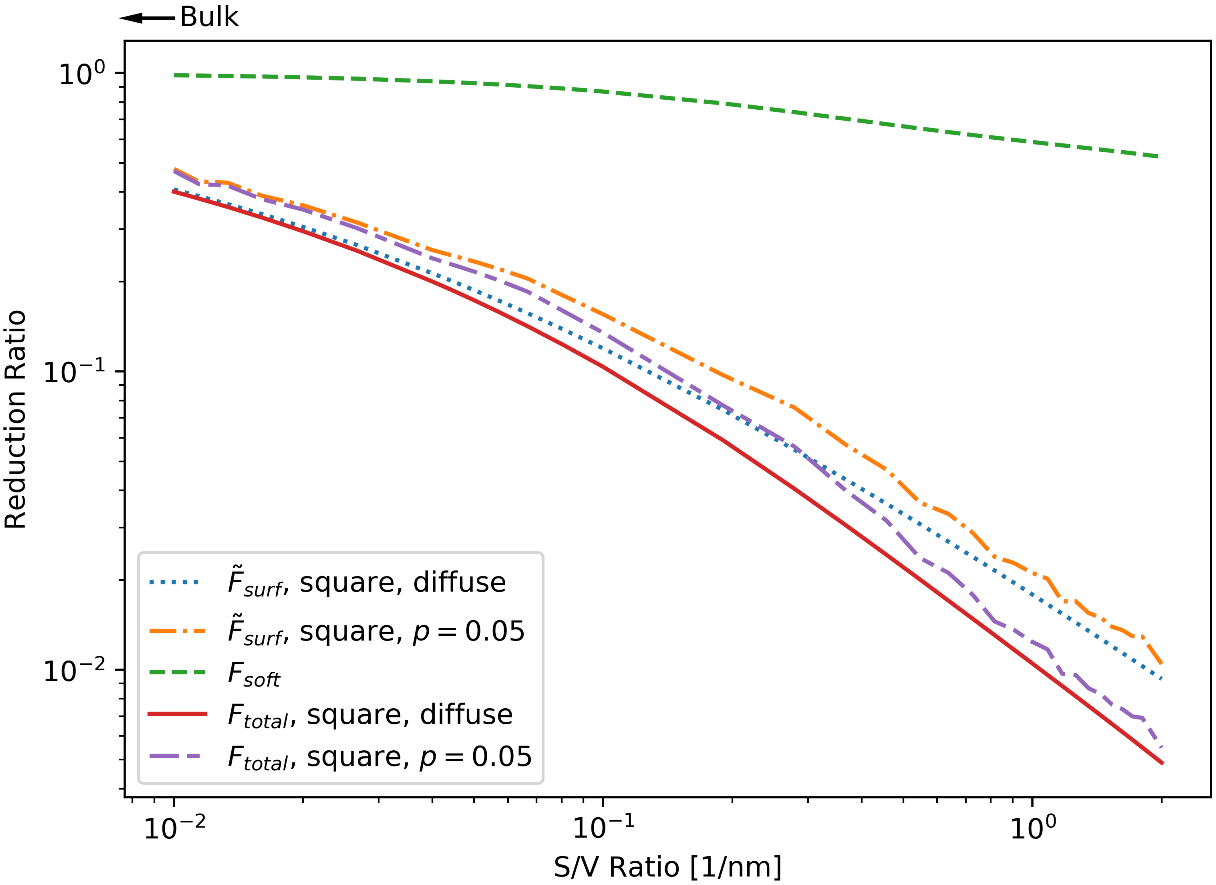

Figure 4.9: Reduction ratios from Figure 4.8 plotted on a log scale.

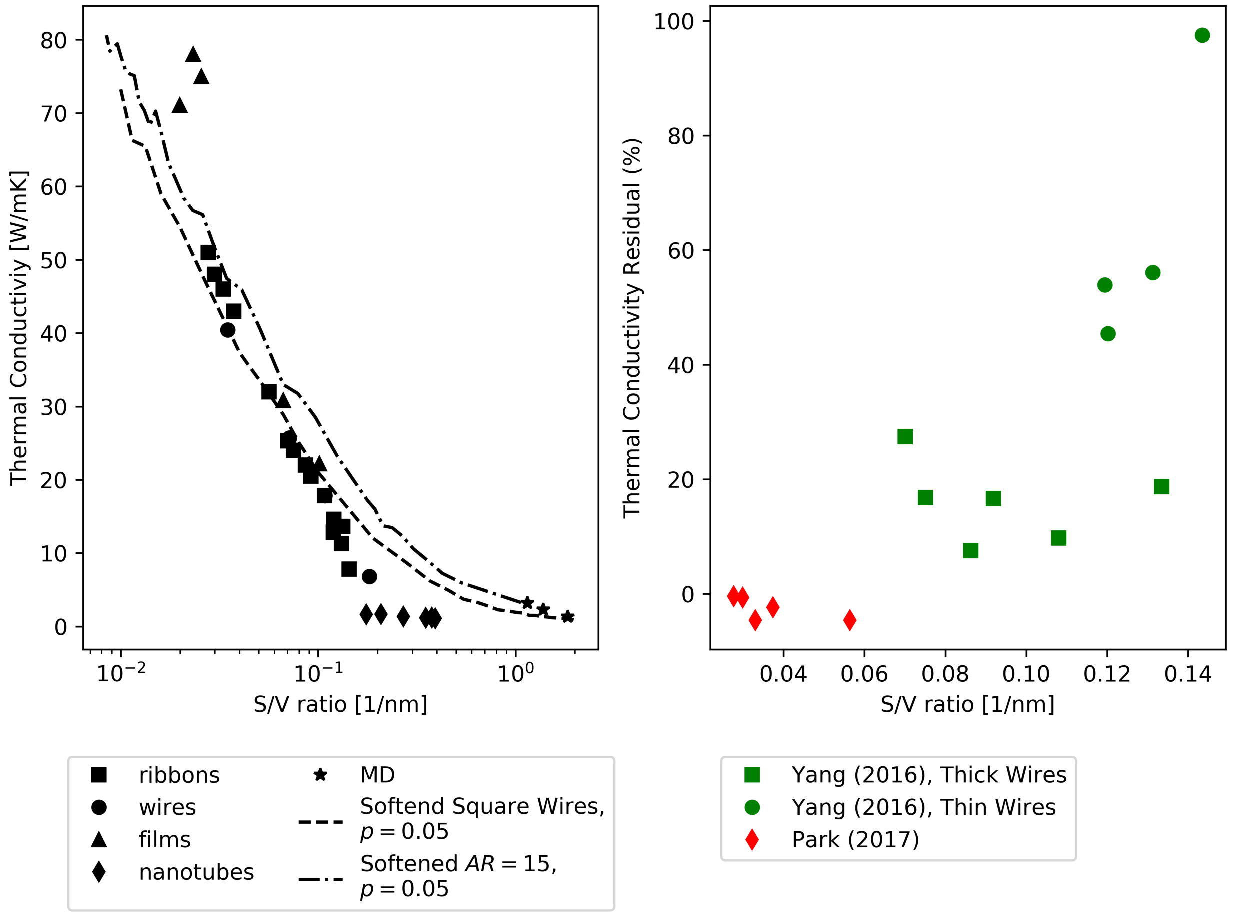

Figure 4.10: (a) Thermal conductivity from MCRT with both specularity of $p = 0.05$ and acoustic softening, compared with values from experiment. (b) Difference between experiment and the MCRT with both specularity of $p = 0.05$ and acoustic softening

4.1.5 Modeling Other Factors

The simplest effect from acoustic softening or acoustic stiffening is the effect on the group velocity, and the most frequent applications of softening to explain reduced thermal conductivity have only considered the group velocity effects. However, alterations to the elastic modulus imply changes to the phonon frequencies. As discussed in Chapter 2, the change in the dispersion relation causes effects in the group velocity, the heat capacity, and the mean free path–the three main factors of thermal conductivity. While each of these factors contains interesting deviations from bulk and bulk-like values when acoustic softening is included, in order to see how acoustic softening should manifest in experimental measurements, we must combine these factors to calculate thermal conductivity.

Using as our example case a nanowire with a diameter of 20 nm and a softening factor of 0.44 (from equation 2.9), we compute the spectral thermal conductivity. This example wire is of a similar scale to the first wires where anomalously low thermal conductivity was reported[36]. When we include the effects of softening on the heat capacity, phonon group velocity, and mean free path, we see that spectral thermal conductivity varies around the velocity-only value, instead of undergoing a flat reduction as seen for reducing the group velocity alone (Figure 4.11).

While the contribution to thermal conductivity from longer wavelengths where the difference in the softening models exists, is small, the overall change in the thermal conductivity between the two softening models is appreciable. For the model neglecting the effect of softening on the MFP and heat capacity, the thermal conductivity at this size scale is approximately 1.7% lower than the full softening model (4.76 W/m K vs 4.84 W/m K).

In addition to spectral thermal conductivity at room temperature, we can look at the temperature dependence of thermal conductivity under our softened model. In Figure 4.12 we compare the softened and unsoftened thermal conductivity from the BvKS dispersion for 20 nm to 40 nm characteristic sizes with softening factors from equation 2.9. First, the change in the thermal conductivity is not uniform. While at higher temperatures, the ther-

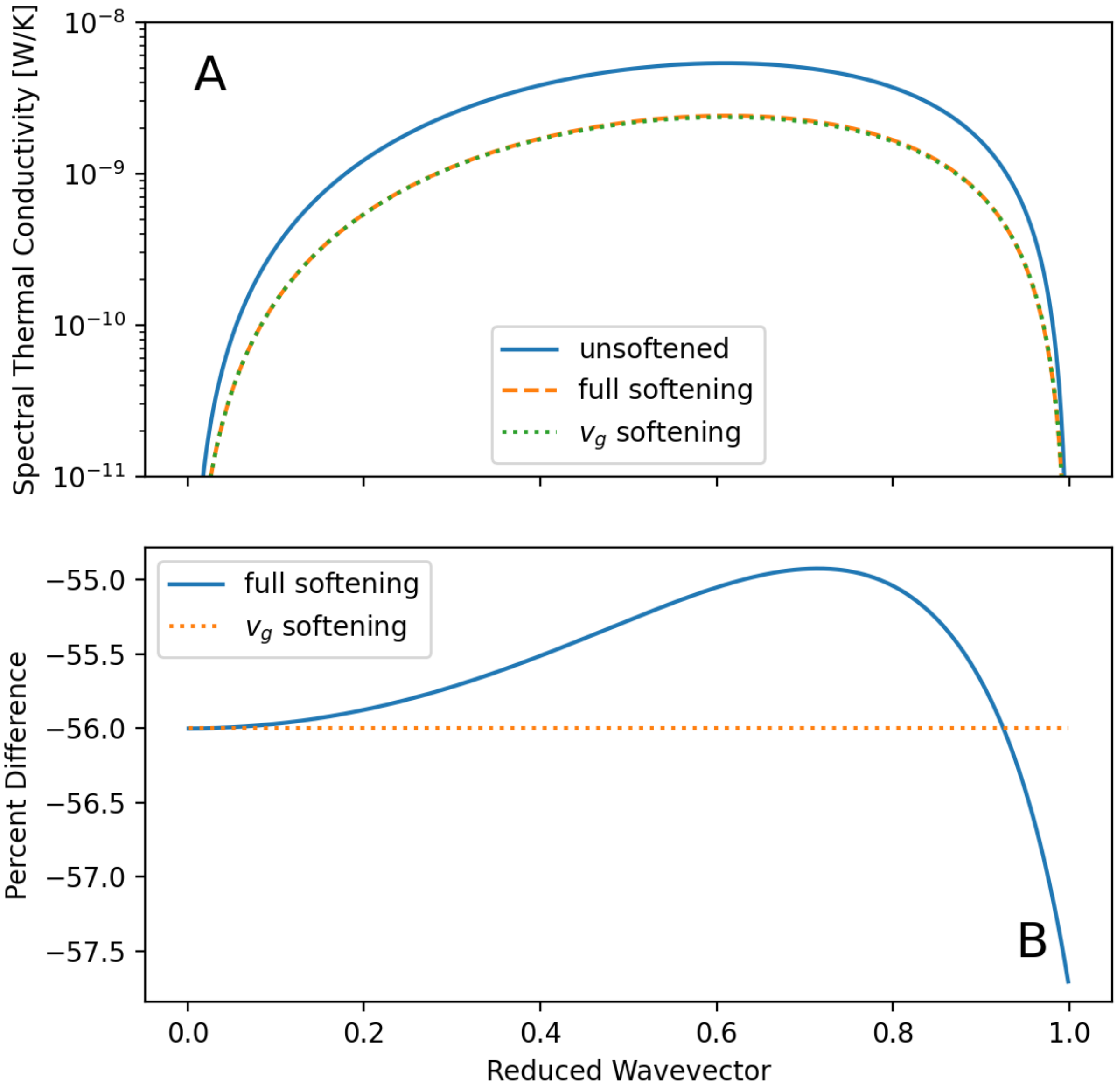

Figure 4.11: A: spectral thermal conductivity as a function of reduced wave vector (i.e. thermal conductivity per inverse wave vector [W/(mK)/(1/m)]) for nanostructure with a characteristic size of 20 nm for unsoftened, v_g only softening, and softening including group velocity, MFP and heat capacity ($F_s = 0.44$). B: percent difference between the unsoftened and softened models.

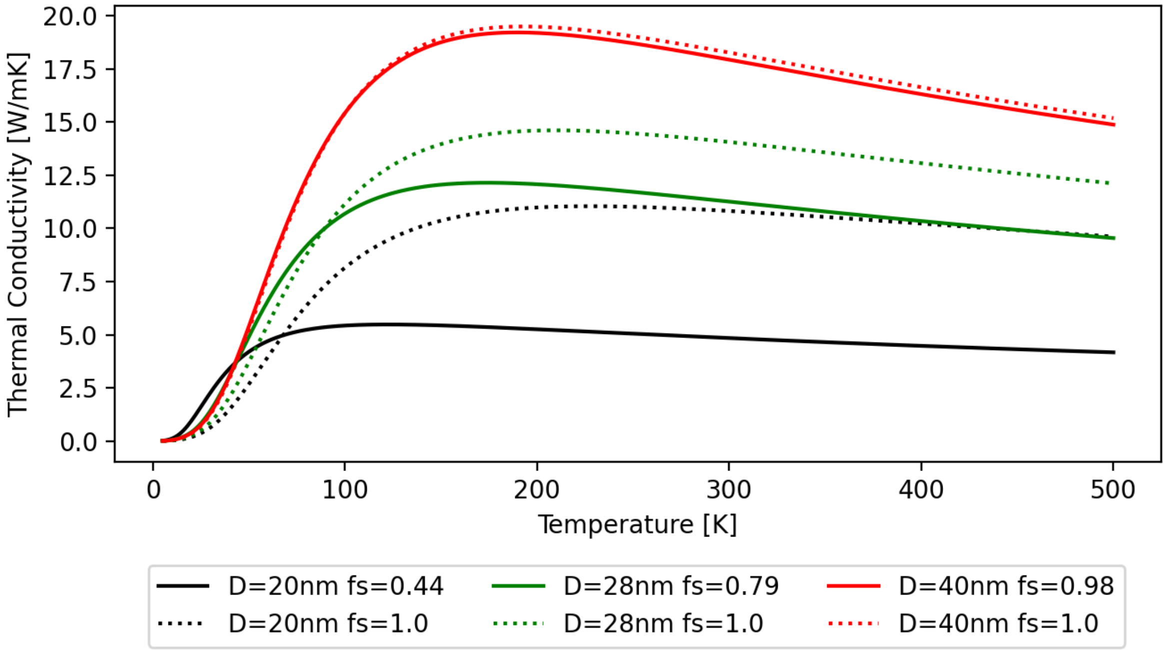

Figure 4.12: Thermal conductivity as a function of temperature for Si structures of various characteristic sizes with and without softening.

mal conductivity is reduced due to the softening, the low-temperature thermal conductivity (below about 75 K) is increased. Additionally, the temperature at which the peak thermal conductivity occurs is reduced. If softening were only affecting the group velocity of phonons, we would not expect to see these features, but rather a uniform shift of the thermal conductivity downwards with temperature.

To further explore the origins of the changes in the temperature dependency of the thermal conductivity, we consider the effects of each term in the kinetic theory independently. In Figure 4.13 we see that reducing the group velocity with a softening factor results in a uniform reduction across temperature. The other two factors in the thermal conductivity have significantly more variation over temperature. For the softening of the MFP, the effect on the thermal conductivity is to reduce the thermal conductivity slightly at higher temperatures, while little effect is seen at low temperatures. For the heat capacity factor, the thermal conductivity is increased by softening across all of the temperatures, but with the increase being more dominant at lower temperatures, and nearly disappearing by room temperature.

4.1.6 Comparison to Experiment

To compare the results of our model with experiment, we focus on the results obtained by Yang et al. [3]. Here thermal conductivity and elastic modulus are measured for two groups of nanoribbons with different thicknesses (a thick group between $30 - 32\,\text{nm}$ thick, and a thin group between $18 - 20\,\text{nm}$ thick). In each group, the width was varied, which varies the surface-to-volume ratio of the wire.

We have attempted to bracket the observed thermal conductivities with our MCRT model including a softening factor, F_s. In Figure 4.14 thermal conductivities for wires with 20 nm and 30 nm thicknesses calculated with an MCRT model with softening factors of 1.0 (unsoftened) and 0.44 (corresponding to a 20 nm diameter wire) are plotted with the experimental data. From this, we are able to model the thermal conductivity of the thick wires very well with an unsoftened MCRT model. However, the unsoftened MCRT model predicts significantly higher thermal conductivity for the thin group of wires than observed.

For the thin group we are able to bracket the data with our softened model using $F_s = 0.55$. This softening corresponds to a ratio of $E_{\text{nano}}/E_{\text{bulk}}$ of around 0.30 which is consistent with the maximum softening experimentally observed[19, 20] and for a structure with a hydraulic diameter of approximately 22 nm using the data from Yang et al.[3]. With this level of softening, we see that all of the ribbons in the thin group are bracketed by the MCRT.

Using F_s estimated from equation 2.9, MCRT simulations for both thick and thin ribbons are shown in Figure 4.15. As the experimental ribbons have a thin oxide layer (approximately 2 nm thick [3]) that should play little role in thermal conductivity and that is not modeled in the MCRT simulations, 4 nm is removed from both the width and height of the ribbon when calculating the MFP with MCRT. With this model, we observe a close correspondence

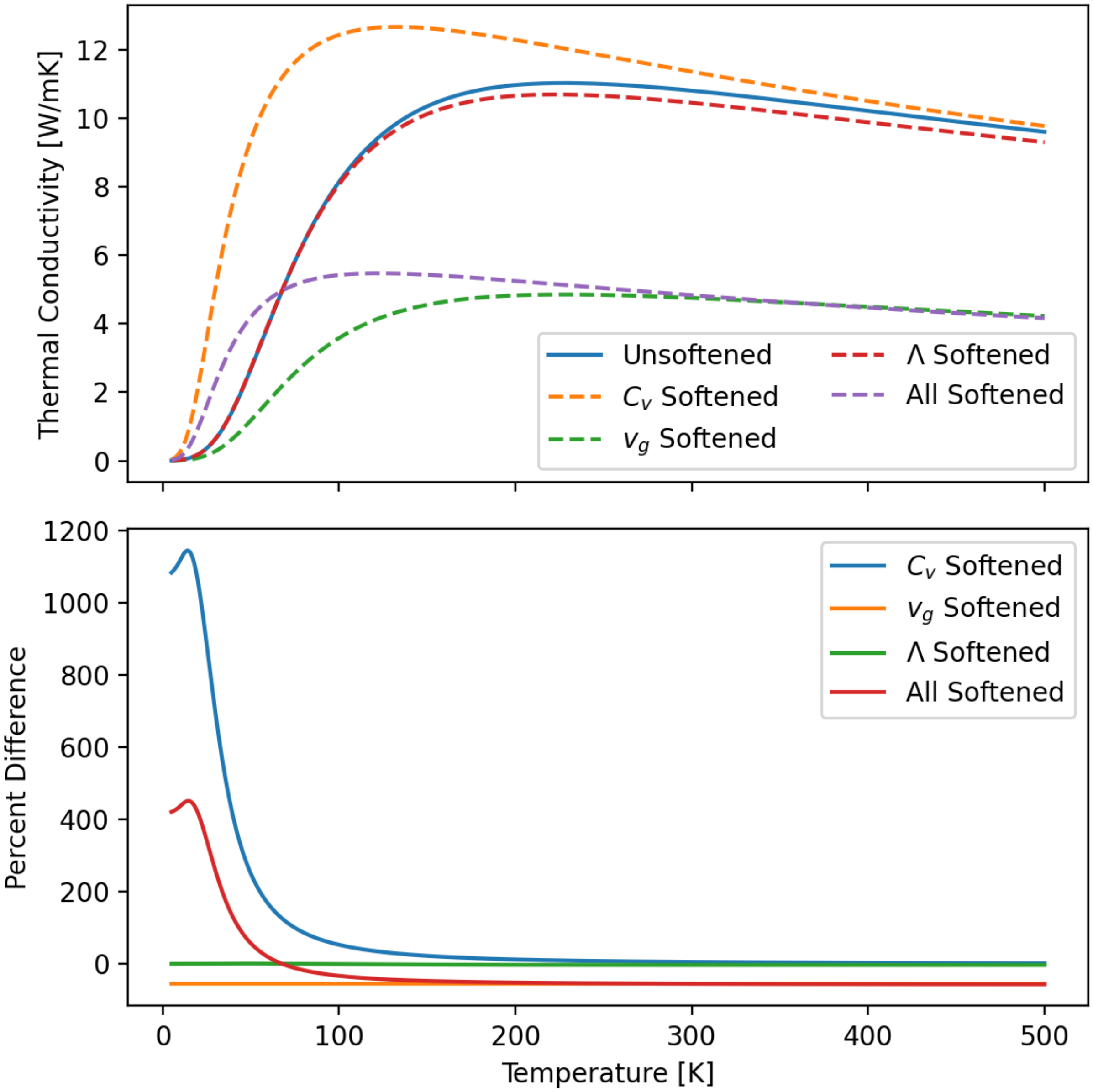

Figure 4.13: Thermal conductivity as a function of temperature for a structure with a characteristic size of 20 nm ($F_s = 0.44$) with thermal conductivity from the components of the softening model plotted separately

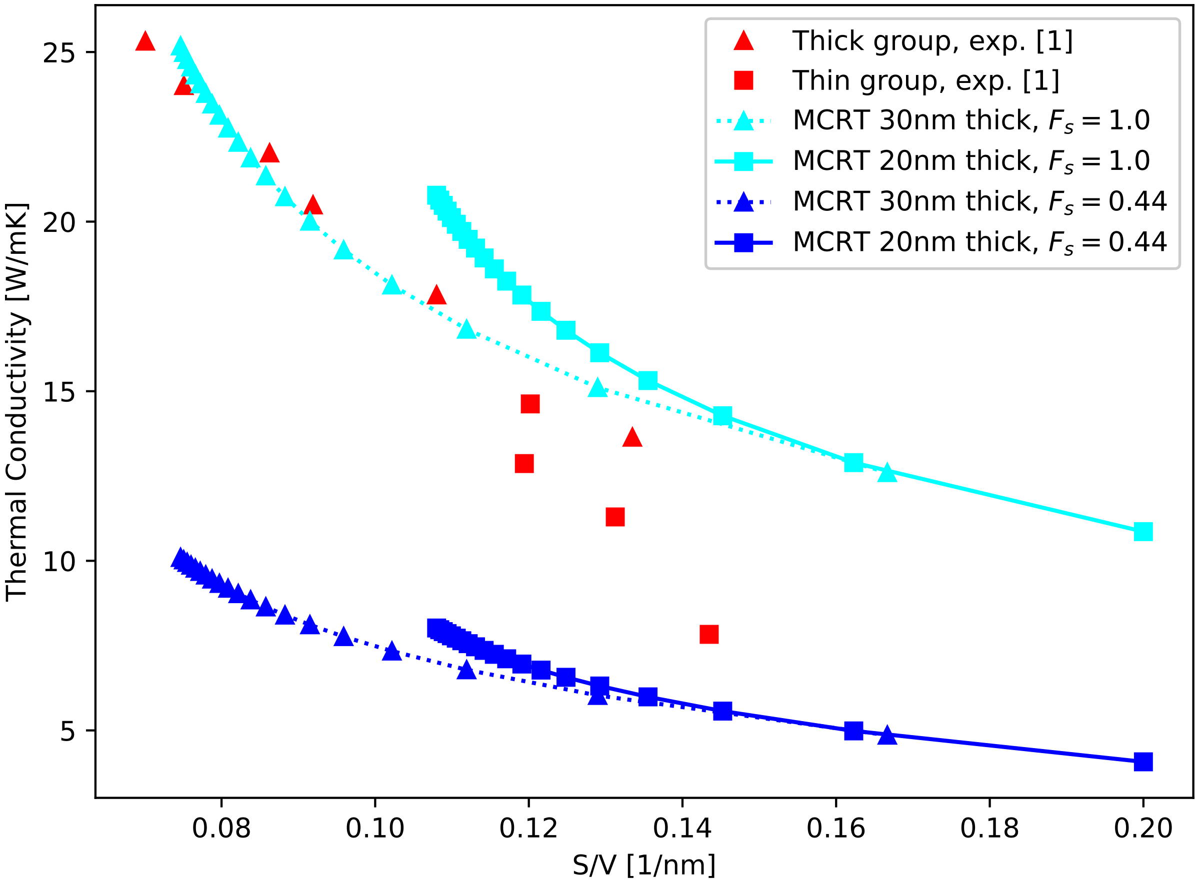

Figure 4.14: Comparison of size sweeps of our thermal conductivity model with and without softening at 300 K to the thermal conductivity reported by Yang et al. [3] for nanoribbons at 300 K.

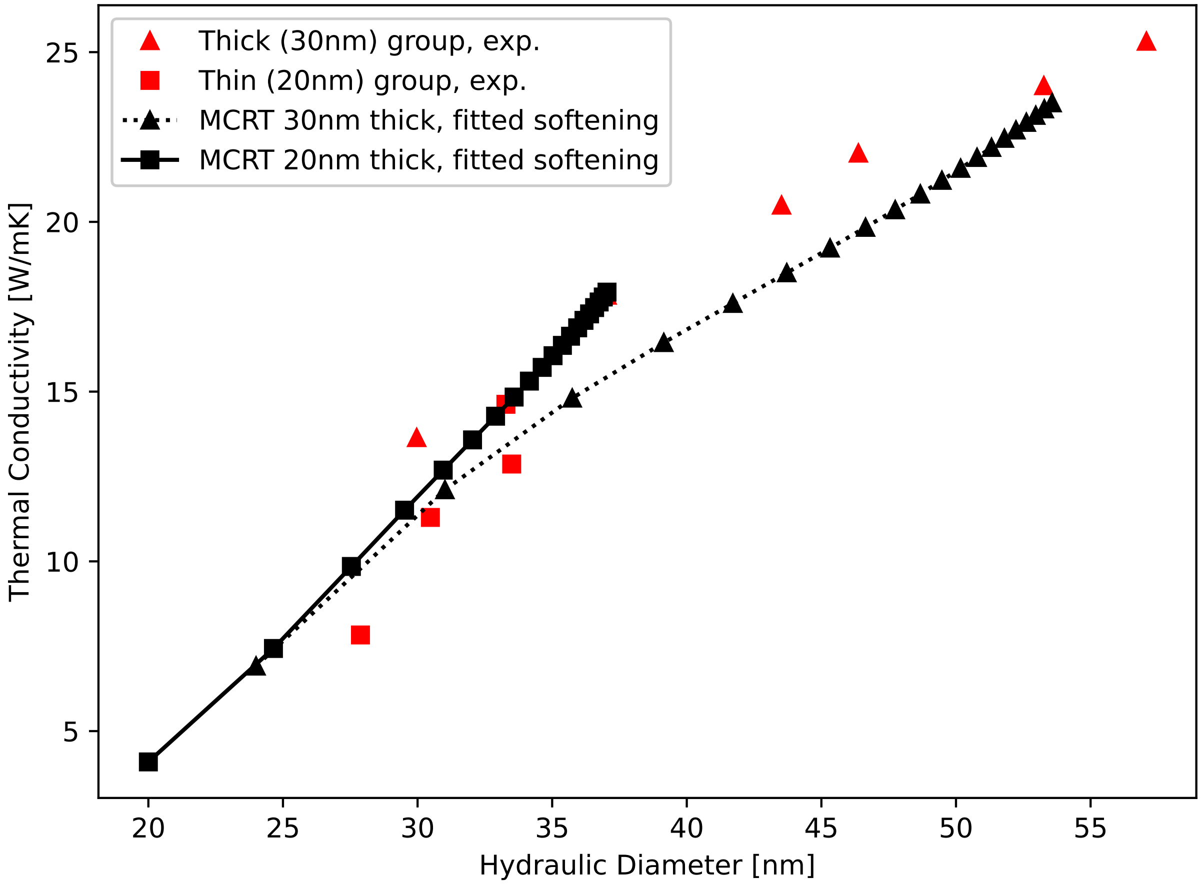

Figure 4.15: Comparison of size sweeps using our thermal conductivity model with F_s given by equation 2.9 at 300 K with the thermal conductivity reported by Yang et al. [3] for nanoribbons at 300 K. For the ribbons from Yang et al. 2 nm of oxide is discounted in the calculation of the hydraulic diameter.

between the model and the experimental values.

While this model indicates that acoustic softening can explain the lower thermal conductivity for the thin group of wires, it doesn't explain fully the transition from unsoftened to softened that occurs with a move from the thick to thin ribbons. Some of the apparent sharpness may be geometric in nature, with the different thicknesses trending together for very small structures (high S/V), where the scattering is most strongly controlled by the width, but differing in the S/V regime where both thickness and width become important. Thus, the placement of the 1/(S/V) type curve for the thermal conductivities predicted is shifted to lower S/V ratios for thicker wires and to higher S/V ratios for larger wires.

Another factor affecting the apparent suddenness of the transition is the high degree of sensitivity of acoustic softening phenomena to such influences as surface recombinations [10], the relative size of oxide layers [13, 16, 17], and etching defects [13, 14]. Computational work by Shim et al. has shown that the surface recombination of various silicon surfaces has a strong impact both on the magnitude of softening and the direction, indicating that for some recombinations a nanoscale stiffening can occur [10].

While comparison to our model for the effect of acoustic softening on thermal conductivity with the size-dependent data gives us some confidence that our method produces results that match the general trends seen in experiment, it does not fully disentangle if softening effects in heat capacity and scattering are observed in the experimental data. However, because of the difference in the effects of softening at low and high temperatures, we examine the temperature-dependent thermal conductivity reported by Yang et al.[3].

In Figure 4.16 we show thermal conductivity from MCRT for wires of the same sizes as Yang et al., with F_s from equation 2.9. Again, when computing the MFP, the dimensions of the nanoribbons were reduced by 4 nm to account for the approximately 2 nm thick oxide commonly present in experiment. We calculate thermal conductivity using both a softened and unsoftened model, and compare them to the data reported by Yang et al. [3]. Importantly, including heat capacity and MFP effects in the softening shifts the peak thermal conductivity to lower temperature. At lower temperatures, the thermal conductivity is increased, while at higher temperatures, the thermal conductivity is decreased. This is similar to the effect seen for Ge-Si core-shell wires [38].

When compared with the values reported by Yang et al. for the temperature-dependent thermal conductivity in thin wires, a few features are notable. First, there is a flatter dependence on temperature after the peak thermal conductivity in the reported values than for the softening model. In the reported values Umklapp scattering begins to have a noticeable effect (i.e. thermal conductivity stops increasing rapidly) around 125 K to 150 K. This is in contrast to a model including contributions from softened heat capacity and mean free paths

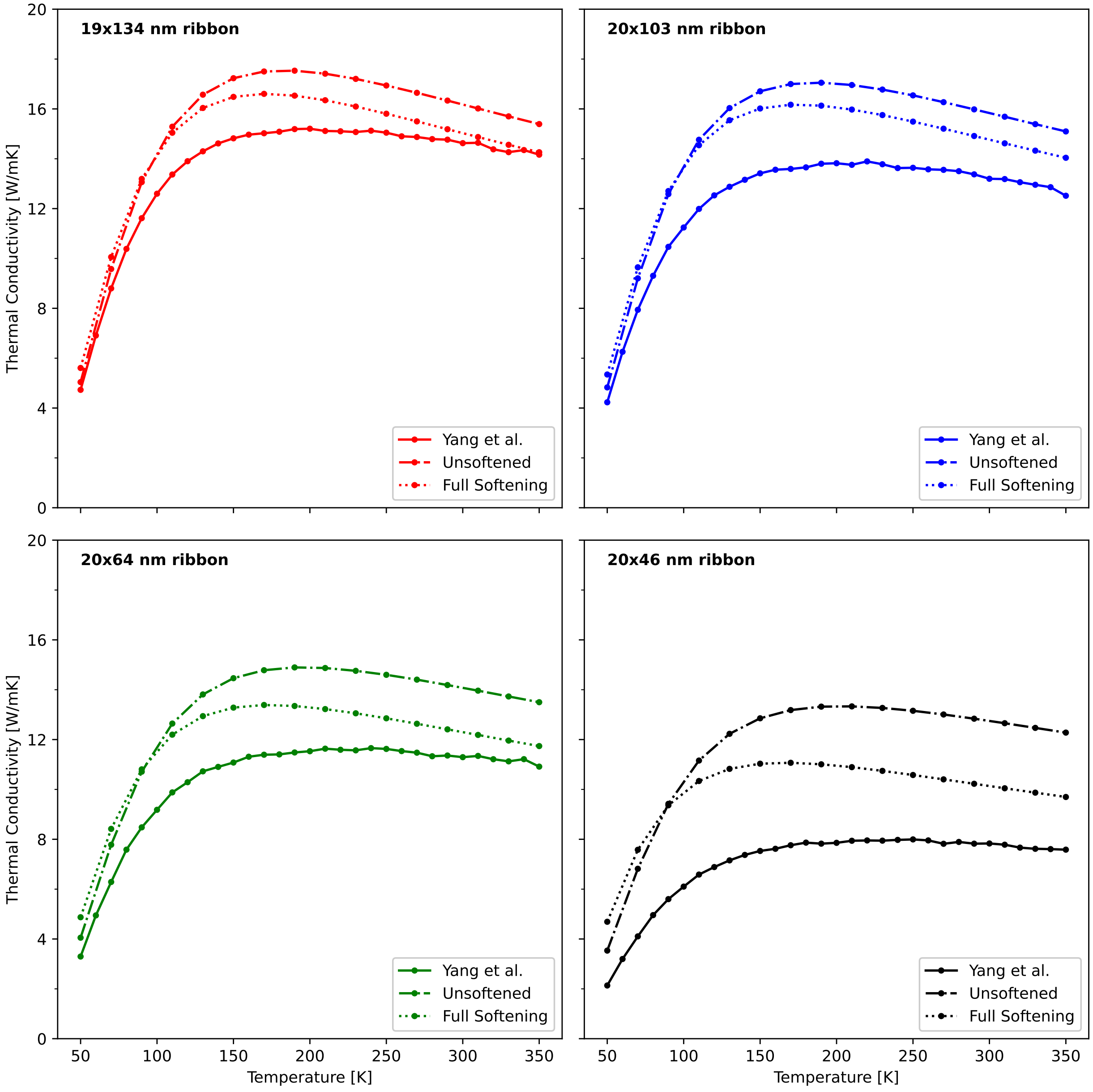

Figure 4.16: Calculated thermal conductivity for wires with sizes matched to those reported by Yang et al. [3] without softening, with softening from equation 2.9.

where Umklapp scattering begins to dominate around $75\,\mathrm{K} - 100\,\mathrm{K}$.

We attribute the discrepancies between the models and experiment to the highly approximate nature of the dispersion relationship used and the softening method. Namely the fitting parameters for phonon-phonon scattering and for impurity scattering are taken from bulk silicon and vary for the nanostructures considered due to the processing. The lack of normal scattering in the model may additionally reduce the accuracy of the model at low temperatures. Additionally, the model for F_s used here is based on Young's modulus measurements, is entirely empirical, and may not completely capture the pertinent physics related to transport properties. Moreover, in contrast to our assumption that the softening is uniform across the cross section of the nanostructures we consider, effects of the surface energy are likely to be strongest at the surface of the wire and decay towards the center of the wire. Therefore, the approximation of a uniform distribution of strain energy should be examined. Finally, the effects of the surfaces on dispersion relation of the wires may not be the same for both the transverse modes and the longitudinal modes; the effects of oxide layers on the effective elastic modulus are not the same for extension and bending.

4.2 ZnO Nanowires

Overall, there is a modest effect from acoustic stiffening that increases the thermal conductivity at most temperatures. At low temperatures, thermal conductivity is slightly reduced compared to the unstiffened case mostly due to the impact of the heat capacity. At higher temperatures, the thermal conductivity is increased, though this increase does not reach the magnitude expected from considering velocity scaling only. The modest deviation is the result of a number of competing factors, and a calculation of all the combined effects results in the thermal conductivity not reaching the value expected when considering the geometry and velocity alone.

4.2.1 BvKS Model

In the ZnO nanowires, the main competition preventing the expected increase in thermal conductivity is that between the effects of velocity and the effects of scattering, which serve to counteract each other. In Figure 4.17 we plot the thermal conductivity as a function of temperature considering stiffening in particular factors only. Here we plot the effects on the mean free path rather than scattering as this preserves the insensitivity of reduction in thermal conductivity from boundary scattering to stiffening effects. As a brief explanation, consider the kinetic formulation where we can write thermal conductivity either in terms of the scattering rates τ or in terms of the mean free paths l.

$$k = \frac{1}{3}\int C_v v_g l dq = \frac{1}{3}\int C_v v_g^2 \tau dq \tag{4.8}$$

Here the mean free path and the scattering rate are related through the group velocity $l = v_g\tau$. For boundary scattering $\tau_{\text{boundary}} = D/v_g$ for a nanowire. Thus the mean free path resulting from the surface can be written as $l_{\text{boundary}} = D$, and is not affected by changes in the velocity from the stiffened dispersion relation.

In Figure 4.17, we see that the thermal conductivity including only a stiffened velocity experiences a significant increase across the entire range of the temperatures. Across the temperature range, the velocity is increased by a flat 15%, resulting in a corresponding 15% increase in the thermal conductivity. Without considering the impact of stiffening on the dispersion relation and the phonon frequencies, we would expect this effect to begin causing a noticeable increase in thermal conductivity over predictions using the bulk speed of sound for wires with diameters of less than 200 nm. Just considering velocity effects we would predict an increase in thermal conductivity would range from 3% for 70 nm wires to 15% for 10 nm wires when compared with prediction using only boundary scattering. Comparing the effect of various factors with changes in Figure 4.18, the qualitative effect of stiffing in each factor remains the same, although the effects are stronger relative to the thermal conductivity for

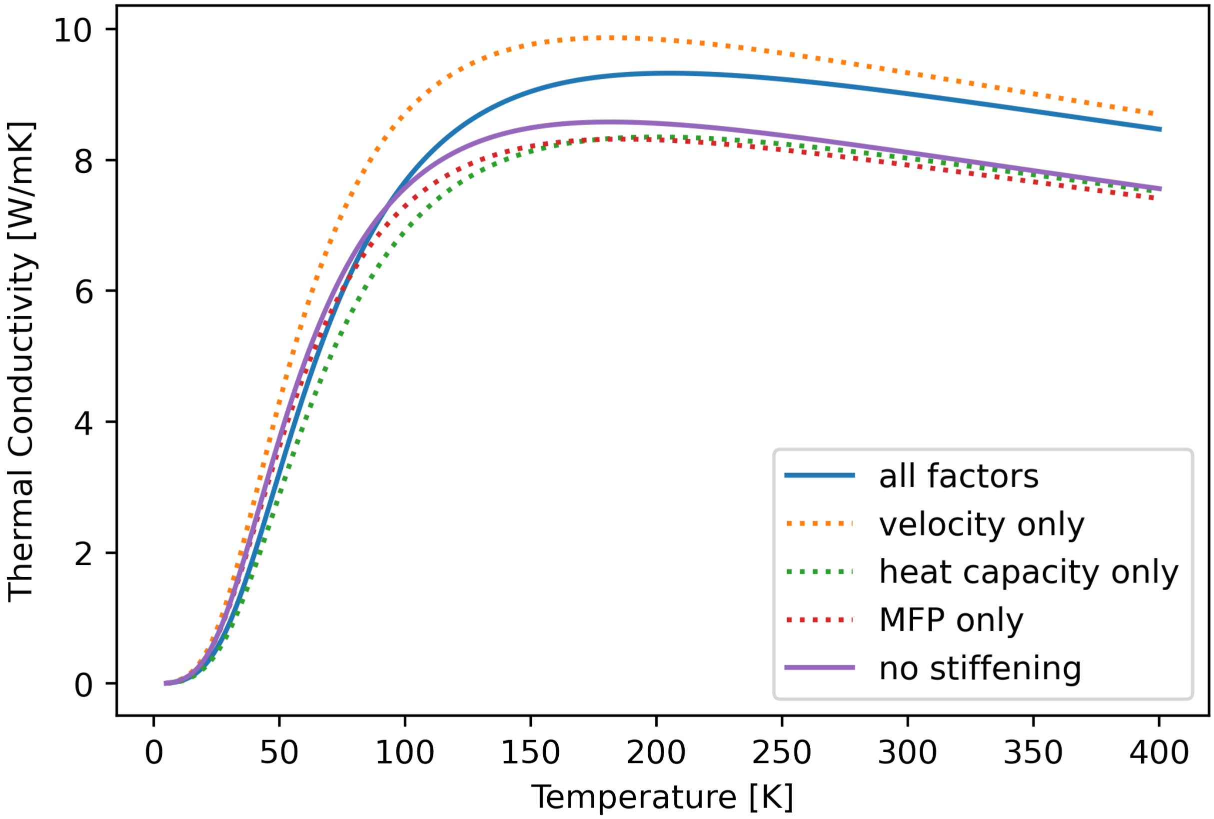

Figure 4.17: Thermal conductivity for a 10 nm ZnO nanowire with a stiffening factor $F_s = 1.15$ applied individually to heat capacity, mean free path, and scattering

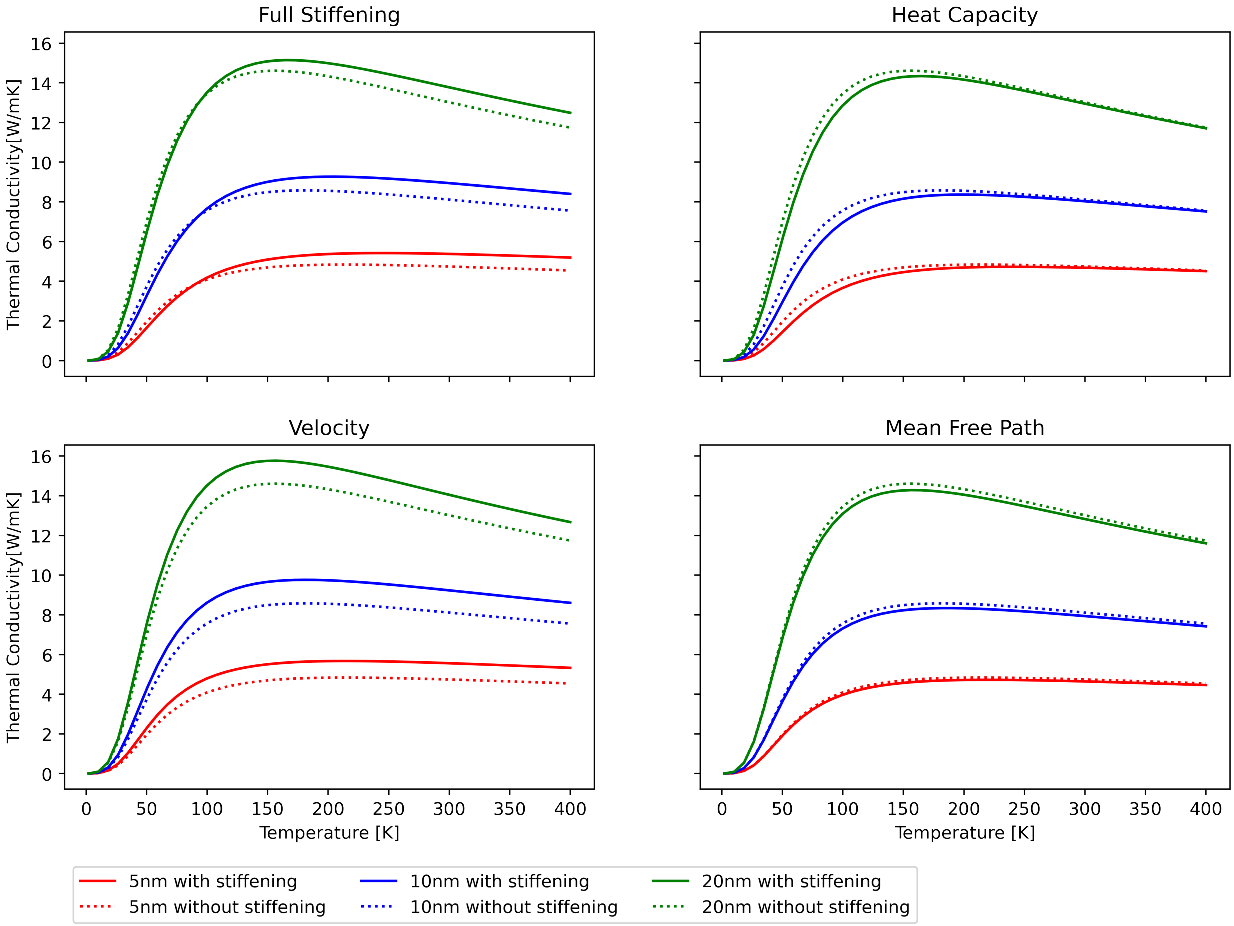

Figure 4.18: Thermal conductivity for various sizes of ZnO nanowires with size dependent stiffening factors from Eqs. 2.4 and 2.5 with fitted parameters applied individually to heat capacity, velocity, and mean free path

smaller sizes.

In contrast to the increase in thermal conductivity seen when considering the effect of stiffening velocity only, when considering the effect of stiffening on the scattering rate or the MFP, thermal conductivity is reduced at most temperatures. This can be seen in both Figure 4.17 and Figure 4.18. In particular, at 300 K, the reduction in thermal conductivity from the effect of stiffening on the MFP is on the order of 2% to 3% for the wires in Figure 4.18. When the effects of stiffening on velocity and scattering are considered together (Figure 4.19), the total effect is an increase in thermal conductivity across all temperatures.

Looking closer at how the scattering (and through it the MFP) is affected by stiffening, we

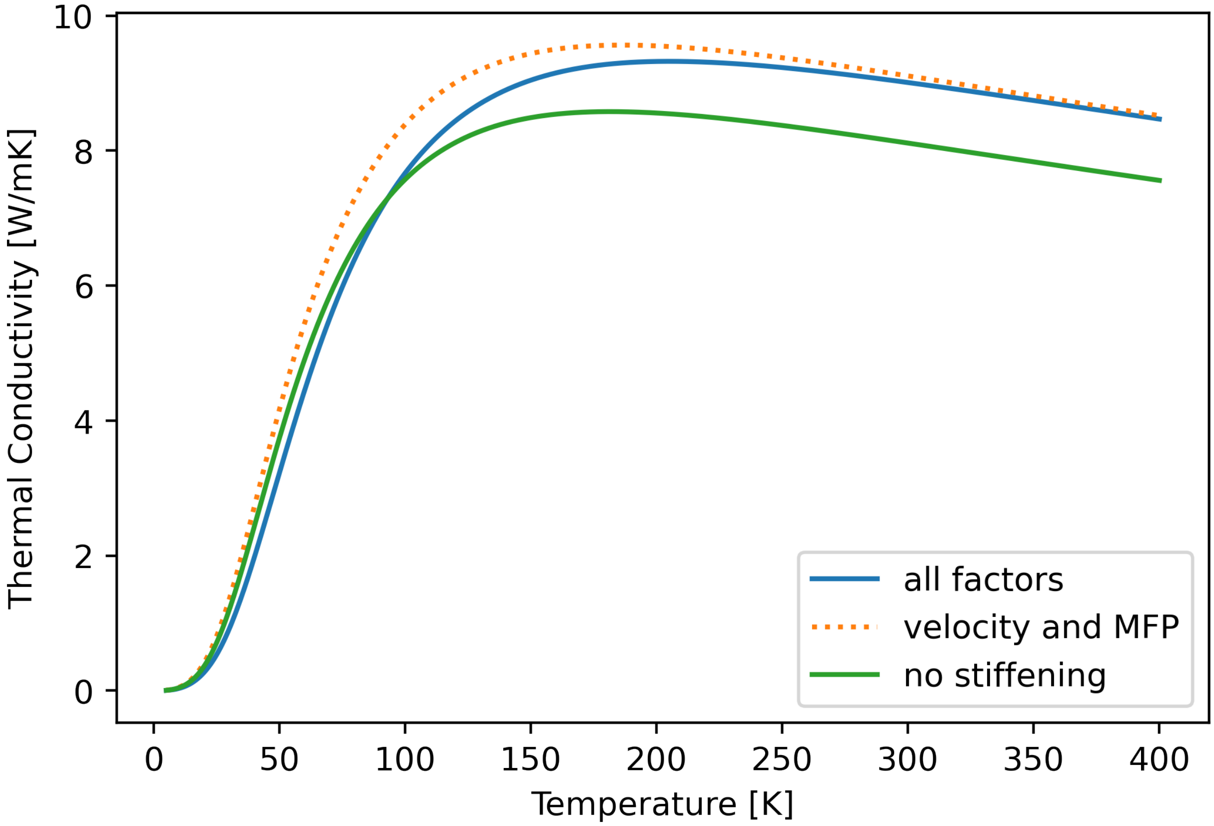

Figure 4.19: Effect of stiffening in both the MFP and the velocity on thermal conductivity for a 10 nm ZnO wire with a stiffening factor of $F_s = 1.15$

can consider three components of scattering that we have modeled here: boundary scattering, impurity scattering, and phonon-phonon scattering. In Figure 4.20 we plot the MFP resulting from different scattering mechanisms as a function of the wavevector for an example nanowire with and without stiffening. We note that the MFP from boundary scattering is unaffected by softening as it is controlled by the size of the nanowires, and do not plot it separately. For both the impurity scattering and the phonon-phonon scattering, the increase in the phonon frequencies with stiffening increases the scattering rate. This reduces both the MFP (Figure 4.20 C and D) and the thermal conductivity. For impurity scattering, the rate is proportional to $1/\omega^4$, leading to a dependency on the stiffening factor of $1/F_s^4$, and thus a dependence of the impurity MFP to $1/F_s^3$.

For phonon-phonon scattering, this dependence becomes more complicated as more than just the phonon frequencies are affected by stiffening. In particular, the Debye temperature and the constants describing the scattering can be affected by changes in the elastic modulus. For the softening formulation in Si nanoribbons, mean phonon-phonon scattering can be modeled as

$$\tau^{-1}_{phonon-phonon,Si}(\omega) = B\omega^2 T exp(\frac{-C_u}{T}), \tag{4.9}$$

where B, ω and C_u are dependent on softening. The dependence of the constant B on the parameters directly modified by stiffening/softening has been given as $B = \frac{\hbar\gamma^2}{Mv^2\Theta_D}$[57]. Where the Debye temperature Θ_D, the Grüneisen parameter γ and the velocity v's dependence on stiffing/softening result in a $1/F_s$ proportionality for B. Here, for ZnO, we use this same dependence for the parameter B in equation 2.18, leading to a reduction in the MFP for stiffened nanowires.

An important difference seen here in ZnO when compared to Si nanoribbons is the relative orders of magnitude of the MFP from impurity and phonon-phonon scattering. In ZnO the MFPs from these scattering modes are, for much of the first Brillouin zone, on the same order as the boundary scattering, i.e. tens of nanometers. Thus, in Si nanoribbons, the effects of boundary scattering dominate, resulting in an overall small effect on thermal conductivity

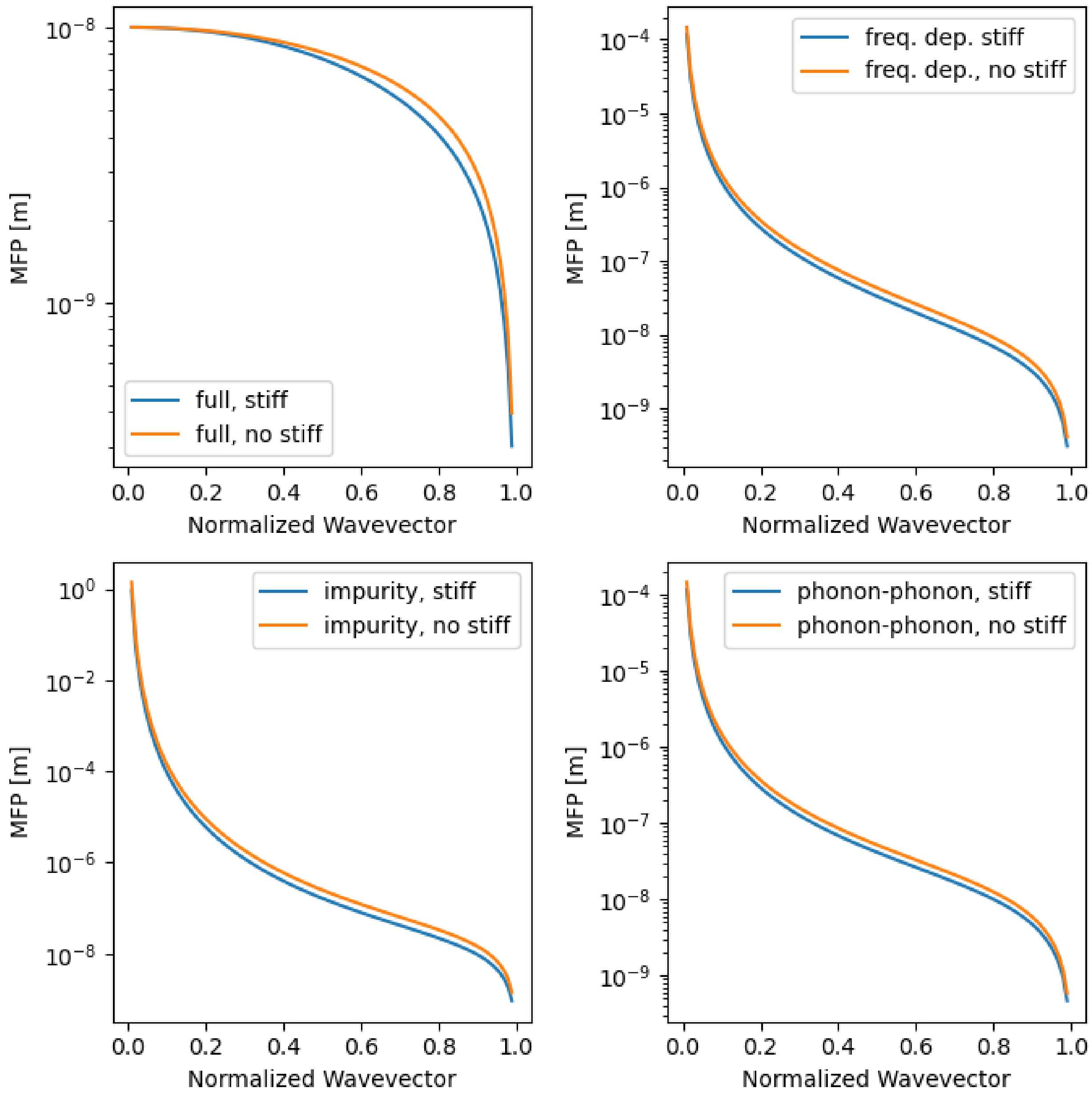

Figure 4.20: MFP of an example system (10 nm ZnO wire with a stiffening factor of $F_s = 1.15$) demonstrating the effect of the stiffening of the total MFP and the MFP for frequency dependent components (impurity and phonon-phonon scattering) both combined and independently

from scattering effects. In ZnO, the boundary scattering fully dominates only at very small sizes. This allows for the opposite effects of the MFP on thermal conductivity to help cancel out the velocity effects. Under this model, the alterations to the thermal conductivity only become apparent at very small sizes.

The addition of stiffening effects in heat capacity operates mainly to shift the temperature of the peak thermal conductivity to a higher temperature. This is similar to the effect seen in silicon nanoribbons with a softened dispersion relation, where the heat capacity effect shifts the peak thermal conductivity to lower temperatures. In Figure 4.21 the per-wavevector heat capacity is plotted at a series of temperatures. We see that at lower temperatures the heat capacity attributed to high frequency (large wavevector) phonons is reduced by stiffening, and the effect becomes smaller with increasing temperature. We attribute this to a shift in the phonon occupation. As the material is stiffened the frequencies of large wavevector phonons are increased, increasing the phonon energies and decreasing the occupation at a given temperature.

In Figure 4.22 heat capacity is plotted as a function of temperature for cases with and without stiffening. The result is that stiffening tends to reduce the heat capacity at low temperatures. At high temperatures, the effects of stiffening disappear, and the heat capacity approaches the unstiffened value. Much as for the case of Si, the stiffening effect can be viewed as an alteration of the Debye temperature. The Debye temperature is directly related to the stiffness of a crystal, so in the case of softening, e.g. in Si nanowires, the Debye temperature is reduced, and thus the high temperature limit of the heat capacity is approached more rapidly. Here, in the case of stiffening in ZnO, the Debye temperature is increased, and thus the high temperature limit of the heat capacity is approached more slowly.

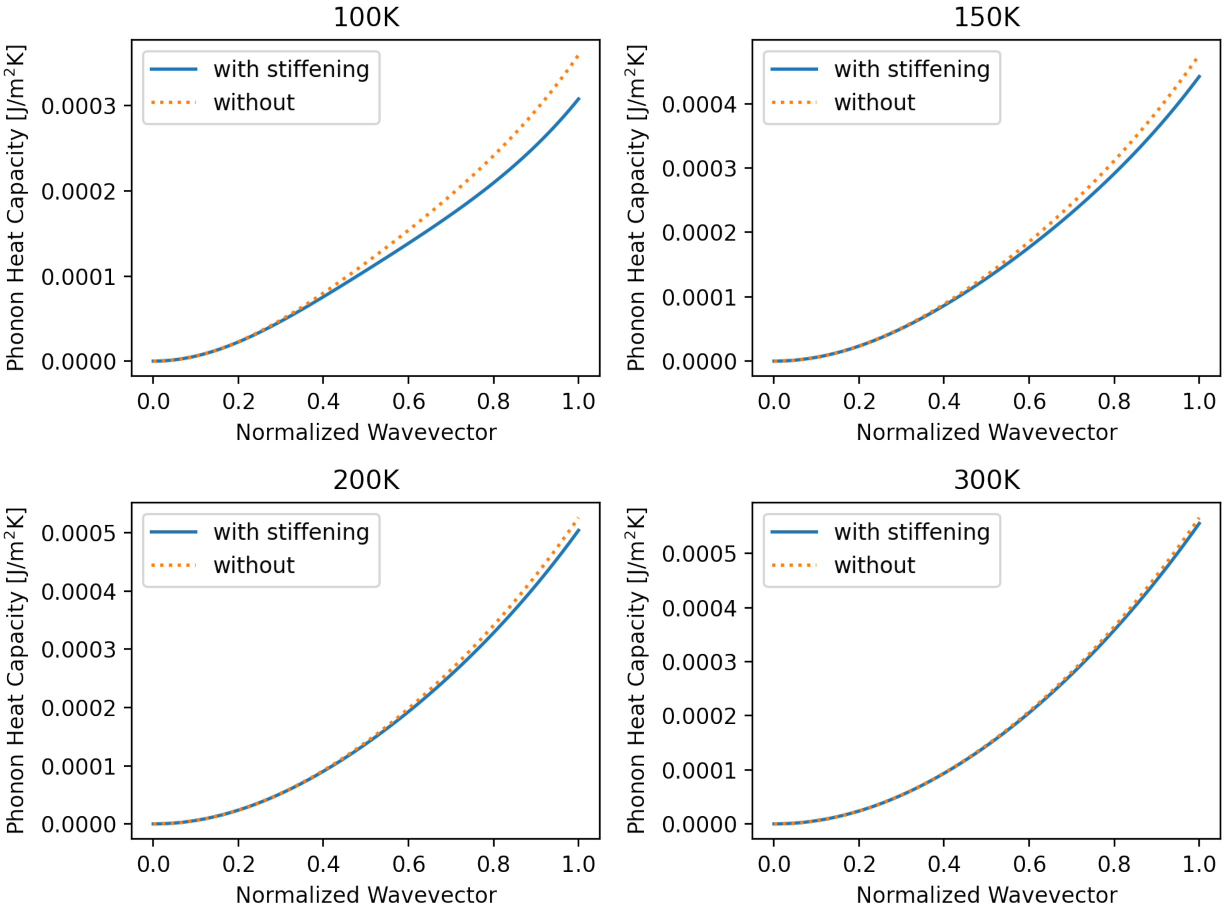

Figure 4.21: Frequency dependent heat capacity for an example system (10 nm ZnO wire with a stiffening factor of $F_s = 1.15$) at multiple temperatures with and without stiffening.

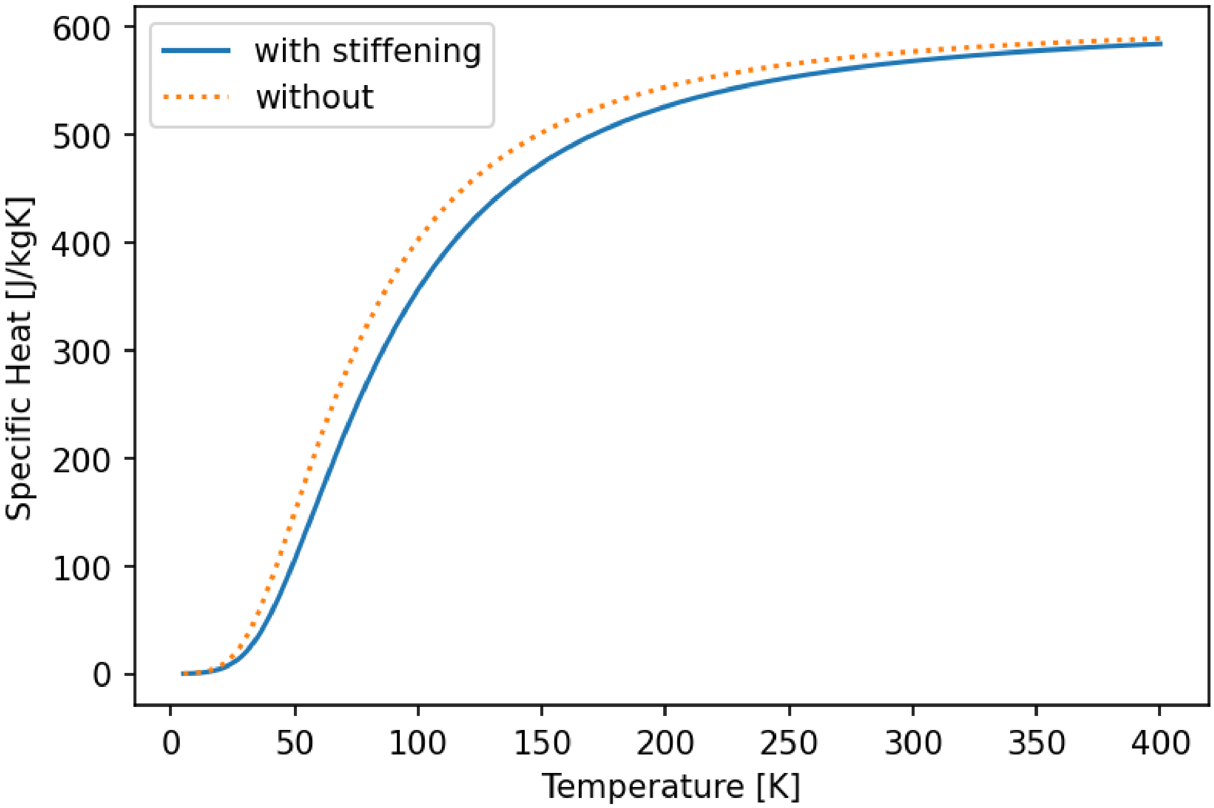

Figure 4.22: Temperature dependent heat capacity of an example system (10 nm ZnO wire with a stiffening factor of $F_s = 1.15$) demonstrating the shift in the heat capacity with stiffing.

4.2.2 Molecular Dynamics

Our models for thermal conductivity in ZnO nanowires indicate that the effects of stiffening should not be readily apparent in measurements of thermal conductivity at many size scales. This is consistent with observations from experiments using nanowires of 70 nm and larger[4] where a stiffening effect was not observed. However, as the lack of strong stiffening effect in part arises from the canceling out of velocity and MFP effects, this result is dependent on the nature of scattering in the material. This presents a weakness of a model which employs scattering rates described by empirical relations. While these empirical relations work well to model the bulk thermal conductivity, they do not fit data from nanowires. Additionally, the nature of the stiffening effect is subject to the empirical form chosen for the scattering rates. If the scattering rates are formulated to have a different dependence on the phonon frequencies, it may be possible to find a set of parameters that fit bulk ZnO data well but cause the scattering rate to have a different dependence on the stiffening factor.

As experimental results from ZnO nanowires are limited, we turn to molecular dynamics to provide a measure of the thermal conductivity with more realistic scattering rates. As phonon-phonon scattering in MD arises from the trajectories of the atoms, it is not subject to the choice of an empirical scattering relation or its dependence on the stiffening factor.

First, we examine the size dependence of the elastic modulus on the thermal conductivity of the nanowires. Here we confirm that the elastic modulus of our nanowires in MD is dependent on the size of the nanowire. The stiffening seen in our nanowires additionally is comparable to the stiffening seen in nanowires from Agrawal et al. [27] in both MD and experiment. Adding these MD data points to the stiffening model results in parameters of 1.44 nm for the shell thickness and 142.7 GPa and 211.1 GPa for the core and shell elastic moduli respectively. This indicates that the thermal conductivity of our MD nanowires should contain the effects of stiffening. For the size range of the MD, the stiffening factor should range from approximately $F_s = 1.13 - 1.22$. This fit is demonstrated in Figure 4.23

To analyze the possible effects of stiffening, we compare the thermal conductivity from

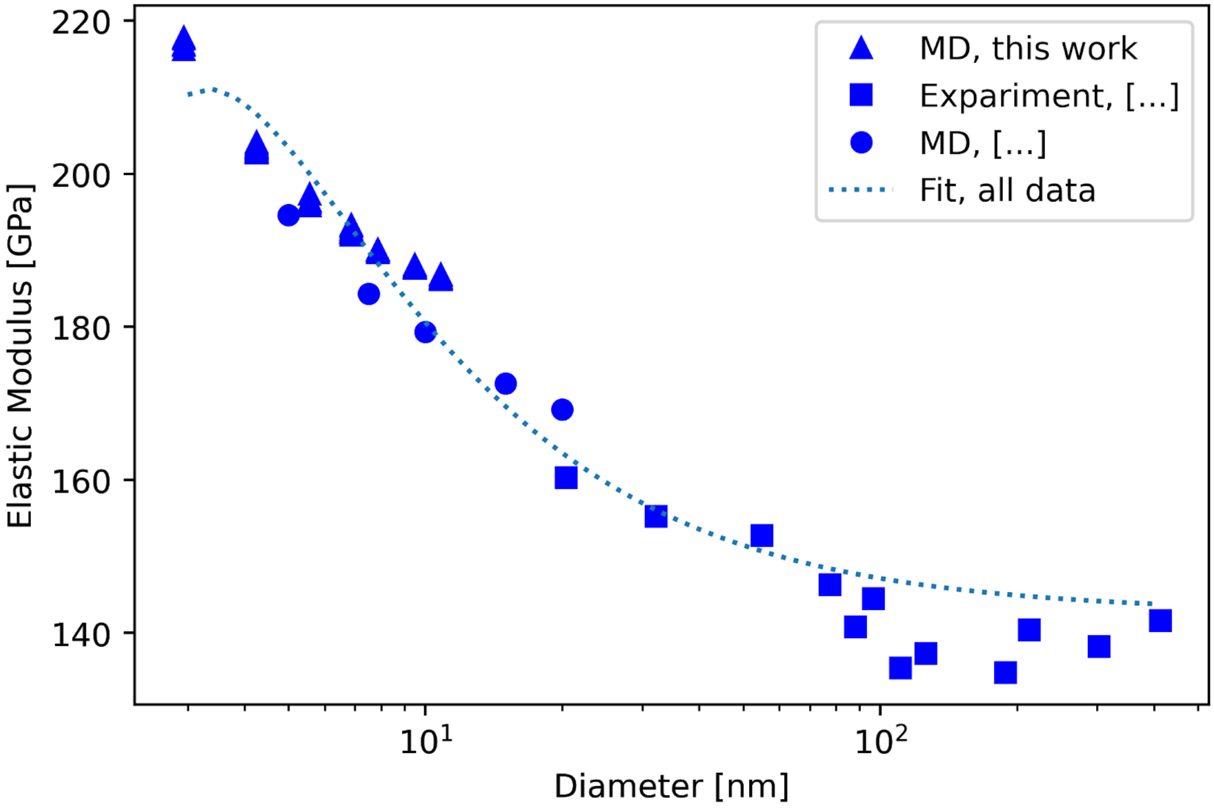

Figure 4.23: Size dependent elastic modulus from experiment and MD from Agrawal et al.[27] and MD from this work, fit to Eq. 2.5.

MD with the values predicted from our model. Using the fitting parameters from above, in Figure 4.24 we compare the thermal conductivity at 300 K for a sequence of MD simulations and our model. As excepted, our thermal conductivity model indicates that the stiffening effects should cause a small increase in the thermal conductivity vs a model without stiffening effects. This increase is most apparent at small sizes where the stiffening factor is the largest. Across all sizes, the thermal conductivity from MD is greater than for both the stiffened and un-stiffened model.

To understand the higher thermal conductivity in the model we explored two avenues. First, the parameters for the thermal conductivity model, particularly the scattering, are fitted to thermal conductivity data from the entirety of the temperature range. This results in the higher low-temperature thermal conductivity measurements dominating the parameter fit. This results in an underprediction of the thermal conductivity at 300 K of around 15% for the bulk thermal conductivity. Fitting our bulk thermal conductivity model for just high-temperature thermal conductivity (between 200 K and 400 K) results in a model that predicts the bulk thermal conductivity at 300 K well. Using these parameters, as shown in Figure 4.24, the thermal conductivity from the model, with and without softening is increased. However, this increase is small and insufficient to fully capture the MD data.

The other avenue that we explore is the surface specularity for our MD. Thus far our model has assumed fully diffuse surfaces. For a highly roughened nanowire, a fully diffuse boundary condition might be appropriate, however, in our MD, the surfaces of the wires are atomically smooth. For smooth surfaces, specular reflections can increase the MFP from surface scattering, increasing the thermal conductivity. To investigate this, we add a specular component to our thermal conductivity model.

To incorporate the thermal conductivity, we modify the surface scattering MFP as[]

$$l_s = \frac{(1+p)}{(1-p)}D, \tag{4.10}$$

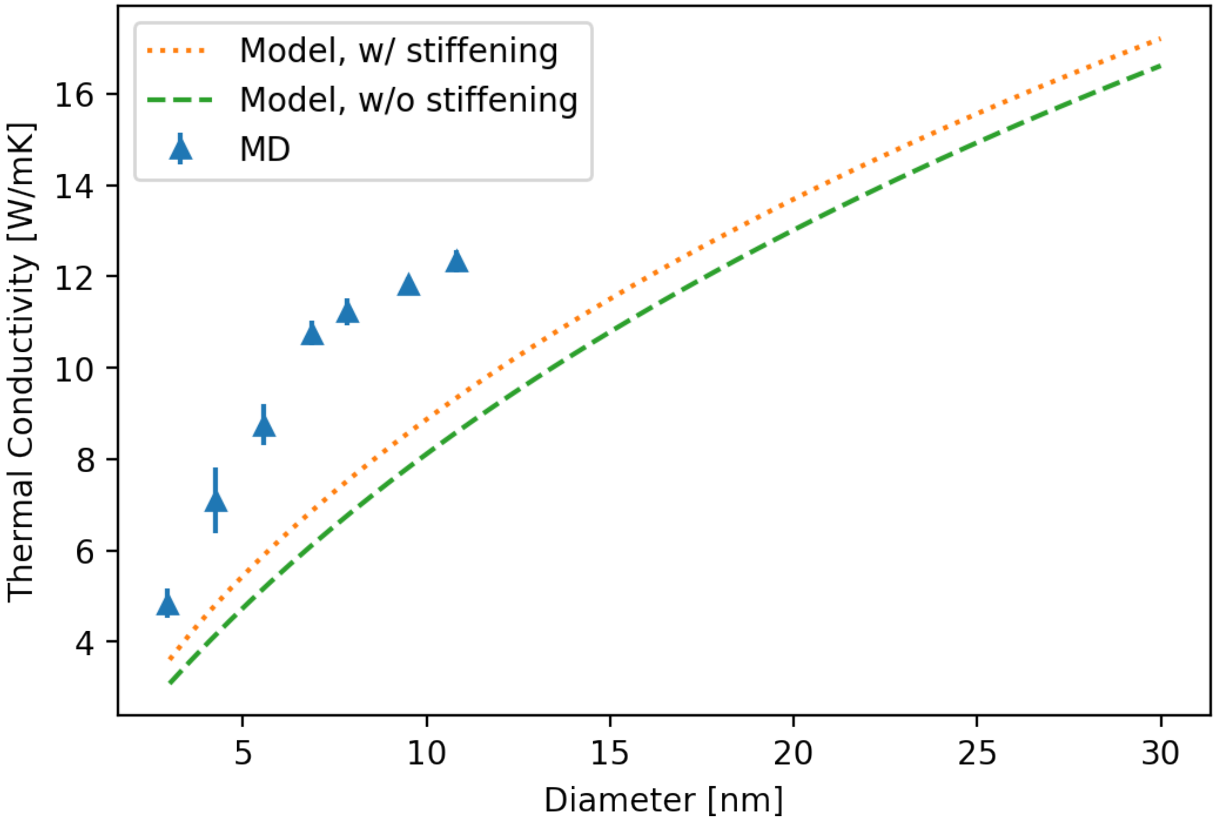

Figure 4.24: Comparison of MD thermal conductivity at 300 K and the modeling with and without stiffening as a function of size.

where D is the wire diameter, and p is the fraction of specular reflections from the surface. The specularity parameter p is dependent on the surface roughness η and the wave vector q. This is calculated as $p = exp(-4\eta^2 q^2)$[90]. Note here that the specularity parameter is dependent on the wavevector and not the phonon frequency. As a result, it is not directly modified by changes to the elastic modulus. However, as it alters the MFP for surface scattering, it may change how dominant the phonon-phonon and impurity scattering rates are.

The addition of surface specularity results in another free parameter for the model—the surface roughness. Here we note that large values of η result in highly diffuse surfaces (where $p \to 0$) and a roughness of $\eta = 0\,\text{nm}$ results in a perfectly specular surface ($p = 1$). For our smooth surfaced wires, we consider surface roughness on the order of 0.1 nm. This is on the order of roughness observed in the fit of thermal conductivity for other nanostructures, in particular nanostructures such as FIB manufactured Si nanoribbons [3].

In Figure 4.25 we see that for a model with a surface specularity of 0.1 nm, the thermal conductivity of both the stiffened and unstiffened model matches well with the thermal conductivity from MD for a wide range of sizes. Additionally, the uncertainty in the thermal conductivity from MD is approximately the same size as the difference between the two models. This result helps to validate the conclusion that the total effect of stiffening in ZnO should result in a change in the thermal conductivity that is difficult to perceive. As the relative insensitivity to stiffening of the thermal conductivity is strongly related to the scattering rates, the correlation of both models to MD data helps to confirm that the empirical models for scattering provide a good approximation of the scattering behavior. In MD the scattering is inherent to the simulation rather than requiring a choice of model to be parameterized.

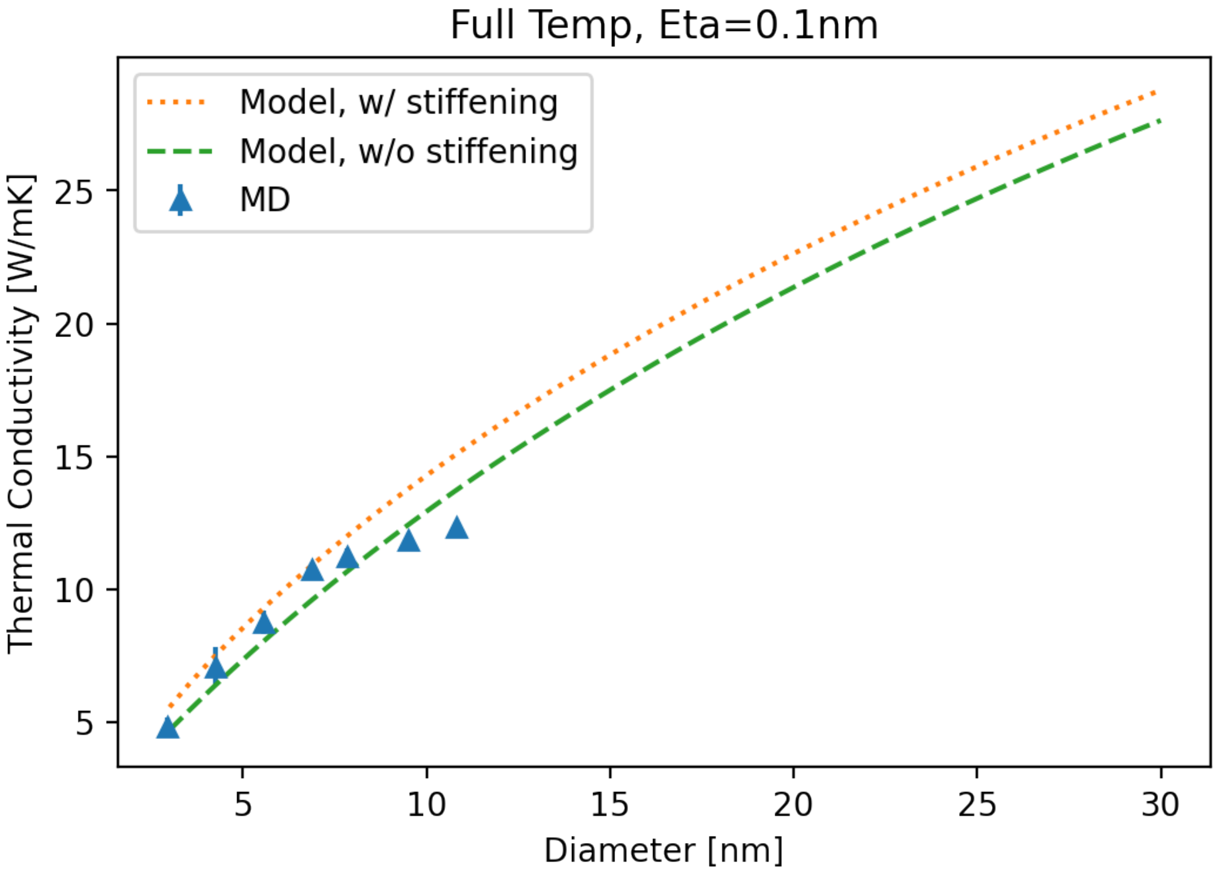

Figure 4.25: Comparison of MD thermal conductivity at 300 K and the modeling with the addition of frequency dependent surface specularity ($\eta = 0.1$ nm) with and without stiffening as a function of size.

Chapter 5

Conclusions and Outlook

Through this work we have developed a deeper understanding of the effect of acoustic softening/acoustic stiffening in semiconducting nanowires.

Using Si nanoribbons, I have compared MD calculations and a MCRT model that includes the effect of high aspect ratios with experimental measurements of thermal conductivity from the literature. For these nanostructures, I have modeled the dependence of thermal conductivity on geometric size, including both the width and the thickness of the wires, using both MD and MCRT. Using a simplified velocity-only model for acoustic softening and combining it with the MCRT model for geometric effects better agreement between experiment and modeling was achieved than just considering geometric effects alone. Despite this, the models were unable to fully capture the thermal conductivity of the smallest nanostructures.

Additionally, by using wave packet simulations, I demonstrated that while the phonon velocity is reduced with decreasing nanostructure size, this decrease occurs at much smaller sizes in MD than would be expected from experiment. This may be due to the same effects causing a difference between experiment and computational methods for the changes in the elastic modulus [7, 13–15] in Si.

While a velocity only model for acoustic softening/acoustic stiffening gives a rough approximation of the effects on thermal conductivity, it doesn't capture the full implications of altered elastic moduli on the dispersion relation thermal conductivity. To capture these more detailed effects I developed a model of acoustic softening that incorporates the effects of changes in the elastic modulus on components of thermal conductivity beyond the phonon group velocity. By considering how a change in the elastic modulus (and thus the continuum speed of sound) should impact the general form of the dispersion relation, we are able to extract the expected influence of acoustic softening on heat capacity and various scattering processes in Si nanoribbons. Including these factors allows us to match the general size dependence of thermal conductivity for wires for which acoustic softening has been observed.

This model indicates that acoustic softening should modify more than just the group velocity. In particular, the heat capacity should be increased at low temperatures, while the mean free path should be slightly reduced. This results in a shifting of the peak thermal conductivity to lower temperatures and an increase in the thermal conductivity at low temperatures. This is similar to effects seen in Ge-Si core-shell wires [38], and the effect is likely to be important for the thermal conductivity at low temperatures and for wires with surface layers.

Further, this model indicates that the influence of acoustic softening phenomena at the nanoscale implicates changes in the dispersion relation that occur on these scales. Incorporating more fine-grained predictions of how the dispersion relation should be modified by surface phenomena at the nanoscale should improve these results and increase the ability of thermal conductivity models to predict nanoscale thermal conductivity in size regimes where size-dependent elastic-modulus effects occur.

While Si provides a number of experimental results to compare modeling against, it suffers from a lack of strong agreement in the literature for the size dependent elastic modulus [21]. As seen here, and elsewhere in the literature[7, 13–15], computational methods don't capture softening well when compared with experimental results. By exploring the potential influence on thermal conductivity of the related size-dependent stiffening effect in ZnO nanowires, I was able to explore a system where both computation and experiment have better agreement. By employing both MD and modeling we have indicated that for small nanowires, stiffening may increase the thermal conductivity observed in experiment relative to that predicted from boundary scattering. However, this increase is small enough that it may be difficult to resolve experimentally. This is in part due to the competing effects of scattering, heat capacity, and group velocity. While the effect of stiffening on group velocity tends to increase thermal conductivity at small sizes, the effects on heat capacity and scattering tend to decrease thermal conductivity.

An important limitation on this work remains the predictions of scattering rates. While the empirical rate used here have enjoyed long used for predicting thermal conductivity, even at the nanoscale, it is possible that, particularly for the phonon-phonon scattering rates, these formulas fail to capture relevant physics. In particular, the power law formulas used here for phonon-phonon scattering do not, in and of themselves, enforce selection rules for Umklapp scattering. Recent experimental work in silver nanowires has indicated that changes in the optical bands may result in significant changes to allowed phonon-phonon scattering process, increasing the mean free path[91]. To include such effects, it may be necessary to compute scattering rates from *ab initio* simulations including surfaces to fully capture effects seen in experiment.

From this work we can make some observations on materials likely to exhibit large stiffening or softening effects in thermal conductivity. First, they should have very strong stiffening or softening of the elastic modulus as the effect on the thermal conductivity is proportional to the square root of this change. Materials with large changes in the coordination number at the surface and large changes in bond lengths near the surface are likely to exhibit the strongest effects. Secondly, the more strongly the scattering is dominated by boundary and surface effects, the more strongly the thermal conductivity will be affected. In general, the effects on phonon-phonon and impurity scattering tend to counter the effects of stiffening/softening on velocity. Materials with large band gaps between the optical and acoustic phonons, as well as high purity materials should have less dominant phonon-phonon and impurity scattering, and thus effects from velocity will be more dominant.

Using dispersion relations that incorporate acoustic softening or acoustic stiffening, we were able to explore the influence of the size dependence of the elastic modulus at the nanoscale on the factors of thermal conductivity. For the first time we considered the influence of factors other than group velocity, namely heat capacity and scattering and explored the relative magnitude of effects on these factors in multiple materials. These efforts will help to advance a better understanding of the full scope of softening and stiffening phenomenon affecting nanoscale thermal transport. More importantly, this understanding can help identify materials that should demonstrate acoustic softening/acoustic stiffening effects for further study.

BIBLIOGRAPHY

[1]M. D. Gerboth and D. G. Walker, “Effects of acoustic softening on thermal conductivity beyond group velocity”, Journal of Applied Physics **127**, 204302 (2020).

[2]M. C. Wingert, S. Kwon, M. Hu, D. Poulikakos, J. Xiang, and R. Chen, “Sub-amorphous Thermal Conductivity in Ultrathin Crystalline Silicon Nanotubes”, Nano Letters **15**, 2605–2611 (2015).

[3]L. Yang, Y. Yang, Q. Zhang, Y. Zhang, Y. Jiang, Z. Guan, M. Gerboth, J. Yang, Y. Chen, D. Greg Walker, T. T. Xu, and D. Li, “Thermal conductivity of individual silicon nanoribbons”, Nanoscale **8**, 17895–17901 (2016).

[4]R. Chen, J. Lee, W. Lee, and D. Li, “Thermoelectrics of Nanowires”, Chemical Reviews **119**, 9260–9302 (2019).

[5]R. E. Miller and V. B. Shenoy, “Size-dependent elastic properties of nanosized structural elements”, Nanotechnology **11**, 139–147 (2000).

[6]H. Sadeghian, J. F. L. Goosen, A. Bossche, B. J. Thijsse, and F. Van Keulen, “Effects of size and surface on the elasticity of silicon nanoplates: Molecular dynamics and semi-continuum approaches”, Thin Solid Films **520**, 391–399 (2011).

[7]K. Kang and W. Cai, “Size and temperature effects on the fracture mechanisms of silicon nanowires: Molecular dynamics simulations”, International Journal of Plasticity **26**, 1387–1401 (2010).

[8] H. Sadeghian, C. K. Yang, J. F. L. Goosen, E. Van Der Drift, A. Bossche, P. J. French, and F. Van Keulen, "Characterizing size-dependent effective elastic modulus of silicon nanocantilevers using electrostatic pull-in instability", Applied Physics Letters **94**, 221903 (2009).

[9] H. Sadeghian, J. F. L. Goosen, A. Bossche, and F. Van Keulen, "Surface stress-induced change in overall elastic behavior and self-bending of ultrathin cantilever plates", Applied Physics Letters **94**, 231908 (2009).

[10] H. W. Shim, L. G. Zhou, H. Huang, and T. S. Cale, "Nanoplate elasticity under surface reconstruction", Applied Physics Letters **86**, 1–3 (2005).

[11] B. Lee and R. E. Rudd, "First-principles calculation of mechanical properties of Si⟨001⟩ nanowires and comparison to nanomechanical theory", Physical Review B **75**, 195328 (2007).

[12] B. Gong, Q. Chen, and D. Wang, "Molecular dynamics study on size-dependent elastic properties of silicon nanoplates", Materials Letters **67**, 165–168 (2012).

[13] H. Sadeghian, C.-K. Yang, J. F. L. Goosen, A. Bossche, U. Staufer, P. J. French, and F. van Keulen, "Effects of size and defects on the elasticity of silicon nanocantilevers", Journal of Micromechanics and Microengineering **20**, 064012 (2010).

[14] H. Sadeghian, H. Goosen, A. Bossche, B. Thijsse, and F. van Keulen, "On the size-dependent elasticity of silicon nanocantilevers: impact of defects", Journal of Physics D: Applied Physics **44**, 072001 (2011).

[15] Y. Zhu, F. Xu, Q. Qin, W. Y. Fung, and W. Lu, "Mechanical Properties of Vapor−Liquid−Solid Synthesized Silicon Nanowires", Nano Letters **9**, 3934–3939 (2009).

[16] M. J. Gordon, T. Baron, F. Dhalluin, P. Gentile, and P. Ferret, "Size effects in mechanical deformation and fracture of cantilevered silicon nanowires", Nano Letters **9**, 525–529 (2009).

[17]Y. Calahorra, O. Shtempluck, V. Kotchetkov, and Y. E. Yaish, “Young’s modulus, residual stress, and crystal orientation of doubly clamped silicon nanowire beams”, Nano Letters **15**, 2945–2950 (2015).

[18]C. C. Röhlig, M. Niebelschütz, K. Brueckner, K. Tonisch, O. Ambacher, and V. Cimalla, “Elastic properties of nanowires”, Physica Status Solidi (B) Basic Research **247**, 2557–2570 (2010).

[19]X. D. Han, K. Zheng, Y. F. Zhang, X. N. Zhang, Z. Zhang, and Z. L. Wang, “Low-Temperature In Situ Large-Strain Plasticity of Silicon Nanowires”, Advanced Materials **19**, 2112–2118 (2007).

[20]X. Li, T. Ono, Y. Wang, and M. Esashi, “Ultrathin single-crystalline-silicon cantilever resonators: Fabrication technology and significant specimen size effect on Young’s modulus”, Applied Physics Letters **83**, 3081–3083 (2003).

[21]M. Nasr Esfahani and B. E. Alaca, “A Review on Size-Dependent Mechanical Properties of Nanowires”, Advanced Engineering Materials **21**, 1900192 (2019).

[22]Y. Zhang, M. K. Ram, E. K. Stefanakos, and D. Y. Goswami, “Synthesis, Characterization, and Applications of ZnO Nanowires”, Journal of Nanomaterials **2012**, 22 (2012).

[23]V. Consonni, J. Briscoe, E. Kärber, X. Li, and T. Cossuet, “ZnO nanowires for solar cells: a comprehensive review”, Nanotechnology **30**, 362001 (2019).

[24]Y. Yang, K. C. Pradel, Q. Jing, J. M. Wu, F. Zhang, Y. Zhou, Y. Zhang, and Z. L. Wang, “Thermoelectric nanogenerators based on single Sb-doped ZnO micro/nanobelts”, ACS Nano **6**, 6984–6989 (2012).

[25]C. Q. Chen, Y. Shi, Y. S. Zhang, J. Zhu, and Y. J. Yan, “Size Dependence of Young’s Modulus in ZnO Nanowires”, Physical Review Letters **96**, 075505 (2006).

[26]G. Stan, C. V. Ciobanu, P. M. Parthangal, and R. F. Cook, “Diameter-Dependent Radial and Tangential Elastic Moduli of ZnO Nanowires”, Nano Letters **7**, 3691–3697 (2007).

[27]R. Agrawal, B. Peng, E. E. Gdoutos, and H. D. Espinosa, "Elasticity Size Effects in ZnO Nanowires−A Combined Experimental-Computational Approach", Nano Letters **8**, 3668–3674 (2008).

[28]F. Xu, Q. Qin, A. Mishra, Y. Gu, and Y. Zhu, "Mechanical Properties of ZnO Nanowires Under Different Loading Modes", Nano Res **3**, 271–280 (2010).

[29]S. Fan, S. Bi, Q. Li, Q. Guo, J. Liu, Z. Ouyang, C. Jiang, and J. Song, "Size-dependent Young's modulus in ZnO nanowires with strong surface atomic bonds", Nanotechnology **29**, 125702 (2018).

[30]H. Yao, G. Yun, N. Bai, and J. Li, "Surface elasticity effect on the size-dependent elastic property of nanowires", Journal of Applied Physics **111** (2012).

[31]X. J. Liu, J. W. Li, Z. F. Zhou, L. W. Yang, Z. S. Ma, G. F. Xie, Y. Pan, and C. Q. Sun, "Size-induced elastic stiffening of ZnO nanostructures: Skin-depth energy pinning", Applied Physics Letters **94**, 131902 (2009).

[32]C. Q. Sun, B. K. Tay, X. T. Zeng, S. Li, T. P. Chen, J. Zhou, H. L. Bai, and E. Y. Jiang, "Bond-order-bond-length-bond-strength (bond-OLS) correlation mechanism for the shape-and-size dependence of a nanosolid", Journal of Physics Condensed Matter **14**, 7781–7795 (2002).

[33]A. J. Kulkarni, M. Zhou, and F. J. Ke, "Orientation and size dependence of the elastic properties of zinc oxide nanobelts", OF PHYSICS PUBLISHING NANOTECHNOLOGY Nanotechnology **16**, 2749–2756 (2005).

[34]N. W. Ashcroft and N. D. Mermin, *Solid state physics [by] neil w. ashcroft [and] n. david mermin.* eng (Brooks/Cole, New York, 1976).

[35]M. T. Dove, *Introduction to lattice dynamics / martin t. dove.* eng, Cambridge topics in mineral physics and chemistry ; 4 (Cambridge University Press, Cambridge, 1993).

[36]D. Li, Y. Wu, P. Kim, L. Shi, P. Yang, and A. Majumdar, "Thermal conductivity of individual silicon nanowires", Applied Physics Letters **83**, 2934–2936 (2003).

[37] R. Chen, A. I. Hochbaum, P. Murphy, J. Moore, P. Yang, and A. Majumdar, “Thermal Conductance of Thin Silicon Nanowires”, Physical Review Letters **101**, 105501 (2008).

[38] M. C. Wingert, Z. C. Y. Chen, E. Dechaumphai, J. Moon, J.-H. Kim, J. Xiang, and R. Chen, “Thermal Conductivity of Ge and Ge–Si Core–Shell Nanowires in the Phonon Confinement Regime”, Nano Letters **11**, 5507–5513 (2011).

[39] C. T. Bui, R. Xie, M. Zheng, Q. Zhang, C. H. Sow, B. Li, and J. T. L. Thong, “Diameter-Dependent Thermal Transport in Individual ZnO Nanowires and its Correlation with Surface Coating and Defects”, Small **8**, 738–745 (2012).

[40] M. Xia, Z. Cheng, J. Han, M. Zheng, C.-H. Sow, J. T. L. Thong, S. Zhang, and B. Li, “Gallium ion implantation greatly reduces thermal conductivity and enhances electronic one of ZnO nanowires”, AIP Advances **4**, 057128 (2014).

[41] J.-W. Jiang, H. S. Park, and T. Rabczuk, “Polar surface effects on the thermal conductivity of ZnO nanowires: a shell-like surface reconstruction-induced preserving mechanism”, Nanoscale **5**, 11035 (2013).

[42] A. J. Kulkarni and M. Zhou, “Size-dependent thermal conductivity of zinc oxide nanobelts”, Applied Physics Letters **88**, 141921 (2006).

[43] A. Krishnasamy Bharathi, A. Kamat, and A. C. Van Duin, “Study of effect of water vapor and mechanical strain on thermal conductivity of zinc oxide using the ReaxFF reactive force field”, Computational and Theoretical Chemistry (2012).

[44] A. J. Kulkarni and M. Zhou, “Tunable thermal response of ZnO nanowires”, Nanotechnology **18**, 435706 (2007).

[45] A. J. Kulkarni and M. Zhou, “Surface-effects-dominated thermal and mechanical responses of zinc oxide nanobelts”, Acta Mechanica Sinica/Lixue Xuebao **22**, 217–224 (2006).

[46] J. Callaway, “Model for Lattice Thermal Conductivity at Low Temperatures”, Physical Review **113**, 1046–1051 (1959).

[47] M. G. Holland, "Analysis of lattice thermal conductivity", Physical Review **132**, 2461–2471 (1963).

[48] C. Dames and G. Chen, "Theoretical phonon thermal conductivity of Si/Ge superlattice nanowires", Journal of Applied Physics **95**, 682–693 (2004).

[49] F. Yang and C. Dames, "Mean free path spectra as a tool to understand thermal conductivity in bulk and nanostructures", Physical Review B **87**, 035437 (2013).

[50] B. Bhushan and X. Li, "Micromechanical and tribological characterization of doped single-crystal silicon and polysilicon films for microelectromechanical systems devices", Journal of Materials Research **12**, 54–63 (1997).

[51] L. Yang, Q. Zhang, Z. Cui, M. Gerboth, Y. Zhao, T. T. Xu, D. G. Walker, and D. Li, "Ballistic Phonon Penetration Depth in Amorphous Silicon Dioxide", Nano Letters **17**, 7218–7225 (2017).

[52] W. Park, D. D. Shin, S. J. Kim, J. S. Katz, J. Park, C. H. Ahn, T. Kodama, M. Asheghi, T. W. Kenny, and K. E. Goodson, "Phonon conduction in silicon nanobeams", Applied Physics Letters **110**, 213102 (2017).

[53] E. Sondheimer, "The mean free path of electrons in metals", Advances in Physics **1**, 1–42 (1952).

[54] K. Fuchs and N. F. Mott, "The conductivity of thin metallic films according to the electron theory of metals", Mathematical Proceedings of the Cambridge Philosophical Society **34**, 100 (1938).

[55] M. Asheghi, M. N. Touzelbaev, K. E. Goodson, Y. K. Leung, and S. S. Wong, "Temperature-Dependent Thermal Conductivity of Single-Crystal Silicon Layers in SOI Substrates", Journal of Heat Transfer **120**, 30 (1998).

[56] A. J. H. Mcgaughey and A. Jain, "Nanostructure thermal conductivity prediction by Monte Carlo sampling of Phonon Free Paths", Applied Physics Letters **100**, 061911 (2012).

[57] M. Kazan, G. Guisbiers, S. Pereira, M. R. Correia, P. Masri, A. Bruyant, S. Volz, and P. Royer, “Thermal conductivity of silicon bulk and nanowires: Effects of isotopic composition, phonon confinement, and surface roughness”, Journal of Applied Physics **107**, 083503 (2010).

[58] A. Ward and D. A. Broido, “Intrinsic phonon relaxation times from first-principles studies of the thermal conductivities of Si and Ge”, Physical Review B **81**, 085205 (2010).

[59] M. W. Wolf and J. J. Martin, “Low temperature thermal conductivity of zinc oxide”, physica status solidi (a) **17**, 215–220 (1973).

[60] J. Alvarez-Quintana, E. Martínez, E. Pérez-Tijerina, S. A. Pérez-García, and J. Rodríguez-Viejo, “Temperature dependent thermal conductivity of polycrystalline ZnO films”, Journal of Applied Physics **107**, 063713 (2010).

[61] N. W. Ashcroft and D. N. Mermin, *Solid State Physics* (Brooks/Cole, Belmont, Ca, 1976), pp. 453–463.

[62] S. Plimpton, “Fast Parallel Algorithms for Short-Range Molecular Dynamics”, Journal of Computational Physics **117**, 1–19 (1995).

[63] J. Tersoff, “New empirical approach for the structure and energy of covalent systems”, Physical Review B **37**, 6991–7000 (1988).

[64] J. Tersoff, “Modeling solid-state chemistry: Interatomic potentials for mnlticomponent systems”, PHYSICAL REVIEW B **39** (1989).

[65] J. Tersoff, “Empirical interatomic potential for silicon with improved elastic properties”, Physical Review B **38**, 9902–9905 (1988).

[66] D. A. Broido, A. Ward, and N. Mingo, “Lattice thermal conductivity of silicon from empirical interatomic potentials”, Physical Review B **72**, 014308 (2005).

[67]S. Munetoh, T. Motooka, K. Moriguchi, and A. Shintani, "Interatomic potential for Si–O systems using Tersoff parameterization", Computational Materials Science **39**, 334–339 (2007).

[68]Y. He and G. Galli, "Microscopic Origin of the Reduced Thermal Conductivity of Silicon Nanowires", Physical Review Letters **108**, 215901 (2012).

[69]Z. Liang, T. E. Wilson, and P. Keblinski, "Phonon interference in crystalline and amorphous confined nanoscopic films", Journal of Applied Physics **121** (2017).

[70]B. Deng, A. Chernatynskiy, M. Khafizov, D. H. Hurley, and S. R. Phillpot, "Kapitza resistance of Si/SiO2 interface", Journal of Applied Physics **115** (2014).

[71]C. J. Fennell and J. D. Gezelter, "Is the Ewald summation still necessary? Pairwise alternatives to the accepted standard for long-range electrostatics", Journal of Chemical Physics **124**, 234104 (2006).

[72]D. J. Binks, "Computational Modelling of Zinc Oxide and Related Oxide Ceramics", PhD thesis (1994), p. 28.

[73]R. Agrawal, B. Peng, and H. D. Espinosa, "Experimental-Computational Investigation of ZnO nanowires Strength and Fracture", Nano Letters **9**, 4177–4183 (2009).

[74]M. D. Kluge, J. R. Ray, and A. Rahman, "Amorphous-Silicon formation by rapid quenching: A molecular-dynamics study", Physical Review B **36**, 4234–4237 (1987).

[75]D. Donadio and G. Galli, "Atomistic Simulations of Heat Transport in Silicon Nanowires", Physical Review Letters **102**, 195901 (2009).

[76]A. France-Lanord, E. Blandre, T. Albaret, S. Merabia, D. Lacroix, and K. Termentzidis, "Atomistic amorphous/crystalline interface modelling for superlattices and core/shell nanowires", Journal of Physics: Condensed Matter J. Phys.: Condens. Matter **26**, 55011–11 (2014).

[77]E. Blandre, L. Chaput, S. Merabia, D. Lacroix, and K. Termentzidis, “Modeling the reduction of thermal conductivity in core/shell and diameter-modulated silicon nanowires”, Physical Review B **91**, 115404 (2015).

[78]A. Stukowski, “Visualization and analysis of atomistic simulation data with OVITO–the Open Visualization Tool”, Modelling and Simulation in Materials Science and Engineering **18**, 015012 (2010).

[79]E. Maras, O. Trushin, A. Stukowski, T. Ala-Nissila, and H. Jónsson, “Global transition path search for dislocation formation in Ge on Si(001)”, Computer Physics Communications **205**, 13–21 (2016).

[80]C. Oligschleger and J. C. Schön, “Simulation of thermal conductivity and heat transport in solids”, Physical Review B **59**, 4125–4133 (1999).

[81]P. K. Schelling, S. R. Phillpot, and P. Keblinski, “Comparison of atomic-level simulation methods for computing thermal conductivity”, Physical Review B **65**, 144306 (2002).

[82]P. K. Schelling, S. R. Phillpot, and P. Keblinski, “Phonon wave-packet dynamics at semiconductor interfaces by molecular-dynamics simulation”, Applied Physics Letters **80**, 2484–2486 (2002).

[83]P. K. Schelling, S. R. Phillpot, and P. Keblinski, “Kapitza conductance and phonon scattering at grain boundaries by simulation”, Journal of Applied Physics **95**, 6082–6091 (2004).

[84]B. Decker, P. K. Schelling, and S. R. Phillpot, “Interfacial phonon scattering in semiconductor nanowires by molecular-dynamics simulation”, Journal of Applied Physics **99** (2006).

[85]Z. Liang and P. Keblinski, “Finite-size effects on molecular dynamics interfacial thermal-resistance predictions”, Physical Review B - Condensed Matter and Materials Physics **90**, 1–12 (2014).

[86] Z. T. Tian, B. E. White, and Y. Sun, "Phonon wave-packet interference and phonon tunneling based energy transport across nanostructured thin films", Appl. Phys. Lett. Applied Physics Letters Nanoscale thermal transport Journal of Applied Physics Journal of Applied Physics Journal of Applied Physics Journal of Applied Physics Nanoscale thermal transport. II. Applied Physics Reviews **9611**, 263113–2484 (2010).

[87] Z. Wei, Y. Chen, and C. Dames, "Wave packet simulations of phonon boundary scattering at graphene edges", Journal of Applied Physics Applied Physics Letters Nanoscale thermal transport Journal of Applied Physics Applied Physics Reviews Applied Physics Letters Journal of Applied Physics Applied Physics Letters **112**, 24328–2484 (2012).

[88] N. A. Roberts and D. G. Walker, "Phonon wave-packet simulations of Ar/Kr interfaces for thermal rectification", Journal of Applied Physics **108** (2010).

[89] W. Liu and M. Asheghi, "Thermal conduction in ultrathin pure and doped single-crystal silicon layers at high temperatures", Journal of Applied Physics **98**, 123523 (2005).

[90] J. M. Ziman, *Electrons and Phonons; the theory of transport phenomena in solids*, International series of monographs on physics (Oxford, England) ˆA100315 (Oxford University Press, London, 1962).

[91] Y. Zhao, M. L. Fitzgerald, Y. Tao, Z. Pan, G. Sauti, D. Xu, Y.-Q. Xu, and D. Li, "Electrical and Thermal Transport through Silver Nanowires and Their Contacts: Effects of Elastic Stiffening", Nano Letters, acs.nanolett.0c02014 (2020).